Studies of the Small-Scale Magnetic and Electric Field Perturbations Observed in the Polar Ionosphere(Dissertation_全文)

AUTHOR(S):

Ishii, Mamoru

学位申請論文

石井　守

主論文

Studies of the Small-Scale Magnetic and Electric Field Perturbations Observed in the Polar Ionosphere

Mamoru Ishii

Dissertation for the degree of Doctor of Science

Department of Geophysics, Faculty of Science
Kyoto University

July 1993

Acknowledgments

This study was performed under the guidance of Prof. M. Sugiura at Research and Development Institute of Tokai University, and under the guidance of Prof. T. Araki. I wish to thank them for their instructive guidance. I am indebted to Drs. T. Iyemori, T. Kamei, M. Takeda, T. Terasawa, S. Machida, S.Taguchi, H. Hanado, H. Naito and the students of the Geomagnetism and Space Magnetism research section of the Department of Geophysics, Kyoto University for their valuable comments and criticisms. I would like to thank Drs. J.A. Slavin, J.D. Craven, L.A. Frank, J.D. Winningham and K. Kimura for permitting me to use their satellite data and to use our paper as some parts of my doctor dissertation. I also wish to express my gratitude to Drs. R. Fujii, K. Shiokawa, A. Matsuoka and other friends for their helpful suggestion, comments and encouragements. Part of the analysis was made by using the facilities at the Data Analysis Center for Geomagnetism and Space magnetism of Kyoto University. This work is supported by the fellowships of the Japan Society for the Promotion of Science for Japanese Junior Scientists.

Abstract

Satellite observations have shown high correlation between magnetic and electric field perturbations in the high latitude field-aligned current regions. In chapter 1 of this paper, the studies of this phenomenon are reviewed briefly. The high correlation has been interpreted by two models. In one of them so called, static model, the observed perturbations are regarded as being static spatial structures, and the ratio of the orthogonal magnetic and electric field components $\Delta B_z/E_x$ represents the height-integrated ionospheric Pedersen conductivity, Σ_P. In another one so called, Alfvén wave model, the observed perturbations are interpreted as being Doppler-shifted Alfvén waves, and the inverse of the ratio gives the Alfvén wave velocity V_A. In chapter 2 of this paper, we investigate the changes of this ratio with spatial scale length using the DE 2 observations. The ratio $\Delta B_z/E_x$ is found to change little with scale length for variations with scale lengths longer than 64 km, or 8.0 s in time. While for variations of smaller scale lengths, which are obtained using numerical filters with cutoff periods shorter than 4.0 s, the same ratio shows a significant dependence on scale length. The calculated ratios are nearly equal to Σ_P based on an ionospheric model for long-wavelength structures and to $1/V_A$ for short-wavelength variations. The transition from the former to the latter usually begins around 4.0-8.0 s on the time scale. On the dayside the correlation between ΔB_z and E_x is generally high, and the transition is clearly seen. Thus the static model is applicable to variations of scale lengths greater than 8.0 s (or 64 km). For scale lengths below about 5 km (~0.6 s) the short-circuiting effect at ionospheric altitudes higher than the altitudes at which the horizontal Pedersen closure current usually flows becomes appreciable (*e.g.*, *Forget et al.*,1991). However, this effect alone cannot explain the observed decrease in the ratio $\Delta B_z/\mu_0 E_x$. The relation between the ratio $\Delta B_z/\mu_0 E_x$ and the solar zenith angle is consistent with the relationship between the Pedersen conductivity and the solar zenith angle in the published conductivity models. In chapter 3 of this paper, we compare the ratio $\Delta B_z/\mu_0 E_x$ observed by the DE-2 satellite for various spatial scales with the effective Pedersen conductivity $\Sigma_{P,eff}$ calculated by the method of *Forget et al.* The results show that in many cases this model can

adequately explain the observed scale-length dependence. However, cases exist in which the difference, $\Delta B_z/\mu_0 E_x$ - $\Sigma_{P,eff}$, decreases at about 0.25 - 1.0 s in temporal scales (2 - 8 km in spatial scales). This behavior is explained as being due to Alfvén waves. In chapter 4, we attempt to obtain the relation between the polar ionospheric conductivity on the nightside and the auroral luminosity deduced from the DE satellite observations. The height-integrated Pedersen conductivity, Σ_P, along the orbit of the DE 2 is calculated by using the method developed in the method of chapter 2. The luminosity along the DE 2 is obtained from the DE 1 VUV (vacuum ultraviolet) auroral imager. The relationship between the auroral luminosity obtained with 123W filter (I_{123W}) measured by the DE 1 and the Σ_P is rather complicated. The following results are obtained: (1) The I_{123W}-Σ_P relation shows a systematic invariant latitude dependence in many cases. That is, the peak of I_{123W} locates at higher latitude than that of Σ_P in most cases, however, this relation is reversed in some special cases. (2) In the equatorward part of the auroral oval on the evening side the I_{123W} and Σ_P are closely related and the ratios of these parameters are consistent with those obtained by *Robinson et al.*[1989]. (3) In the equatorward part of the auroral oval on the morning side, the correlation between I_{123W} and Σ_P is rather poor. (4) In the poleward part of the auroral oval both on the morning and evening sides the I_{123W}-Σ_P relation is different from that in the equatorward part of the oval, and the corresponding Σ_P for the same I_{123W} is smaller in the poleward part of the auroral oval than in its equatorward part. (5) Classifying in accordance with the energy of precipitating electrons, the I_{123W}-Σ_P relation shows a clear tendency. That is, Σ_P increasing for the same I_{123W} with increasing energy of precipitating particles. These results are consistent with the characteristic energy dependence of the I_{123W} and Σ_P suggested by *Rees et al.*[1988]. That is, when the characteristic energy is greater than about 2 keV, both I_{123W} and Σ_P are decreasing with increasing characteristic energy and the I_{123W}-Σ_P relation becomes insensitive to the characteristic energy. While, in lower characteristic energy less than about 2 keV, I_{123W} is decreasing but Σ_P is increasing with increasing characteristic energy of precipitating electrons, that is, the relation can be sensitive to energy of electrons.

Table of Contents

Acknowledgments i

Abstract ii

Table of Contents iv

1 General Introduction **1**

1.1 Magnetosphere-Ionosphere Interaction 1

1.2 Small-Scale Field-Aligned Currents 1

1.3 Ionospheric Conductivity 5

2 Correlation Between Magnetic and Electric Field Perturbations in the Field-Aligned Current Regions Deduced From DE 2 Observations **10**

2.1 Introduction 10

2.2 Method of Analysis 12

2.2.1 *Variation of the Ratio Between Magnetic and Electric Field Perturbations With Scale Length* 13

2.2.2 *Relation Between Ratio $\Delta B_z/\mu_0 E_x$ and Solar Zenith Angle* 14

2.2.3 *Polarity of Small-Scale Magnetic Perturbation* 15

2.3 Results 15

2.3.1 *Variation of the Ratio Between Magnetic and Electric Field Perturbations With Scale Length* 15

2.3.2 *Relation Between Ratio $\Delta B_z/\mu_0 E_x$ and Solar Zenith Angle* 19

2.3.3 *Polarity of Small-Scale Magnetic Perturbation* 20

2.4 DISCUSSION 21

2.5 CONCLUSION 25

3 Scale-Length Dependence of the Ratio Between the Magnetic and Electric Field Perturbations in the Ionospheric Field-Aligned Current Region 27

3.1 INTRODUCTION 27

3.2 METHOD OF ANALYSIS 28

3.2.1 *Model of Forget et al.* 28

3.2.2 *Observations* 29

3.3 RESULTS 30

3.4 DISCUSSIONS 32

3.5 CONCLUSIONS 33

4 Quantitative Relationship Between the Auroral Luminosity and the Ionospheric Conductivity in the Polar Region 35

4.1 INTRODUCTION 35

4.2 TECHNIQUE 38

4.3 RESULTS 41

4.3.1 *Case studies* 41

4.3.2 *Statistical results* 46

4.4 DISCUSSION 48

4.5 CONCLUSIONS 53

References 55

Figure Captions 61

Tables 67

Figures 69

Chapter 1

General Introduction

1.1 Magnetosphere-Ionosphere Interaction

The earth's magnetic field connects the ionosphere with the magnetosphere electromagnetically because the conductivity along the magnetic field (parallel conductivity)is relatively high. There are two main forms of transport of the electromagnetic energy from magnetosphere to ionosphere; Field-aligned current and Alfvén wave. Field-aligned currents transfer the energy as inflow and outflow of charged particles along the magnetic field lines. On the other hand, Alfvén wave transfers the energy as electromagnetic waves.

It is important subject to investigate the detail of electromagnetic energy injection to the ionosphere. *Iijima and Potemra* [1976] showed statistical field-aligned current structure in large scale by using the magnetic field data from Triad satellite observations. Figure 1 shows their results. In their study, it is noticed that a systematic large scale upward and downward current structure exists in the polar region.

1.2 Small-Scale Field-Aligned Currents

Sugiura[1984], and *Sugiura et al.*[1982,1983] presents a framework of study on field-aligned current or magnetosphere-ionosphere coupling from a very different point of view. That is, the field-aligned currents generally have fine structure and they mainly close meridionally through

the ionospheric Pedersen currents. This new framework is deduced from the fundamental relationship between the field-aligned currents and the magnetospheric convection electric field derived from the magnetic and electric field observations on the low altitude Dynamic Explorer 2 (DE 2) satellite. They showed that the variation of the north-south component of the electric field and those of the east-west component of the magnetic field are usually very similar and that the correlation coefficient between them is very high. They regard these magnetic and electric field perturbations as the static structure of the field-aligned current system, and examined the relation between the magnetic and electric field perturbations by using the following theoretical arguments: Let the x, y and z axis be toward north, up and eastward, respectively. The earth's main field is assumed to be vertical and downward. It is assumed that $\partial \Delta B_y/\partial t = 0$ and that ΔB_x is independent of z (*i.e.*, $j_\parallel = -(1/\mu_0)\partial \Delta B_z/\partial x$) where ΔB is the perturbation magnetic field. Then by equating $j_\parallel$ to the divergence of the height-integrated horizontal ionospheric current, it is obtained

$$\frac{\partial \Delta B_z}{\mu_0 \partial x} = \frac{\partial(\Sigma_P E_x)}{\partial x} + \frac{\partial(\Sigma_P E_z)}{\partial z} + E_z \frac{\partial \Sigma_H}{\partial x} - E_x \frac{\partial \Sigma_H}{\partial z} \tag{1.1}$$

where Σ_P and Σ_H are the height-integrated Pedersen and Hall conductivities. If E_z is independent of x and if the conductivities and E_z are independent of z, equation (1.1) can be integrated to give

$$\Delta B_z = \mu_0(\Sigma_P E_x - \Sigma_H E_z) + \text{const.} \tag{1.2}$$

If the observed values of ΔB_z are linearly correlated with those of E_x with a coefficient of correlation near unity over distances of several hundred kilometers along the x axis, it must be conclude either (a) that the north-south Hall current is zero and that

$$\Delta B_z = \mu_0 \Sigma_P E_x + \text{const.} \tag{1.3}$$

or (b) that E_z is always proportional to E_x. However, E_z was assumed to be independent of x

in deriving equation (1.2). Since E_x varies with x, the proportionality of E_z to E_x contradicts with this assumption. Therefore, (a) (*i.e.*, equation(1.3)) is the only choice. Equation (1.3) also means that the ratio, $\Delta B_z/\mu_0 E_x$ represent the height-integrated Pedersen conductivity, Σ_P, under the assumption that the constant is nearly zero.

On the other hand, *Gurnett et al.*[1984] interpreted these magnetic and electric field fluctuations in the field-aligned current region as a different phenomenon, *i.e.*, Alfvén waves. They investigated the height dependence of the ratio between magnetic and electric field perturbations observed by DE-1, and found that this ratio decreases rapidly with increasing height. They insisted that this height dependence is more fitted to Alfvén wave model than the static model. They also investigated the frequency dependence of the ratio $\Delta B/\Delta E (= V_A^{-1}, V_A$; Alfvén wave velocity) and show that the ratio tends to decrease with increasing frequency and is usually somewhat larger than the computed value of the Alfvén index of refraction. They mentioned that this difference comes from the reflection of Alfvén wave.

After these studies were published, many studies have been conducted by analyzing the relationship between the magnetic and electric field perturbations in the polar regions observed by polar orbiting satellite (*Israelevich et al.*, 1988, *Dubinin et al.*, 1990 by ICB-1300; *Knudsen et al.*, 1990 by HILAT and Rocket; *Matsuoka et al.*, 1991 by EXOS-D; *Berthelier et al.*, 1989, *Forget et al.*, 1991 by AUREOL-3; and *Weimer et al.*, 1985,1987 by DE-1/2, respectively. see also Table 2). In Chapter 2 we also investigate the relation between the magnetic and electric field perturbation in the ionospheric polar region. The characteristics and the advantages of our analysis comparing with others are as follows: (1) The method of analysis: In order to investigate the scale dependence of the ratio $\Delta B/\Delta E$, we use some digital filters in time-domain instead of spectrum method (in frequency domain). (2) Statistical results: We use large data set obtained by DE-2 observation and analyze the ΔB-ΔE relation in more general cases and

in better statistics than other studies. The studies shown in Table 2 are based on the data obtained in various altitude, but the result is generally similar each other. The correlation coefficient between the magnetic and electric field perturbations are generally high in the polar region and the ratio, $\Delta B/\Delta E$, is decreasing with increasing the frequency. But it is not clear until now which model, that is, static structure model or Alfvén wave model, is better to understand this phenomenon.

Recently, some studies attempted to explain this scale dependence of the ratio, $\Delta B/\Delta E$, using simulation method. *Forget et al.*[1991] interpreted the scale-length dependence of the ratio between the magnetic and electric field perturbations as being produced by the in which a field-aligned current closes its circuit at different the ionospheric altitudes depending on its scale length. They calculate the scale-length dependence of the height-integrated effective Pedersen conductivity, $\Sigma_{P,eff}$, solving the current continuity equation numerically. However, they also suggest a possibility of the presence of Alfvén waves.

On the other hand, *Knudsen et al.*[1992] interpret these perturbations as being produced by the reflection of Alfvén waves from the ionosphere. They use a model to compute the frequency-dependent amplitude and phase relations between the meridional electric and the zonal magnetic fields due to Alfvén waves.

In Chapter 3 of this paper, we compare the value of $\Sigma_{P,eff}$ estimated by the model of *Forget et al.*[1991] with the value of the ratio $\Delta B_z/\mu_0 E_x$ deduced from DE-2 observations. We examine to what extent the Alfvén wave effect exists in scale-length dependence of the ratio $\Delta B/\Delta E$ by subtracting the value of $\Sigma_{P,eff}$ from the ratio $\Delta B_z/\mu_0 E_x$ calculated from observation.

1.3 IONOSPHERIC CONDUCTIVITY

The ionized region of upper atmosphere from about 60 to 1000 km altitude is called ionosphere. The cause of this ionization is mainly the solar EUV radiation on the sunlit hemisphere. In addition, it cannot be ignored the effect of precipitating particles on the polar region. These precipitating particles also cause the aurora. *Rees* [1963] calculated the ionization and excitation rate by the particles with various energy. After this paper was published, in many studies it is calculated the relation between the energy of precipitating particles and auroral luminosity using the method by *Rees* [1963].

Various techniques have been used in order to deduce the ionospheric conductivity such as; (1) incoherent scatter radar, (2) multispectral auroral imager, (3) ground-based magnetometers, (4) precipitating particle data obtained by polar orbiting satellite, and (5) the magnetic and electric field perturbation data obtained by polar orbiting satellite.

The most popular method to deduce the ionospheric conductivity is to measure the particle density and drift velocity by using incoherent scatter radar. In this method, we can obtain the data with high temporal ($\sim$ about 10 s) and spatial resolution. Over the past decades, many studies attempted to construct conductivity models from the data obtained by the incoherent scatter radars in polar regions [*Mehta*, 1979; *Senior*, 1980; *Vickrey et al.*,1981; *de la Beaujardiere et al.*,1982; *Robinson and Vondrak*, 1984; *Schlegel*, 1988; *Rasmussen et al.*, 1988; *Brekke and Hall*, 1988; and *Senior*, 1991]. From these studies, they constructed ionospheric conductivity models in the sunlit polar region having a solar-zenith angle and solar activity dependence. However, the polar radars do not operate for periods long enough to obtain a 2-dimensional distribution of conductivity. In addition, radar observation have a latitudinal limitation of investigation.

Some researches attempted to deduce the precipitating particle energy and the ionospheric conductivities from the multispectral auroral images. The principle of this method is as follows: The higher energy particles can penetrate into the ionosphere deeper than the lower energy particles. The neutral particle density in the ionosphere, and hence collision frequency with them is increasing with descending the altitude. By this reason, in the lower ionosphere, particles tend to loss their energies by collision before emitting from the excited state. This "quenching" phenomenon is especially significant in the case of the emission which has relative long time delay between excitation and emission, for example, 630.0 nm (time delay $\sim$ 110 s) and 557.7 nm ($\sim$ 0.7 s). While, 427.8 nm emission is not sensitive this quenching effect because this emission has small time delay between excitation and emission. From this reason, with increasing particle energy, the quenching effect for 557.7 nm and 630.0 nm become significant and the intensity ratio, $I(557.7nm)/I(427.8nm)$ and $I(630.0nm)/I(427.8nm)$ decrease. *McEwen and Bryant* [1978] shows the relation between particle energy and intensity ratio quantitatively. Figure 2 shows that the ratio $I(630.0nm)/I(427.8nm) \sim 6$ in 500 eV of particle energy, while it become $\sim$ 0.1 in 5 keV.

Eather and Mende [1971] deduced the auroral energy deposition rate, mean energy and ionospheric conductivity from the ratio of auroral intensity by using ground-based multispectral auroral image data. *Rees et al.*[1988], *Lummerzheim et al.*[1991] and *Rees* [1992] applied this method to construct maps of the characteristic energy and the energy flux from the multispectral auroral images on DE 1. This method provide the conductivity distribution with high time resolution and over large region, but the results are not so accurate. *Mende et al.*[1984] compared the value of ionospheric conductivities deduced from the ratio of luminosity with those deduced from radar observations. Their results shows a general agreement between the results obtained from two different methods. However, the value of conductivity deduced from

the intensity ratio tend to have large scatter with increasing the conductivity.

Some studies attempt to deduce the ionospheric conductivity distribution from the data obtained by many ground-based magnetometers. *Kamide et al.*[1981] estimated the distribution of ionospheric electric fields as following steps, which is called KRM method: (1) Calculation of the equivalent ionospheric current function from geomagnetic H and D component observed on the earth's surface, (2) Computation of the electric potential distribution from the equivalent ionospheric current function by using a simple model of the ionospheric conductivity, (3) Derivation of ionospheric current vectors as well as electric fields and, (4) Derivation of the field-aligned current intensity by taking the divergence of the ionospheric currents. As their results are very sensitive to the given conductivity model, *Kamide et al.*[1986,1989] calculated the electric field and current distributions at high latitudes by means of the KRM magnetogram inversion technique and examined the accuracy of these calculations by changing the conductivity distribution iteratively until the calculated electric fields become consistent with electric fields inferred from ion drift measurements made by DE 2.

However, this method require widely distributed geomagnetic data, and the spatial resolution with this method is not so good as other methods because the distance among observatories is, in general, more than 500 km.

Another method to infer the ionospheric conductivities is to use the precipitating particle data obtained by polar orbiting satellite. *McDiarmid et al.*[1975] used the data from ISIS 2 spacecraft to determine average intensities and energies of auroral electrons as a function of magnetic local time and invariant latitude for periods of relatively low geomagnetic activity ($K_P \leq 3_0$). *Wallis and Budzinski* [1981] used these data as well as further unpublished ISIS 2 results for periods of higher magnetic activity to infer the local time and invariant latitude dependent electrical conductivity within the auroral zone for quiet and active geomagnetic

conditions. More recently, *Spiro et al.*[1982] have constructed an average conductivity model for four amplitude ranges of the AE index (the so-called Rice University model).

From this method we can obtain the "statistical" ionospheric conductivity distribution, but cannot obtain the "snap-shot" ones. In addition, we cannot estimate the contribution of solar EUV radiation for ionization, and the calculated conductivities underestimate the actual ones in the sunlit hemisphere.

There is another method to deduce the ionospheric conductivity from the magnetic and electric field perturbations observed by polar orbiting satellite. In Chapter 2, we show that the ratio of the magnetic to electric field perturbations, $\Delta B_z/\mu_0 E_x$ represents the Pedersen conductivity, Σ_P when the scale of these perturbations are greater than about 8 km. By applying this result, the ionospheric Pedersen conductivities can be deduced with simple calculations. The conductivity estimated by this method includes the effects of both solar EUV and precipitating particles. The time resolution and accuracy is high when the correlation between the magnetic and electric field perturbation is high. However, the Hall conductivity cannot be estimated by this method, and it is difficult to estimate even the Pedersen conductivity when the correlation between the magnetic and electric field is poor.

As is discussed above, the each method has it's own limit to deduce accurate 2-dimensional distribution of polar ionospheric conductivity. To supplement their limitations, several studies analyzed the quantitative relationship between the auroral luminosity observed by polar orbiting satellite and ionospheric conductivities, in order to estimate the conductivity from auroral image data taken by satellite.

Robinson et al.[1988] compared the ionospheric conductivities deduced form the data obtained Chatanika radar with the VUV (vacuum ultraviolet) image observed by DE 1.

Conductivity estimated by KRM method in *Kamide et al.*[1986,1989], and estimated by mul-

tispectral method in *Rees et al.*[1988], *Rees*[1990] and *Lummerzheim et al.*[1992] are compared with auroral image data observed by DE 1.

In Chapter 4 of this paper, we compare the auroral luminosity observed by DE 1 and the ratio between the magnetic and electric field perturbations observed by DE 2. From this analysis, we obtain a new result showing that the relation between the auroral luminosity and Pedersen conductivity depend on the energy of precipitating particles.

Chapter 2

Correlation Between Magnetic and Electric Field Perturbations in the Field-Aligned Current Regions Deduced From DE 2 Observations

2.1 Introduction

The field-aligned currents play an important role in the ionosphere-magnetosphere coupling. Extensive studies have been made of the relationships between field-aligned currents, electric and magnetic fields, and particle precipitation using data from satellites, sounding rockets, and ground-based radars. Simultaneous observations of magnetic and electric fields have been made by the S3-2 and S3-3 satellites [*Burke et al.*, 1980; *Smiddy et al.*, 1980; *Rich et al.*, 1981] and by a combination of ground-based radar observations and TRIAD magnetometer measurements [*Robinson et al.*, 1982]. The correlation between magnetic and electric field fluctuations in the field-aligned current regions has also been analyzed using data obtained by DE 2 [*Sugiura et al.*, 1982, 1983; *Sugiura*, 1984], DE 1 [*Gurnett et al.*, 1984], ICB 1300 [*Dubinin et al.*, 1990], a sounding rocket and HILAT [*Knudsen et al.*, 1990], EXOS D [*Matsuoka et al.*, 1991], and AUREOL 3 [*Forget et al.*, 1991].

Observations indicate that the orthogonal components of the magnetic (**B**) and electric (**E**) field perturbations are highly correlated especially in the sunlit hemisphere. If the orthogonal **B** and **E** field variations are assumed to be proportional, an integration over ionospheric height of the steady state divergence-free condition on the current density yields a differential

equation, which has a particular solution giving the relationship by which the ratio of the orthogonal components of the **B** and **E** field variations represents the height-integrated Pedersen conductivity Σ_P :

$$\Delta B_z/(\mu_0 E_x) = \Sigma_P \tag{2.1}$$

where the x and z axes are oriented in the direction of the (DE 2) spacecraft motion (north-south) and the east-west direction, respectively, and where μ_0 is the magnetic permeability in vacuum [*Sugiura*, 1984]. This is the basis of what is called the static model below.

Gurnett et al. [1984] presented an alternative interpretation that the **B** and **E** field perturbations observed by DE 1 are Alfvén waves. In this model the Alfvén velocity is given by the ratio of the orthogonal **E** and **B** field perturbations; that is, expressing this relationship in terms of the DE 2 spacecraft coordinates, we have

$$\frac{E_x}{\Delta B_z} = V_A \tag{2.2}$$

Weimer et al. [1985, 1987] analyzed the **B** and **E** field fluctuations using data obtained by DE 1 and 2 in magnetic conjunctions; they found that large-scale electric field perturbations observed by the two spacecraft are approximately equal when reduced to a common reference altitude and that the relationship between **E** and Δ**B** is consistent with the static model. *Vickrey et al.* [1986] examined the fluctuations of high-latitude **E** and **B** fields with scale sizes between 3 and 80 km using data from the ion drift meter and magnetometer on board the HILAT satellite and found that for these scale sizes the magnetosphere tends to behave as a source of steady current independent of ionospheric conductivity.

In this paper we investigate the dependence of the Δ**B** to **E** ratio on spatial scale, using the electric and magnetic field data obtained by DE 2 in the polar regions. Values of this ratio are compared with the Pedersen conductivity inferred from the international reference ionosphere

model (IRI-86 model [see *Bilitza*, 1986]) and the Alfvén wave velocity calculated from the in situ ion density and magnetic field measurements. Most of the studies mentioned above investigated the ratio between the magnetic and electric fields by using power spectral analysis, while in this study the ratio is calculated by the least squares method directly from numerically filtered electric and magnetic field data. In the analysis by the least squares method the reliability of the ratio can be examined by the correlation coefficient, and the variation of the ratio along the spacecraft orbit is determined by a "dynamic" correlation method. We examine the relation between the ratio $\Delta B_z/\mu_0 E_x$ and the solar zenith angle and compare the results with published conductivity models [*Mehta*, 1979; *Senior*, 1980; *Vickrey et al.*, 1981; *de la Beaujardiere et al.*, 1982; *Robinson and Vondrak*, 1984; *Schlegel*, 1988; *Rasmussen et al.*, 1988]. Lastly, we show an example of an Alfvén wave and discuss the scale size dependence of the $\Delta\mathbf{B}$ to $\mathbf{E}$ ratio.

2.2 METHOD OF ANALYSIS

The Dynamics Explorer (DE) 2 spacecraft was launched on August 3, 1981, into a polar orbit with initial apogee and perigee at 1003 km and 299 km altitude, respectively. Vector magnetic field data were obtained by a triaxial flux gate magnetometer, with resolution of $\pm$ 1.5 nT in the basic mode and with a sampling rate of 16 vector samples per second [*Farthing et al.*, 1981]. Vector electric field measurements were made by a symmetric double floating probe system with a sensitivity of 0.1 mV m^{-1} and a range $\pm$ 1V m^{-1}[*Maynard et al.*, 1981]. One of the horizontal antennas (i.e., along the Z axis) did not deploy after launch.

In this study, data for the north-south (X) component of the electric field and the east-west (Z) component of the magnetic field are used. The X component is along the spacecraft velocity vector and is therefore approximately in the geographical north-south direction. The $v \times B$

electric field from the satellite motion, the corotation electric fields, and the contact potential differences are subtracted from the observed electric field. The Earth's internal magnetic fields calculated from a Magsat model [*Langel et al.*, 1980] are subtracted from the observed magnetic fields.

2.2.1 *Variation of the Ratio Between Magnetic and Electric Field Perturbations With Scale Length*

Figure 3 shows an example of the deduced **B** and **E** field data. The curves for ΔB_z and E_x are very similar. The scatter plot between ΔB_z and E_x is shown in Figure 4. The correlation coefficient between them is 0.96.

The ratio $\Delta B_z/E_x$ represents the Pedersen conductivity Σ_P in the static model and the inverse of the Alfvén wave velocity, $1/V_A$, in the Alfvén wave model. Therefore we compare the ratio $\Delta B_z/E_x$ based on the observation with a Σ_P model (IRI-86) and with $1/V_A$ estimated from the in situ measurements of the magnetic field and plasma density measurements.

A digital filter with variable cutoff/passband periods shown in Table 1 is used to examine the scale length dependence of the ratio $\Delta B_z/E_x$. The filter used is a nonrecursive digital filter, whose transfer function has insignificant sidelobe effects near the cutoff frequencies. For large-scale variations, 0.5-s averages are used, while for analysis of short-scale variations, high time resolution data at the sampling rate of 16 per second are used. Both 0.5-s-averaged data and high time resolution data are compared for intermediate scales (1-4 s) in order to examine whether 0.5-s-averaged data give the same results as high time resolution data. It should be noted that unless the correlation coefficient between the magnetic and electric fields is high, the interpretation of the ratio $\Delta B_z/E_x$ is not straightforward. The correlation is generally high with the data which are obtained in the sunlit hemisphere and which are not filtered or are

filtered with long cutoff periods. The correlation tends to decrease when a filter with a short cutoff/passband period is used or when data are taken in the dark hemisphere, as is shown later.

The Pedersen conductivity Σ_P is calculated from the ion species, densities, and temperature given by the IRI-86 model along the spacecraft orbit. The value of Σ_P changes as the spacecraft moves with high velocity over a region in which the conductivity varies rapidly. The maximum and minimum conductivity values based on the IRI-86 model are given in Figure 5. The Alfvén wave velocity V_A is calculated from the magnetic field and the ion density observed by DE 2. Since the ion species and the mixing ratio are not exactly known, V_A is calculated for two extreme cases, i.e., for an O^+ dominant plasma and for an H^+ dominant plasma. We have examined the dominant ion under various circumstances by using the IRI-86 model and have found the H^+ ion is dominant at altitudes over 600 km in the polar ionosphere at winter midnight under solar minimum and that the O^+ ion is dominant under the other conditions.

2.2.2 *Relation Between Ratio $\Delta B_z/\mu_0 E_x$ and Solar Zenith Angle*

Next, we calculate a "dynamic" correlation to investigate the relation between the solar zenith angle and the ratio $\Delta B_z/E_x$ in the sunlit region. The correlation coefficient between ΔB_z and E_x and the ratio of ΔB_z to E_x are calculated for a sliding "data window" of 10 s, which is short compared with the scale length of the conductivity variation.

In the analysis of this section a high-pass filter with a 30-s cutoff period is used to reduce influences of low-frequency trends stemming from uncertainties in the satellite attitude determination. As mentioned earlier, interpretation of the value $\Delta B_z/E_x$ is difficult when the correlation coefficient is low, and therefore the intervals in which the correlation coefficient is

below 0.75 are not included in the discussion except where specifically indicated.

2.2.3 *Polarity of Small-Scale Magnetic Perturbation*

Lastly, we examine the polarity of small-scale magnetic field perturbations transverse to the main field to investigate wavelike structures in the magnetic field for the cases in which the correlation is high. The polarization in the magnetic field perturbation was examined if the Z component of the magnetic field was well correlated with the X component of the electric field. Hodographs for the magnetic field perturbations were made using a high-pass filter with a cutoff period of 0.5 s. Since the Z component of the electric field was not measured, the polarization in the electric field cannot be examined by direct observation.

2.3 RESULTS

2.3.1 *Variation of the Ratio Between Magnetic and Electric Field Perturbations With Scale Length*

A total of 156 intervals were analyzed, of which 129 represent auroral oval traversals and the remaining 27 are segments of auroral oval traversals. The data period we used is from September 1981 to December 1982, covering all local times. When the sample length is too long, the correlation becomes low because the ratio (i.e., the Pedersen conductivity or the Alfvén wave velocity) changes within the sampled interval. On the other hand, if this interval is too short, the correlation coefficient can become statistically unreliable because too few data points were used. For these reasons we analyzed the data for a time interval of about 30 s to a few minutes in length in each run of the correlation calculation. When the perturbation region is wide in latitude, we divide the region into a few sections, each section forming a sample.

The correlation between the magnetic field perturbation ΔB_z and the orthogonal electric field component E_x is very high in many cases. Ninety-nine of the 129 examples have correlation coefficients greater than 0.75. When a band-pass filter with a short passband period is used, the correlation coefficient generally decreases. Average values of $\Delta B_z/E_x$ are equal to the average $\mu_0\Sigma_P$ for large scales (cutoff period of >8.0 s, spatial scale >64 km). The average ratio decreases with decreasing scale and approaches the reciprocal of the Alfvén wave velocity, $1/V_A$.

A typical example of the variation of the ratio is shown in Figure 5. The horizontal axis represents the passband period of the band-pass filter. Since the band-pass filter has two cutoff frequencies at both ends, the ratio is plotted at the center of the corresponding band. The numbers indicated at the top or the bottom of the plot give values of the correlation coefficient between ΔB_z and E_x. The upper numbers were obtained using 0.5-s averages (cutoff period $\geq$ 1.0 s), and the lower numbers using high time resolution data (cutoff period $\leq$ 4.0 s). The standard deviation of the differences between the individual ratios $\Delta B_z/\mu_0 E_x$ and the ratio determined by the least squares fitting is shown by vertical bars, the relative magnitude of the errors ranging from 0.83 to 2.23%. Similar plots for 20 examples are shown in Figures 6 and 7. The case labeled (a) in Figure 6 was observed near the terminator. The Σ_P deduced from the IRI-86 model (the average value for each pass) is indicated by the asterisk at the extreme right (i.e., on the right-hand axis) which is connected by a dotted line to the data for the same pass. The Alfvén wave velocity calculated from the observed plasma density and magnetic force data (assuming O^+ ions dominant) is likewise indicated by the asterisk at the extreme left (on the axis) connected by a dotted line to the rest of the data for the same pass.

Most of the plots given in Figure 6 for the dayside show a tendency for the ratio to become smaller with decreasing scale length, although the critical scale length at which the decrease begins varies from one case to another. The results from the nightside data given in Figure 7

indicate that many fewer nightside cases show this tendency than for the dayside and that for an appreciable fraction of the cases the ratio is nearly flat. Two cases show large decreases below 1.5-3 s. One of these two cases, marked (b) in Figure 7, had an off-scale point at 8-16 s; this case was observed during a magnetically disturbed period as is discussed later. In Figures 6 and 7, intervals for which the correlation coefficient is less than 0.5 are indicated by asterisks with no connecting lines. Cases where the correlation coefficient is <0.5 are much more numerous among the nightside events (Figure 7) than for the dayside (Figure 6).

Figure 8 shows a comparison of Σ_P estimated from the ΔB_x to E_y ratio with that calculated from the IRI-86 model and a comparison of V_A estimated from the E_y to ΔB_x ratio with that calculated from the observed plasma density and the magnitude of the magnetic field. In Figures 8a and 8b, the vertical axis represents the ratio of observed ΔB_x to E_y, and the abscissa represents the value based on the model. The horizontal bar of the IRI-86 model value shows the range of Σ_P along the orbit in the observing period. In Figure 8c, the vertical axis represents the observed E_y to ΔB_x ratio, and the abscissa the value calculated from the plasma density and the magnetic field magnitude. Cases in which the correlation coefficient exceeds 0.75 are plotted. For the data shown in Figures 8a and 8b, band-pass filters with passband periods 16.0-32.0 s and 0.5-1.0 s, respectively, are used. These panels show that for large scales (passband period 16.0-32.0 s) there is a good agreement between the observation and the model; while for small scales (passband period 0.5-1.0 s) the estimates from the ΔB_x to E_y ratio are generally smaller than those based on the model. Figure 8c shows variations of the ratio E_y to ΔB_x with decreasing scale length. The asterisk represents the ratios for large scales (passband period 16.0-32.0 s), and the caret represents the ratios for small scales (passband period 0.25-0.5 s). Values of the ratio in each pass tend to approach the value of V_A (O^+).

The dayside ionospheric conductivity is primarily determined by the solar EUV (and X

ray) radiation. It is therefore expected that the conditions of the ionosphere-magnetosphere coupling change significantly when the terminator is crossed. Thus the data are classified into three categories: dayside, nightside, and near the terminator. Here the terminator was calculated by the method described by *Woolf* [1968]. The terminator position depends on altitude and changes about 20° in latitude depending on whether the Earth's atmosphere is transparent or opaque with respect to the solar EUV radiation. If we regard the position of the maximum gradient of the Pedersen conductivity Σ_P based on the IRI-86 model as the terminator at the ionospheric height, we find that the position of the terminator at spacecraft altitudes is nearly equal to that at the ground.

On the dayside the ΔB_z to E_x ratio generally tends to decrease with decreasing cutoff period, and the ratio tends to be constant for relatively long (>8.0 s) cutoff periods. Data marked (a) in Figure 6, which were taken near the terminator, do not show this tendency. The critical scale length where the ratio starts to decrease varies from one example to another, as seen in Figure 6, and cannot be determined uniquely on the basis of such plots as Figure 6. However, statistically speaking, the ΔB_z to E_x ratio is constant for cutoff periods greater than 8 s. It is not clear what parameter controls the critical scale length. For large scale lengths the value of the ratio $\Delta B_z/\mu_0 E_x$ is nearly equal to the Pedersen conductivity estimated from the IRI-86 model. However, there are cases in which strong high-energy particle precipitation exists when this ratio is much larger than is expected from the model.

The correlation between ΔB_z and E_x is generally lower on the nightside than on the dayside, and in some samples almost no correlation is found even for large scales. Especially under disturbed conditions (AE > 700 nT), the correlation is very poor; the correlation coefficient in nine of twelve disturbed cases was less than 0.6. When magnetic activity is low (AE < 100 nT), most of the data showed a good correlation; 25 of 30 examples showed correlation

coefficients greater than 0.75. The dependence of the correlation on the AE index is smaller on the dayside. Another characteristic on the nightside is that the correlation is high only in limited cutoff period domains. The variation of the ΔB_z to E_x ratio with scale length is not as clear on the nightside as on the dayside (see Figure 7). Some cases show that the ratios $\Delta B_z/\mu_0 E_x$ are quite large. The period of the case labeled (b) in Figure 7 was magnetically disturbed (AE= 918 nT). We have no particle precipitation data for this period. It should be noted that on the nightside the Pedersen conductivity is generally low but the Alfvén velocity is large, and hence the two tend to approach each other.

Next, we examine the cases near the terminator (see Figure 6, data (a)). The $\Delta B_z/\mu_0 E_x$ variation is characterized by a mixture of cases on the dayside and on the nightside. The correlation between ΔB_z and E_x near the terminator is generally less than that on the dayside but better than on the nightside. However, it is difficult to compare the observed ratio $\Delta B_z/\mu_0 E_x$ with the value calculated from the IRI-86 model near the terminator, because the gradient of the Pedersen conductivity is large near the terminator. In most examples (10 out of 14) the ratio tends to become small when the cutoff period of the filter becomes short.

2.3.2 *Relation Between Ratio $\Delta B_z/\mu_0 E_x$ and Solar Zenith Angle*

We analyze the relation between the ratio $\Delta B_z/\mu_0 E_x$ and the solar zenith angle, using the "dynamic" correlation method. The width of the data window is 10.0 s, and a high-pass filter with cutoff period of 30 s is used. Twenty-three cases are analyzed, an example of which is shown in Figure 9. The top panel shows the variation in the ratio $\Delta B_z/\mu_0 E_x$ along the orbit, and the bottom panel the correlation coefficient between ΔB_z and E_x. When the correlation coefficient is under 0.75, the ratio is not plotted. A general trend of monotonic decrease in the

ratio along the orbit is seen. We calculate the solar zenith angle along the orbit and show in Figure 10 the relationship between the solar zenith angle and the ratio $\Delta B_z/\mu_0 E_x$, using 20 examples chosen with criteria that the pass is near the terminator and that solar activity is relatively high. The ratios for which the correlation coefficient is over 0.75 are averaged within intervals of 0.5° in zenith angle, and these average ratios are plotted with dots in Figure 10. The irregular curve represents the total average ratio within intervals of 0.5° in zenith angle. It is clear from this figure that the ratio increases with decreasing solar zenith angle.

Next, these results are compared with the published Pedersen conductivity models whose parameters include the solar zenith angle [*Mehta*, 1979; *Senior*, 1980; *Vickrey et al.*, 1981; *de la Beaujardiere et al.*, 1982; *Robinson and Vondrak*, 1984; *Rasmussen et al.*, 1988; *Schlegel*, 1988]. Some models include a solar activity index as one of the parameters. In Figure 10, we used a data period with the sunspot number exceeding 130, because solar activity should be nearly equal for comparison.

In Figure 10 we superimposed seven traces on each other which are calculated on the basis of seven published Pedersen conductivity models. The model published by *de la Beaujardiere et al.* [1982] agrees well with the lower envelope of our results.

2.3.3 *Polarity of Small-Scale Magnetic Perturbation*

There are 68 examples in which the correlation coefficients are large even for small scale lengths. There are some cases where the hodograph clearly shows a rotation (Figure 11), suggesting that the fluctuation is an Alfvén wave. However, in most cases the polarization is very complicated.

2.4 DISCUSSION

The purpose of this paper is to investigate the relationship between the magnetic and electric field perturbations in the field-aligned current region. There are two models to explain the relationship. One is the static model, and the other is the Alfvén wave model. While the ratio $\Delta B_z/E_x$ represents the height-integrated Pedersen conductivity Σ_P in the static model, the same ratio gives the reciprocal of the Alfvén wave velocity in the Alfvén wave model. Therefore the ratio is compared with $\mu_0 \Sigma_P$ and $1/V_A$ for perturbations of various scale lengths by applying band-pass filters with various cutoff periods to the data. It is found that the ratio $\Delta B_z/E_x$ has little variation with scale length for the data processed with filters having cutoff periods greater than 8 s (or 64 km in length) and that the ratio is nearly equal to the Σ_P calculated from the IRI-86 model. Therefore the static model is applicable to scale lengths greater than 8 s (or 64 km).

Most of the examples for large scales in which the ratio does not agree well with the Pedersen conductivity model are from intervals of relatively high AE activity. The reason for this may be that the IRI-86 model underestimates Σ_P because this model does not include the effect of particle precipitation, and more importantly that the situation is time-dependent. Generally speaking, there is auroral particle precipitation in these cases.

When we compare the results for the dayside with those for the nightside, the ratio $\Delta B_z/E_x$ on the dayside is found to be greater than that on the nightside, and the correlation coefficients between ΔB_z and E_x on the dayside are generally greater than those on the nightside. The lower correlation between ΔB_z and E_x on the nightside is considered to be largely due to time-dependent situations related to high magnetic activity. The dominant source of ionization in the dayside ionosphere is solar EUV, and hence the ionization is quasi-stationary. In contrast,

the ionization of the nightside ionosphere in the auroral zone is mainly caused by particle precipitation, which usually is highly variable in time and space.

Analyzing the variation of the ratio along the orbit, we have shown that the ratio $\Delta B_x / \mu_0 E_x$ depends on the solar zenith angle. The Pedersen conductivity based on the model of *de la Beaujardiere et al.* [1982] follows closely the lower envelope of variation of $\Delta B_x / \mu_0 E_x$ with solar zenith angle (Figure 10). This is a reasonable result, because this model takes into account the effect of ionization by the solar EUV radiation only, excluding the contribution from particle precipitation.

Errors in Σ_P as deduced by the present method depend on the correlation between ΔB_z and E_x. On the dayside the correlation coefficient between ΔB_z and E_x is generally very high. For example, when the correlation coefficient between ΔB_z and E_x is over 0.8, the estimated error in Σ_P is a few percent. On the other hand, *Senior* [1991] noticed that the error in Σ_P deduced from radar observations is about 15% because of the assumptions regarding ionospheric temperature and density.

Another finding of this study is that the magnetic to electric field ratio decreases with increasing frequency. Two types of interpretation are possible. One is that the electric and magnetic perturbations are static structures on large scales, whereas small-scale perturbations are Alfvén waves; as the scale length becomes smaller, the ratio $\Delta B_x / E_x$ changes over to $1/V_A$, which is generally smaller than the Pedersen conductivity. Another type of interpretation is that the origin is static in nature even for small scales but the closure of the current in the ionosphere on small scales is different from that on large scales. The point of the latter interpretation is that the field-aligned portion of the current circuit in the ionosphere becomes longer than the horizontal, cross-field portion of the circuit as the horizontal scale decreases and that the parallel resistance might not be negligible compared with the Pedersen resistance

[e.g., *Reid* ,1965]. *Forget et al.* [1991] explain the frequency dependence of the ratio $\Delta B_z/E_x$ by this effect. However, this effect seems to be insufficient to explain the decrease of the ratio with decreasing scale length found in many cases dealt with in this paper. We followed Forget et al.'s calculation using the IRI-86 model and generally confirmed their result that the spatial wavelength below which the effect is important is typically 5 km. However, according to the present analysis, the observed ratio of $\Delta B_z/E_x$ begins to decrease at about 4 s (32 km in spatial scale) in many cases. Forget et al. give only two examples of observation; therefore we believe that there is no fundamental conflict between the views of Forget et al. and ours. Indeed, upon close examination, one of the examples given by Forget et al. (i.e., orbit 5848 N in their Figure 4) shows that the observed ratio begins to show an appreciable decrease at wavelengths somewhat greater than 10 km. This situation is similar to some of the examples shown in our Figure 6. We believe that the discrepancy between the observation and the theoretical result on the short-circuiting effect of higher ionospheric altitudes is due to the Alfvén wave effect, although we recognize the effect of scale size on the ionospheric conductance.

In Figures 6 and 7 we see a tendency for the gradient of the ratio $\Delta B_z/E_x$ at small scales to be steep when the ratio for larger scales is large. The local V_A, which is proportional to $n^{-1/2}$, varies much less with solar zenith angle than does the Pedersen conductivity, which is proportional to n^2 where n is the electron density. Therefore the above tendency is consistent with the deduction that small-scale perturbations in the magnetic and electric fields contain a significant amount of Alfvén waves.

One possible explanation of the transition from the static field-aligned current model to the Alfvén wave model may be given as follows: The generation of small-scale field-aligned currents is related to the irregular structures of the plasma in the magnetosphere, and the power spectral densities of the irregularities would decrease as the spatial scale decreases. On the other hand,

Alfvén waves generated in the magnetosphere may produce power spectral peaks near a few seconds in period at high latitudes, and the power in these Alfvén waves may exceed that in the irregular structures in small-scale field-aligned currents. *Iyemori* [1988] reported from cross-spectral analysis of the Magsat magnetic field observations that in the higher-frequency range (1.0-2.0 Hz) the R mode statistically dominates the L mode in the auroral region, whereas for the lower frequency range (0.125-0.25 Hz) the L mode dominates and covers most of the polar region. This result clearly demonstrates the presence of Alfvén waves in small scales.

We now examine the polarity of the magnetic perturbation for the cases in which magnetic and electric fields are well correlated on small scales as well as on large scales. Results indicate that most of these examples show several cycles of rotation of the magnetic field vector (e.g., Figure 11). Although the polarization characteristics cannot always be uniquely defined, we conclude that the small-scale magnetic and electric field perturbations contain a significant amount of Alfvén wave component. However, these waves may be localized waves, because cross-spectral analyses for relatively wide data intervals generally do not show any systematic polarization characteristics. There are intervals, however, during which left-handed polarization is clearly identified, suggesting the possibility that these waves may be of ion cyclotron wave origin. A circular polarization could also be observed when the satellite passes a line current structure. However, each line current produces only 180° of rotation at the most. To explain such rotations as are seen in Figure 11, the spacecraft has to pass through many line currents that are placed in suitable positions, but the probability of having such a distribution of line currents should be very small.

It is of interest to find the critical parameter or parameters that control the degree of importance of the Alfvén waves. The transition from the static to Alfvénic structures occurs in most cases between the scale sizes of 4.0-8.0 s (32-64 km on spatial scales). The main reason for

the scale length dependence of the ratio of $\Delta B_z/E_x$ is the transition from static structures to Alfvén waves. However, it is noted here that the real situation is complex because of the effects of the reflected waves from the ionosphere. Discussion of this subject is outside the scope of this paper and will be given in a separate report.

2.5 CONCLUSION

We analyzed the correlation between the magnetic and electric field perturbations observed by the DE 2 satellite using band-pass filters to determine the scale length dependence of the ratio of the magnetic to electric field perturbations. Results can be summarized as follows.

1. The observed ratio $\Delta B_z/\mu_0 E_x$ agrees well with a Pedersen conductivity (Σ_P) model on large scales (8-32 s band-pass filters; 64-256 km on spatial scales). Therefore the large-scale perturbations are interpreted as being static structures.

2. The ratio $\Delta B_z/\mu_0 E_x$ shows a solar zenith angle dependence in accordance with the published ionospheric conductivity models.

3. In most cases the ratio on small scales (cutoff period of filter of <2.0 s; spatial scale lengths of <16 km) is smaller than that on large scales and approaches the local Alfvén wave velocity.

4. The decrease in the ratio for short wavelengths is partly due to the short-circuiting effect at higher ionospheric altitudes. However, this effect by itself cannot explain the observed decrease in the ratio.

5. The critical scale length at which the transition from static structures toward Alfvén waves begins is, in general, between 4 and 8 s (32 and 64 km in length scale).

6. In some cases a left-handed polarization is seen in the magnetic perturbation, suggest-

ing the existence of ion cyclotron waves.

Chapter 3

Scale-Length Dependence of the Ratio Between the Magnetic and Electric Field Perturbations in the Ionospheric Field-Aligned Current Region

3.1 INTRODUCTION

Small scale magnetic and electric field perturbations have been observed in the field aligned current region in the ionosphere by polar-orbiting satellites. The following results have been obtained from the observations (Table 1): (1) Correlation between the magnetic and electric field perturbations observed in the ionospheric field-aligned current region, especially on the dayside, is often very high. (2) The ratio between the magnetic and electric field perturbation has a scale-length dependence. The ratio $\Delta B_x/E_x$ decreases with decreasing temporal or spatial scale length. There are two interpretations regarding the reason for the correlation between the magnetic and electric field perturbations. One uses a static model; the observed perturbations are regarded as being static spatial variations, and the ratio of the orthogonal magnetic and electric field components, $\Delta B_x/E_x$, represents the height-integrated Pedersen conductivity, Σ_P. The other uses an Alfvén wave model; the observed perturbations are interpreted as being Doppler-shifted Alfvén waves, and the inverse of the ratio gives the Alfvén wave velocity, V_A. The observed perturbations in the magnetic and electric fields may represent a complex mixture of these effects.

Forget et al.[1991] interpreted the scale-length dependence of the ratio between the magnetic and electric field perturbations as being produced by the circumstance that the manner in which a field-aligned current closes its circuit in the ionosphere depends on its scale length. However,they also suggest the possibility of a presence of Alfvén waves. They calculate the scale-length dependence of the height-integrated effective Pedersen Conductivity, $\Sigma_{P,eff}$, solving the current continuity equation numerically.

In this paper, we compare the value of $\Sigma_{P,eff}$ calculated by the model of *Forget et al.* with the value of the ratio $\Delta B_z/\mu_0 E_x$ deduced from DE-2 observations. We examine to what extent the Alfvén wave effect exists in scale-length dependence of the ratio $\Delta B_z/E_x$ by subtracting the value of $\Sigma_{P,eff}$ from the ratio $\Delta B_z/\mu_0 E_x$ calculated from observation.

3.2 METHOD OF ANALYSIS

We compare the ratio between the magnetic and electric field perturbations deduced from the model, which is the same as that used by *Forget et al.*[1991], with the ratio based on the observations by DE-2 for 20 examples.

3.2.1 *Model of Forget et al.*

The Fourier transformed electrostatic potential, Φ_k, with wave number k in the ionosphere satisfies the following equation (eq.(5) in *Forget et al.*,1991):

$$\frac{d^2\Phi_k}{dz^2} + \frac{d\ln\sigma_D}{dz}\frac{d\Phi_k}{dz} - k^2\frac{\sigma_P}{\sigma_D}\Phi_k = 0 \tag{3.1}$$

where σ_D and σ_P represent the direct and Pedersen conductivities, respectively. The z axis is vertical and direct current exists parallel to the $y-z$ plane forming sheet currents. The ambient magnetic field is assumed to be vertical.

We solve this equation for Φ_k for a given conductivity profile and for different wavelengths. The boundary conditions for the potential are $\Phi_k(z = 0km) = 0$ and $\Phi_k(z = 1000km) = 1$. The vertical profiles for the ionospheric conductivities are taken from the IRI-86 model (*Bilitza*, 1986) from 80 km at intervals of 1 km up to the altitude of 1000 km. An example of conductivity profile calculated from the IRI-86 model is shown in Figure 12(a). It is assumed that both parallel and Pedersen conductivities at the ground are 10^{-13} mho/m, and that the conductivities between 0 km and 80 km are interpolated linearly on logarithmic scale. Figure 12(b) shows the ionospheric potential profile for each spatial scale-length. Figure 12(c) shows an example of the scale-length dependence of the effective height-integrated Pedersen conductivity $\Sigma_{p,eff}$ calculated from the potential profile shown in Figure 12(b).

The IRI-86 model has parameters representing season, time, locations and solar activity. For these parameters we use the values at the times of observation. The electric field along the z axis can be calculated from the potential Φ. From the eq.(8) in *Forget et al.*, *i.e.*,

$$\Sigma_{p,eff} = \frac{1}{E_x(k, z_0)} \int_0^{z_0} \sigma_P(z) E_x(k, z) dz \tag{3.2}$$

we can obtained $\Sigma_{p,eff}$ which depends on the wave number k.

3.2.2 *Observations*

The instrumentations of magnetic field and vector electric field measurements on DE 2 are shown in chapter 2.2.

The dayside ionospheric conductivity is primarily determined by the solar EUV and X ray radiation, while the nightside ionospheric conductivity is mainly dependent on auroral particle precipitation. However, the IRI-86 model does not take the effect of particle precipitation into consideration, and therefore we cannot compare the results calculated from the nightside the IRI-86 model directly with those from observations. However, it is of interest to see how much

difference there is between the observational results and the calculation based on the nightside the IRI-86 model. Thus one nightside pass (pass 19) is examined for this purpose.

Figure 13 presents the satellite orbits from which data are used. The coordinates in this figure are invariant latitude and invariant magnetic local time. Pass 17 may appear to be a night pass. However, this pass took place near the summer solstice and the terminator at the time of this pass is at a more anti-sunward location than the selected portion of this pass; that is, pass 17 is sunlit. The time of pass 12 is March 13, and this pass crossed the terminator. All other passes are sunlit passes.

Figure 14 shows twenty examples of the scale-length dependence of the ratio $\Delta B_z/\mu_0 E_x$. We used the same data as shown in Figure 6, and the number on each curve corresponds to that in Figure 13.

We assume a power law for the magnetic and electric field power spectral densities. Then, given a frequency band (say, for a band pass filter) the wave energy density is largest at the lower limit of the frequency range. In comparing the observational results on the ratio $\Delta B_z/\mu_0 E_x$ (in a frequency band) with the theoretical results (for a fixed frequency) we assume that the ratio at the frequency of maximum wave energy density in the observation (*i.e.*, at the lower frequency limit of the band pass filter) characterizes the ratio for the frequency band, and we compare this observational ratio with the height-integrated effective Pedersen conductivity, $\Sigma_{P,eff}$, calculated with the IRI-86 model for the same frequency.

3.3 RESULTS

Figure 15 shows the scale-length dependence of the difference between the effective height-integrated Pedersen conductivity $\Sigma_{P,eff}$ derived from the IRI-86 model and the ratio of ΔB_z to $\mu_0 E_x$ observed by DE-2. The coordinate axis represents this difference.

We use a high-pass or band-pass filter in order to investigate the scale-length dependence of the difference between the model and observation. Since a band-pass filter has cut-off frequencies at both ends, the difference $\Delta B_z/\mu_0 E_x$ - $\Sigma_{P,eff}$ is plotted at the center of each band. The pass numbers marked an each curve correspond to those in Figures 13 and 14. For each pass (*i.e.*, for each curve in Figure 15) the difference between the Alfvén conductivity Σ_A $(= 1/(\mu_0 V_A))$ and $\Sigma_{P,eff}$ is calculated from the observed plasma density and magnetic field data (assuming that O^+ ions dominate). This difference is plotted at the extreme left on the vertical axis and connected by a dotted line to the rest of the data for the pass. Points for which the correlation between the magnetic and electric field perturbations is poor are connected by dotted lines (*e.g.*, for the large scale-length portion of curve 4)

Many of the curves in Figure 15 are flat for all scale lengths. But some curves (*e.g.*, curves 6 and 20) show is a significant increase with decreasing scale length towards the shortest scale length. Curve 11 has a minimum at a middle scale length (*i.e.*, at the pass band 0.5-1.0 s). For this pass the difference between the maximum and the minimum of $\Delta B_z/\mu_0 E_x$ - $\Sigma_{P,eff}$ is about 4.0 S.

Curve 19 has a different character because this pass is entirely in darkness. The observational ratios are much larger than the theoretical values for this pass. The difference increases with increasing spatial/temporal scale length, and goes off scale at 2 - 4 s.

In all cases in Figure 15, the values of Σ_A - $\Sigma_{P,eff}$ are smaller than the values of $\Delta B_z/\mu_0 E_x$ - $\Sigma_{P,eff}$ at the smallest scale length plotted, or what amounts to the same thing, the values of Σ_A are smaller than the values of $\Delta B_z/\mu_0 E_x$ at the smallest scale length in Figure 14. In some cases, the value of Σ_A - $\Sigma_{P,eff}$ is nearly equal to the minimum in these curves (*e.g.*, curves 7 and 11).

It is of interest to investigate the magnitude of the difference between the observational

$\Delta B_z/\mu_0 E_x$ and the theoretical $\Sigma_{P,eff}$ relative to the magnitude of the former. Figure 16 shows the scale-length dependence of this relative difference. The format of Figure 16 is similar to that of Figure 15 except that the ordinate is a normalized dimensionless quantity.

Some of the profiles of these curves are different from the corresponding profiles in Figure 15. Curve 19 has a constant value of approximately 1.0. Many of the other curves of others are confined to the level of about ± 0.5. However, parts of curves 6,7 and 12 are below -0.5. In these cases the ratio $\Delta B_z/\mu_0 E_x$ becomes smaller than one half of $\Sigma_{P,eff}$ calculated from the IRI-86 model.

We investigated the relation between the AE index and the scale-length dependence of the difference $\Delta B_z/\mu_0 E_x$ - $\Sigma_{P,eff}$. However, no clear relationships have thus far been found.

3.4 DISCUSSIONS

In Figure 15 we showed the scale-length dependence of the difference between the ratio $\Delta B_z/\mu_0 E_x$ calculated from DE-2 observations and $\Sigma_{P,eff}$ calculated from the IRI-86 model using the method of *Forget et al.*[1991]. If the curves in Figure 15 are all at zero, this means that $\Delta B_z/\mu_0 E_x$ - $\Sigma_{P,eff}$ on each pass is explained by the model of *Forget et al.* For example, curves 2,3 and 5 are near zero for all scale lengths and can be explained by the static model. Some of other curves in Figure 15 remain near some non-zero constant values.

Curve 19 has a quite different profile from the others. The reason for this is as follows: There are two main origins in the ionization of the ionosphere; there are solar EUV and X radiation and auroral particle precipitation. On the nightside, the auroral particle precipitation effect becomes dominant. However, the IRI-86 model takes only the solar radiation effect into consideration. Therefore, the calculated $\Sigma_{P,eff}$ from the model gives an underestimate.

In Figure 16, curve 19 keeps its level near 1.0 through all scale-lengths. Because $\Sigma_{P,eff}$ is

much smaller than $\Delta B_z/\mu_0 E_x$ for this case, the ratio $(\Delta B_z/\mu_0 E_x - \Sigma_{P,eff})/(\Delta B_z/\mu_0 E_x)$ is nearly 1.0. For some other passes the difference between the ratio $\Delta B_z/\mu_0 E_x$ and $\Sigma_{P,eff}$ has a scale-length dependence. We can think of two reasons for this behavior. One is the influence of auroral particle precipitation, as in curve 19, and the other is the existence of Alfvén waves. In the former case, the ratio $\Delta B_z/\mu_0 E_x$ increases by auroral particle precipitation because the ionospheric conductivity increases. In the latter case, the existence of Alfvén waves reduces the ratio, $\Delta B_z/\mu_0 E_x$, because Alfvén conductivity Σ_A is generally lower than Σ_P.

In many cases which show scale-length dependence, the minimum is between 0.25 and 1.0 s in the cut off period, and these minimums are nearly equal to $\Sigma_A - \Sigma_{P,eff}$. It appears reasonable to interpret that these minimums reflect the effect of Alfvén waves. We thus speculate that Alfvén waves exist on the temporal scale of 0.25 - 1.0 s, or, 1 - 4 Hz. In this respect, there have been reports on the existence of Pc 1 - 2 magnetic pulsations in the equatorial magnetosphere at $L > 7$ (e.g., *Anderson et al.*,1992).

3.5 CONCLUSIONS

We compared the ratio, $\Delta B_z/\mu_0 E_x$, between the orthogonal magnetic and electric field perturbations in the auroral ionospheric region and the effective Pedersen conductivity calculated with the method of *Forget et al.* for various scale lengths. Results can be summarized as follows.

1) The differences between the ratio $\Delta B_z/\mu_0 E_x$ from observation and the $\Sigma_{P,eff}$ from model calculation in more than 10 of the 20 cases examined have little dependence on scale length. For these cases, therefore, the scale-length dependence of the ratio $\Delta B_z/\mu_0 E_x$ can be explained by the model of *Forget et al.*

2) Several cases show a minimum in the difference between $\Delta B_z/\mu_0 E_x$ and $\Sigma_{P,eff}$ at 0.25

- 1.0 s. We believe that the primary cause for this scale-length dependence is the presence of Alfvén waves.

3) On the nightside, there is a large difference between the observational ratio and the $\Sigma_{P,eff}$ based on the model, which we interpret as being an effect of auroral particle precipitation.

Chapter 4

Quantitative Relationship Between the Auroral Luminosity and the Ionospheric Conductivity in the Polar Region

4.1 INTRODUCTION

The distribution of the ionospheric conductance (height integrated conductivity) is a controlling factor in the ionosphere-magnetosphere interaction. However, it is difficult to obtain observationally a "snapshot" of the two-dimensional conductance distribution. Over the past two decades many attempts have been made to construct conductance models from data obtained by incoherent scatter radars in the polar regions [Mehta,1979; Senior,1980; Vickrey et al.,1981; de la Beaujardiere et al.,1982; Robinson and Vondrak,1984; Schlegel,1988; Rasmussen et al.,1988; Brekke and Hall,1988; and Senior,1991]. However, the polar radars do not operate for long enough periods to obtain a full two-dimensional distribution of the conductivities. In addition, radar observations are limited in latitude. Wallis and Budzinski[1981] and Spiro et al.[1982] showed statistical results on the two-dimensional distribution of conductance deduced from particle data obtained by polar orbiting satellites. Fuller-Rowell and Evans[1987] have investigated ionospheric Pedersen and Hall conductivities inferred from the particle influx obtained by TIROS-NOAA satellite observations.

Several studies attempted to deduce a "snap-shot" of the ionospheric conductance distribution from auroral luminosity obtained by photometers on board polar orbiting satellites. Craven

et al.[1984] showed the relationship between ionospheric conductance and auroral luminosity on a global scale, where the conductance was estimated from data obtained by ground-based magnetometers. Kamide et al.[1986] also calculated the ionospheric conductance and compared it with the auroral image obtained by DE 1, introducing the following relationship between the height-integrated Pedersen conductivity Σ_P and VUV (vacuum ultraviolet) auroral luminosity I in kR;

$$\Sigma_P \sim K I^{0.5} \text{mhos} \tag{4.1}$$

where K is a constant. This result was improved in Kamide et al.[1989] by including the electric fields deduced from the ion drifts measured along the DE 2 orbit. Robinson et al.[1989] obtained the following quantitative relationships between the auroral luminosity observed by the DE 1 auroral imaging photometer and the ionospheric conductance estimated from Chatanika radar measurements:

$$\Sigma_P = 3.8(I_{123W})^{0.5} \text{mhos} \tag{4.2}$$

$$\Sigma_H = (1.8\overline{E} - 0.8)(I_{123W})^{0.5} \text{mhos} \tag{4.3}$$

where I_{123W} represents auroral luminosity in kilorayleighs obtained by the auroral imaging photometer with 123 nm pass-band filter (Frank et al.,1981), and where $\overline{E}$ represents the average energy of precipitating particles in keV. From this empirical relation, they concluded that the relation between the auroral luminosity and the height-integrated Pedersen conductivity is not sensitive to the energy of precipitating particles, while the relation between the luminosity and the height-integrated Hall conductivity is very sensitive to the particle energy.

Some researchers have attempted to deduce the ionospheric conductances from multispectral auroral images. Eather and Mende [1971], and Rees and Luckey [1974] deduced energies of precipitating electrons using ground-based multispectral auroral image data. Rees et al.[1988],

Lummerzheim et al.[1991] and Rees[1992] applied this method to construct maps of auroral energetic electron parameters from the DE 1 multispectral auroral images.

In this study, we investigate the quantitative relationship between the auroral luminosity observed by DE 1 [Frank et al.,1981] and the height-integrated Pedersen conductivity deduced from the ratio between the east-west component of the magnetic perturbations (ΔB_z) and the north-south component of the electric field (E_x) obtained by DE 2. The new point of this study is that the height-integrated Pedersen conductivity, Σ_P, is deduced not from the precipitating particle data but the magnetic and electric field perturbation data. Since the DE 1 and 2 satellites are in the same meridian plane, there are many cases where DE 1 and 2 are favorably situated to observe simultaneously the same aurora without problems of angle in field of view. In addition, these satellites can observe auroras at various latitudes, while a ground-based radar can observe the electron density distribution only near the radar site.

Numerous attempts have been made to clarify the electrodynamics in the field-aligned current region from the magnetic and electric field perturbations obtained by polar orbiting satellites [Sugiura,1984; Sugiura et al.,1982,1983; Gurnett et al.,1984; Weimer et al.,1985,1987; Israelevich et al.,1988; Berthelier et al.,1989; Dubinin et al,1990; Knudsen et al.,1990,1992; Lysak,1991; Matsuoka et al.,1991; Forget et al.,1991; and Ishii et al.,1992]. From these studies, it was found that the correlation between the orthogonal components of the magnetic and electric field perturbations is generally high in the field-aligned current region, and the ratio $\Delta B/\Delta E$ has a scale (or frequency) dependence. These results were interpreted by two different models: (1) static structures of small-scale field-aligned currents and (2) Alfvén waves. Ishii et al.[1992] showed that the large scale (> 8.0 s or 64 km) magnetic and electric field perturbations observed by DE 2 can generally be interpreted as static structures. In these cases the ratio $\Delta B_z/\mu_0 E_x$ represents the height-integrated Pedersen conductivity, Σ_P.

In that follows we show some case studies and statistical results on the quantitative relationship between the auroral luminosity and Σ_P.

4.2 TECHNIQUE

The Dynamics Explorer (DE) satellites were launched on August 3, 1981, into coplanar polar orbits. The initial apogee and perigee altitudes of DE 1 were 24,875 km and 675 km, and those of DE 2, 1003 km and 299 km, respectively.

Auroral image data were obtained by the spin-scan auroral imaging instrumentation (SAI) on DE 1 [Frank et al.,1981]. Each image frame was assembled from a two-dimensional array of picture elements (pixels) obtained by 120 rotations of the satellite. For the satellite's 6 s spin period, 120 scan lines of an image were obtained in 12 min. The spin axis was oriented normal to the orbital plane with individual scan lines in each image aligned parallel to the orbital plane. The angular dimension of each pixel was $\sim 0.29°$, for a linear dimension of ~ 32 km per Earth radius of altitude.

The imaging instrumentation on DE 1 comprised three distinct photometers and a variety of visible and vacuum ultraviolet (VUV) filters. In this study, we use the data obtained with the VUV photometer and filter 123W, which means that the $\sim$ 30-nm wide pass-band of filter extended to a short-wavelength cutoff at $\sim$ 123-nm. Photometer response to the aurora was dominated by emission from OI (130.4, 135.6-nm) and the LBH bands of N_2, and allowed global imaging of the auroral oval in both the dark and sunlit ionosphere (Frank et al.,1981).

The instrumentations of the magnetic and electric field data on DE 2 are shown in Chapter 2. From the results of Chapter 2, the ratio of the magnetic and electric field perturbations, $\Delta B_z / \mu_0 E_x$, represents the height-integrated Pedersen conductivity, Σ_P, for large scale sizes (typically in 8 to 32 s periods or 64 to 256 km in spatial scale). We calculate the "dynamic" correlation

(see Ishii et al.[1992]) to investigate the variation of the ratio, $\Delta B_z/\mu_0 E_x$, along the orbit of the spacecraft. To reduce the influences of high-frequency perturbation where the Alfvén wave component would be large, and also to reduce the variations in the magnetic field data caused by inaccuracies in the spacecraft attitude data, a high-pass filter with a 20-s cutoff period is used for both half-second average magnetic and electric field data. The correlation coefficient between ΔB_z and E_x and the ratio of ΔB_z to E_x are calculated in a sliding "data window" of 10-s. Interpretation of the value $\Delta B_z/\mu_0 E_x$ is difficult when the correlation coefficient is low, and those intervals in which the correlation coefficient is below 0.5 are not included in the analysis except when specifically indicated. The estimation of the Pedersen conductance, Σ_P, by the ratio, $\Delta B_z/\mu_0 E_x$, is only valid in the field-aligned current region where the amplitudes of the magnetic and electric field perturbations are relatively large. Therefore we did not analyze the data when the fluctuation of the magnetic field did not have enough amplitude. We used the data with the standard deviation of ΔB_z greater than $3nT$. In addition to these criteria, we added another threshold on the current structure. That is, we estimated Σ_P only when the current structure can be approximated by infinite current sheets. Unless the fluctuations are caused by sheet currents, it is generally difficult to interpret the ratio, $\Delta B_z/\mu_0 E_x$, as the Pedersen conductance.

Fung and Hoffman [1992] studied the finite geometry effects of the field-aligned currents. In their study, they showed that the relationship of two horizontal components of the magnetic perturbation should be proportional in a "sheetlike" structure, while it is not linear in an "endlike" structure. They concluded that the high correlation between the two horizontal components of the magnetic field is a sufficient condition for making the "infinite" sheet current approximation except for the cases of Alfvén waves. For this reason we omit the intervals where the absolute value of the correlation between the two components (*i.e.*, ΔB_z and ΔB_x) is less

than 0.5 in a data window strictly speaking, this criterion is not applicable to the case in which the satellite crosses the sheet current perpendicularly, because in that case the amplitude of ΔB_x becomes zero. However, there are generally finite perturbation in ΔB_x in the polar region and this problem can be ignored.

We analyzed 32 cases obtained in the period from September 1981 to January 1982. Of these, eleven cases were in the morning sector, one near the midnight sector, and the other 20 in the evening sector. We avoided data which might contain the influences of a reflection of the solar radiation from the earth (near the terminator). Since the DE satellites' orbit plane is inertially fixed, the local time of the orbital plane depends on season. Thus all the data in the morning sector were obtained after November 1981 and the evening data, from September 1981. Therefore, from this data set it is difficult to investigate the influence of season.

Several corrections are necessary to analyze the auroral luminosity when viewing the aurora obliquely because of the van Rhijn effect and/or atmospheric absorption. To minimize these effects and to make the observing conditions as uniform as possible, we use only those data obtained from viewing directly above the aurora or nearly so.

Figure 17 shows a schematic view of the observational geometry. We call the luminosity at pixels along the DE 2 orbit as "center" data, and call "right" and "left" those pixels one scan line to the right and left of the "center", respectively. In this study, we compare the ratio, $\Delta B_z/\mu_0 E_x$, calculated from the DE 2 observations with the average luminosity data for the "center", "right" and "left" obtained by DE 1.

Plates 1 - 3 show examples of auroral images obtained by DE 1 observation with the 123W filter. A magnetic projection of the DE 2 trajectory to auroral altitudes and the universal time along the trajectory are indicated on each plate.

For 24 cases we used the energetic particle data simultaneously obtained by DE 2 in addition

to the magnetic and electric field data and the auroral images. In its basic operating mode, the low altitude plasma instrument (LAPI) provided a 32-point energy spectrum of positive ions and electrons from 5 eV to 32 keV and from 0° to 180° in pitch angle every second [Winningham et al., 1981].

We should be careful about the time differences between observations of DE 1 and 2. If the time difference between them is large, the relation between the auroral luminosity and the Pedersen conductance cannot be investigated because of the temporal and spatial variations in the aurora. The DE 2 satellite takes 4 - 10-min to cross the auroral oval while observing the magnetic and electric field perturbations, while DE 1 takes less than 18 s (*i.e.*, three scans, "right", "center" and "left") to obtain the luminosity data along the DE 2 trajectory. We selected the data so that the observation-time difference is minimized in each case. However, some time difference cannot be avoided (the maximum time difference being 12-min). A discussion of the influence of the observation-time difference in our analysis is given in Section 4.4.

4.3 RESULTS

4.3.1 *Case studies*

Figures 18 - 21 show the results of comparison of the ratio, $\Delta B_z/\mu_0 E_x$, with auroral luminosity for the three cases of Plates 1 through 3. Figures 18 and 19 correspond to the morning- and evening-side events shown by Plate 1, and Figures 20 and 21 correspond to the evening-side events of Plates 2 and 3, respectively.

Panel (a) of each figure shows the magnetic and electric field perturbations obtained from the DE 2 observations, correlation coefficients between ΔB_z and E_x (thick line) and those between ΔB_x and ΔB_z (thin line) for data window of 10-s, and the ratio $\Delta B_z/\mu_0 E_x$. The

horizontal axis of this panel indicates universal time. The ratio $\Delta B_z/\mu_0 E_x$ is plotted only when both the correlation coefficient between ΔB_z and E_x and that between ΔB_z and ΔB_x are higher than 0.5, and when the value of standard deviation of ΔB_z is greater than 3 nT.

The upper four traces of panel (b) of each figure present the auroral luminosity near the trajectory of DE 2. The horizontal axis indicates the invariant latitude. The time shown at upper right of each panel indicates the time when DE 1 scanned the "center" which is along the trajectory of DE 2. The bottom two traces show the ratio $\Delta B_z/\mu_0 E_x$ and the coefficient of correlation between ΔB_z and E_x. The ratios are shown by asterisks, and their averages within each luminosity pixel are shown as bar chart. A vertical broken line in Panel (b) represents the boundary between the region 1 and 2 field-aligned current systems deduced from magnetic field perturbations. Panel (c) in Figures 18-20 presents the correlation between the auroral luminosity and $\Delta B_z/\mu_0 E_x$ on a log-scale. Solid and open circles represent data obtained in regions 1 and 2, respectively. Each solid or open circle represents the I_{123W}-Σ_P relation in one pixel. The error bars of luminosity indicate the standard deviation of three values of luminosity along the DE 2 orbit, "center","right" and "left". The error bars for ratio $\Delta B_z/\mu_0 E_x$ show the standard deviation of the ratio $\Delta B_z/\mu_0 E_x$ from the average over each pixel. Two thin and thick solid lines present the regression lines of the data obtained in regions 1 and 2, respectively, and a dotted line shows the relationship obtained by Robinson et al.[1989].

For these examples, the characteristics of the precipitating particles are also investigated (Plates 4- 6). The upper panel of each plate gives the variations in the number flux of high energy (>35 keV) electrons with pitch angle 0° (blue line) and 90° (yellow line) observed by Geiger-Mueller tube assemblies (GMT). The number flux is given in units of particles/cm^2-s-sr. The middle and lower panels show the energy fluxes for ions and electrons averaged over all pitch angles observed between 0° and 90°, respectively.

Case 1: Nov. 25, 1981

Plate 1 and Figure 18 show an example on the morning sector observed at 03:25UT (DE 1) and 03:26:00-03:33:00UT (DE 2) on November 25, 1981. This is about one hour after the abrupt onset of a brief auroral substorm (maximum AE $\sim$ 750 nT), and well into the recovery phase. The hourly value of the AE index was 160 nT. The time difference between the DE 2 observations of the magnetic and electric fields and the DE 1 auroral imaging along the DE 2 orbit plane was 1 min at the low latitude end and 8 min at the high latitude end of the oval. Σ_P was not calculated for the period 03:29:00-03:29:30 UT because of the criteria mentioned above (*see* Figure 18(a)).

Differences between the profiles for auroral luminosity and $\Delta B_z/\mu_0 E_x$ are clearly seen (Figure 18(b)). Neither the "center" nor the "average" luminosity profile has a clear peak, while the profile of $\Delta B_z/\mu_0 E_x$ has a distinct peak at 70° invariant latitude.

Figure 18(c) shows a scatter plot between $\Delta B_z/\mu_0 E_x$ and auroral luminosity, with different symbols used to distinguish between measurements made in the region 1 and 2 current systems. The boundary between these two regions was crossed at 03:29:30 UT; this boundary coincides with the boundary between the central plasma sheet (CPS) and the boundary plasma sheet (BPS) regions in this case. Open and solid circles in Fig. 18(c) present data obtained at lower and higher latitudes than this boundary at 74.9° invariant latitude, respectively. The open and solid circles are divided into two nearly parallel clusters. The coefficients of correlation between luminosity and $\Delta B_z/\mu_0 E_x$ for the data points in regions 1 and 2 are 0.788 and 0.510, respectively.

We also investigated the dependence of the relation between auroral luminosity and $\Delta B_z/\mu_0 E_x$ on the energy of precipitating electrons. To investigate this energy dependence we calculate the characteristic energy E_0 ($= (1/2)\int Ef(E)dE/\int f(E)dE$ where $f(E)$ is the differential

downward electron flux). To reduce the influence of photoelectrons, E_0 is calculated only for particle energies greater than 20 eV. The average of characteristic energies of precipitating electrons is 1484 eV in CPS, and 173 eV in BPS, respectively.

A characteristic property of this case is the existence of large ion flux (03:29:00-03:29:30UT). Correlations between ΔB_z and E_x and between ΔB_x and ΔB_z both become poor in this region.

Figure 19 presents observations on the evening side during the same orbit as that for Figure 18. The differences between the time of observation of the magnetic and electric field perturbations and that of auroral luminosities are 4 min at the poleward side and −3 min at the equatorward side of the auroral oval. In this case, profiles of the auroral luminosity and $\Delta B_z/\mu_0 E_x$ are similar to each other (Fig. 19(b)). The peak in the auroral luminosity nearly corresponds to that of $\Delta B_z/\mu_0 E_x$ (invariant latitude $\sim 73°$). The boundary between the region 1 and 2 current systems is at 73.5° INV (invariant latitude). It is noticed that the precipitating particles on the evening side have lower energies than those on the morning side as seen in Plate 4, and that it is difficult to determine unambiguously the boundary between BPS and CPS in this case, but this boundary may be placed at 03:37:10 UT the same as the boundary between regions 1 and 2. The average of characteristic energies of precipitating electrons is 290 eV in BPS, and 625 eV in CPS. The correlation coefficient between $\Delta B_z/\mu_0 E_x$ and auroral luminosity is 0.948 in region 1, and 0.934 in region 2 (Fig. 19(c)). The data at lower latitudes (high energy electron region) show lower luminosity for the same conductance than those at higher latitudes (low energy electron region). This result agrees well with that of Robinson et al.[1988], who analyzed data from the same local-time sector as in the present case.

Case 2: Nov. 21, 1981

Plate 2 and Figure 20 show another case of simultaneous observations of auroral luminosity and magnetic and electric fields. These data were obtained in the evening sector at 12:30:00 -

12:34:00 UT (DE 2) and at 12:30 UT (DE 1) on November 21, 1981. In this case, the difference between the times of observation of DE 2 and 1 is nearly zero at the poleward edge of the auroral oval and is 4 min at the equatorward edge of the auroral oval. Geomagnetic activity was decreasing in the recovery phase of a substorm which was followed by another substorm in close succession (hourly value of AE=364 nT).

From Figure 20(b), it is seen that the correlation between ΔB_z and E_x is rather poor in the region where the auroral luminosity is very high (*i.e.*, 71° <INV<73°). Plate 2 shows that the surge head is at the poleward boundary of the aurora. The peak of $\Delta B_z/\mu_0 E_x$ is at about 66.0° INV, while there is no significant enhancement in auroral luminosity.

In this case, the boundary between the region 1 and 2 current systems corresponds to the boundary between the BPS and CPS (at about 12:30:30 UT, 70.7° INV in Plate 5). Figure 20(c) shows a scatter plot between luminosity and $\Delta B_z/\mu_0 E_x$ for the two latitude groups divided by this boundary; their regression lines are almost parallel. The average of characteristic energies of precipitating particles is 1690 eV in BPS, and 2293 eV in CPS. As in the previous examples, data obtained at lower latitudes (high energy electron region) tend to have lower luminosity or higher conductance than those obtained at higher latitudes (low energy electron region).

Case 3: Oct. 20, 1981

Plate 3 and Figure 21 show another case in which the auroral luminosity and the magnetic and electric fields were observed almost simultaneously. This example was obtained in the evening sector at 19:18:00-19:23:00 UT (DE 2) and at 19:14 UT (DE 1) on October 20, 1981. Magnetic activity during this period is very high (hourly value of AE index = 735 nT) compared with the previous examples. The difference in time of observations of DE 2 and 1 is 4 min at the poleward edge and 11 min at the equatorward edge of the auroral oval. The equatorward edge of the auroral oval near midnight was around 55° INV in this case, which is unusually low.

Figure 21(a) shows that the z-component of the magnetic field perturbation has large scale structures, while the electric field oscillates without large scale structures. Such a tendency is generally seen during disturbed periods on the night side. This large difference between the two field profiles makes the correlation between ΔB_z and E_x poorer during disturbed periods than that during quiet periods. It should be noted that the invariant latitude dependence of the relation between auroral luminosity and $\Delta B_z/\mu_0 E_x$ is opposite from the results in Cases 1 and 2. The data obtained at lower latitudes have higher luminosity or lower conductance than those obtained at higher latitudes. The average of characteristic energies of precipitating electrons is 1172 eV in BPS, which is higher than that in CPS (162 eV). Thus the energy dependence is consistent with the previous cases in which the region of lower energy electrons shows higher luminosity and lower conductance than the region of higher energy electrons.

4.3.2 *Statistical results*

We analyzed 32 cases in all and were able to compare these results with particle data for 24 of the cases. It was found that the relation between auroral luminosity and $\Delta B_z/\mu_0 E_x$ is dependent on invariant latitude and/or energy of precipitating particles. In this section, statistical results are presented for the dependence of the $I_{1231\text{Å}}$-Σ_P relation on invariant latitude and energy. In addition to these analyses, the importance of the time difference between observations with DE 1 (auroral luminosity) and 2 (magnetic and electric field perturbations) is examined.

Figure 22 shows scatter plots for the entire data set classified by the time difference between measurements of auroral luminosity and the magnetic and electric fields. The format of the scatter plot is the same as that of panel (c) of Figures 18 - 21. In Figure 22(a), the data points are widely scattered and any relation between the auroral luminosity and $\Delta B_z/\mu_0 E_x$ is difficult to discern. Figures 22(b) and (c) show results sorted by the time difference; observations with

time difference less than and more than 30-s are plotted in Figure 22(b) and (c), respectively. The result shows that the selection of cases with smaller time differences does not improve the correlation.

We also analyzed these data for ranges of the AE index, but no significant dependence was found.

Next, we analyzed these data as functions of invariant latitude and local time. As the data points near midnight are few, we divided the data into two groups: data obtained in the morning sector and those in the evening sector. For the division by invariant latitude, the boundary between the region 1 and 2 current systems is used. While the results shown in Figure 23 are complicated, we see a tendency that in both local time sectors, the higher latitude group tends to have smaller values of $\Delta B_z/\mu_0 E_x$ than the lower latitude group for the same luminosity. This tendency is clearer on the morning side than that on the evening side.

Another noticeable point in this figure is the local time dependence of the relation at the lower latitudes. On the evening side, the correlation coefficient is relatively higher (0.580) than that on the morning side (0.138), and the distribution of points is consistent with the results of Robinson et al.[1989]. The distribution on the morning side is almost random.

Figure 24 shows the results of comparison of the relation between auroral luminosity and $\Delta B_z/\mu_0 E_x$ with energies of precipitating electrons in 24 cases. The dotted line in each panel shows the result of Robinson et al.[1989] for comparison, and the broken lines in panel (b), (c) and (d) of Figure 24 represent the model by Rees et al.[1988], which will be discussed in the next section. Two solid lines represent regression lines for our data set. Figure 24(a) shows the distribution of points with characteristic energy less than 100 eV. Figures 24(b), (c) and (d) represent plots for characteristic energies of 100-500 eV, 500 eV-1 keV and greater than 1 keV, respectively. In using the Rees model, we adopted the characteristic energies of 250 eV (b), 750

eV (c), and 1 keV (d). Points scatter in the same way as in Figure 23, but the center of scatter shifts towards higher conductance (towards right in these plots) with increasing particle energy. The results of Robinson et al.[1989] have the best agreement with the relation for higher energy particles (*i.e.*, Figure 24(d)), while the model of Rees et al.[1988] appears to agree better with the cases of lower energies (*i.e.*, Figure 24(b)).

4.4 DISCUSSION

One of the new findings in this study is the invariant latitude dependence of the I_{123W}-Σ_P relation. In most cases, Σ_P decreases with increasing invariant latitude for the same luminosity. However, in some cases, this relation is reversed (*e.g.*, Figure 21(b) and (c)). According to Kamide et al.[1986], the relation between I_{123W} and Σ_P can be expressed as equation (4.1). Our results suggest that the proportionality coefficient K has an invariant latitude dependence.

Rees et al.[1988] estimated the DE 1 UV imager response (in counts/pixel) due to the auroral luminosity for an electron energy flux of 1 erg·cm^{-2}·s^{-1} as a function of the characteristic energy of an assumed Maxwellian distribution. They also calculated the Hall and Pedersen conductances as functions of characteristic energy and electron energy flux. They noted the following points. (1) The auroral luminosity as given in DE 1 counts per unit energy flux ε obtained with the 123W filter decreases monotonically with increasing characteristic energy of precipitating electrons. This decrease in the emissions is due to increasing absorption by O_2 above the region of auroral emission. (2) The ratio $\Sigma_P/\varepsilon^{0.4}$ has a peak at a characteristic energy of about 2 keV, because the Pedersen mobility reaches a maximum at an altitude of about 140 km. Robinson et al.[1989] explained why the I_{123W}-Σ_P relation is insensitive to the characteristic energy of precipitating electrons by pointing out that both luminosity and Σ_P decrease with increasing electron energy when the characteristic energy is greater than 2

keV. It follows that the relation between the luminosity and Pedersen conductance will be sensitive to the characteristic energy of precipitating electrons when it is less than 2 keV; in this energy range, Σ_P increases while luminosity decreases with increasing characteristic energy. This explanation is consistent with our results shown in the previous section ,*e.g.*, the cases included in Figure 21 and the statistical result presented in Figure 24.

The result calculated from the Rees et al.[1988] model (broken lines in Figure 24(b), (c) and (d)) is close to one of the regression lines when the characteristic energy of precipitating electrons is 100-500 eV (Figure 24(b)). In Figure 24(c) and (d), the result from Rees et al.[1988] overestimates Σ_P in the I_{123W}-Σ_P relation of our results, and the empirical relation of Robinson et al.[1989] is closer to our results. The discrepancy of our result with that of Rees et al.[1988] at high energy may be explained by taking into account the scattering of 130.4-nm emissions. As mentioned in Robinson et al.[1989], the 130.4-nm lines of atomic oxygen suffer multiple scattering and self-absorption, and if these emissions are the dominant contributors to the detector response with the 123W filter, the model calculation must be different from the observed values in the I_{123W}-Σ_P relation. In addition, the 123W filter for the DE 1 VUV imager provides images of primarily optically thick OI emissions at 130.4 nm. Thus the relationship between the total column emission and the characteristic electron energy is not straightforward. Their model calculation without 130.4-nm shows the tendency that the observed I_{123W} is greater than the model at the same Σ_P, and this is consistent with our results.

Robinson et al.[1989] estimated the ionospheric conductance from data obtained by the Chatanika radar. These observations covered from 62° to 69° of invariant latitude, and four of the six cases they used in their study were taken from the observation on the evening side (other two cases were obtained near midnight and from the early morning sector). Therefore it is reasonable that their result agrees well with our result for the lower latitude of evening side

(*i.e.*, Figures 19(c) and 23(c)).

The local time dependence of the relation between the auroral luminosity and ionospheric conductance might be explained as follow: According to the characteristics of auroral display obtained by Akasofu[1981], diffuse auroras in the evening sector have smooth displays, on the other hand, those in the morning sector have complex shapes. It is speculated that the precipitating electrons of diffuse auroras in the morning sector have various energies and therefore the relation between luminosity and conductance is complicated in the morning sector.

Even if the energy dependence of the I_{123W}-Σ_P relation is taken into account, this relationship is still too complicated to be described with a simple formula. Possible sources of this complexity in the I_{123W}-Σ_P relation other than the invariant latitude and energy of the precipitating electrons are: (1) time differences between observations at DE 1 and 2, (2) the decay constant for ionospheric conductivity, and (3) the spatial resolution of auroral observations.

As to the first possibility, the distribution of the points for observations within 30-s of time difference (Figure 22(b)) does not necessarily show a smaller scatter than for points for observations more than 30 s apart (Figure 22(c)). Even for the group of smaller time differences, there is a significant scatter in the distribution. The error due to the difference between the times for luminosity and Σ_P may be related to the phase of magnetic activity, because the temporal and spatial variations are higher under disturbed conditions. Therefore the time difference in observation could be one of the causes for the scatter. We have shown an example for which a clear difference exists in the profiles of auroral luminosity and conductance while there was no time difference (*e.g.*,Figure 20(b)). In addition, Figure 22 shows that the I_{123W}-Σ_P relation is almost independent of difference in time of observation. Therefore, we conclude that the time difference is not likely to be the main cause for the observed invariant latitude dependence in the I_{123W}-Σ_P relation.

To examine the second possibility, we need to know the lifetime of electrons in the E-region and the lower F-region. Jones and Rees [1973] calculated the decay of electron density following the cessation of ionization. It was shown that the electron density decreases from 10^6 to 10^3 cm^{-3} at 100 km altitude within 60-s after cessation of ionization, while it decreases from 2×10^5 to 10^5 at 200 km altitude within 600-s. If the ionospheric conductivity is estimated from the electron density near 120 km altitude, the time constant of the conductance is estimated to be about 60-s. The effect of the time history of auroral activity on the conductivities would be of the same order of magnitude as the effect of 60-s of observation-time difference between DE 1 and 2. Especially, one reason why the I_{123W}-Σ_P relation is complicated in the lowest energy of precipitating electrons (Figure 24(a)) is speculated that the background Σ_P varies significantly by time constant of ionizations.

For discussions on the third possibility, error bars are indicated in panels (c) of Figures 18-21. The length of the error bars for measurements of luminosity is a measure of the difference in luminosity at the "right", "center", and "left" pixels, while the error bars of the ratio $\Delta B_z/\mu_0 E_x$ denote the standard deviation of the ratio within a region defined by a pixel of the auroral image. When the standard deviation of $\Delta B_z/\mu_0 E_x$ is large as is indicated for some points in panels (c) of Figures. 18-21, it is deduced that the aurora has fine structures with scale length less than one pixel ($\sim$ 32 km of spatial scale per earth radius of altitude), and this possibility can be a cause of the complication in the relation between luminosity and conductance.

Possible artificial causes of the invariant latitude dependence of the I_{123W}-Σ_P relation shown in (b) of Figures 18, 20 and 21 are: (1) an error in the mapping of the DE 2 orbit on the auroral altitude, and (2) the relatively large field of view of the imager (*i.e.*, spatial resolution). The former possibility can be divided into two different subjects: (1a) differences between the model magnetic field of the earth and the actual field during a substorm, and (1b) the

difference between the assumed height of auroral emissions and the actual height. However, these possibilities are quantitatively not enough to explain the invariant latitude dependence of the I_{123W}-Σ_P relation. For example, there is a difference of about 4° of invariant latitude between the peak of auroral luminosity and the peak of $\Delta B_z/\mu_0 E_x$ in Fig. 18(b). If this difference arises from an inaccurate mapping by the geomagnetic field model (*i.e.*, possibility (1a)), the disturbance in the horizontal component of magnetic field near the DE 2 spacecraft must be about 30000 nT (earth's main field) $\times \tan 4° \sim 3000nT$, but such a possibility is unlikely. About possibility (1b), in plotting panel (b) in Figures 18-21 we varied the assumed heights of the aurora from 100 to 300 km; but no significant difference was found in the location of the peak in auroral luminosity.

We discuss the possibility (2) as follows. Equation (1) shows that the relationship between Σ_P and I_{123W} is not linear. On the other hand, the luminosity and the conductance are averaged linearly in a pixel. For example, if half the area of a pixel is occupied with an aurora whose luminosity is uniform, the measured luminosity and the estimated conductance at this pixel will also be one half of the value it would be if all the area of the pixel is occupied with an aurora of the same luminosity. However, the conductance inferred from this luminosity is $1/\sqrt{2}$ times that for the case in which the whole area of the pixel is occupied by aurora. The results is that the actual conductance averaged over the pixel is lower than that estimated from the luminosity. Thus we overestimate the conductance in the case when the aurora is non-uniform in a pixel. Robinson et al.[1989] also mentioned that there are some points which have higher luminosity and lower conductance at high latitudes than at low latitudes, and they explained this by the resolution of the imager. The large error bar for Σ_P suggests the existence of a non-uniformity in the aurora distribution, and this effect must be taken into account. However, the spatial non-uniformity cannot explain the energy dependence shown in Figure 24, unless it

is proved that an aurora produced by higher energy electrons has smaller structures than an aurora produced by lower energy electrons.

We conclude that the invariant latitude dependence of the relation between auroral luminosity and conductance is due to the different energies of the precipitating electrons.

It is shown that the correlation between the magnetic and electric field perturbations is poor in a region where the auroral luminosity is very high (*i.e.*,Figure 20(b)). We speculate that this poor correlation comes from a strong temporal and spatial variations of luminosity and conductance associated with such regions as the westward traveling surge.

4.5 CONCLUSIONS

We have investigated the quantitative relationship between the auroral luminosity obtained by the DE 1 imaging photometer at VUV wavelengths and the height-integrated Pedersen conductivity, Σ_P, deduced from magnetic and electric field perturbations observed by DE 2. We obtained the following results:

1. The relation between the auroral luminosity and the ionospheric conductivity has a latitude dependence. In most cases, for the same luminosity, Σ_P decreases with increasing invariant latitude. However, this tendency is reversed in some cases. This latitude dependence of the luminosity-Σ_P relation can be explained by the difference in energy of the precipitating electrons. That is, Σ_P decreases with decreasing energy of auroral particles for the same luminosity.

2. In the region of lower energy electrons, our result is consistent with the model results calculated by Rees et al.[1988]. On the other hand, in the region of higher energies, our result is consistent with the result of Robinson et al.[1989] and not with the model of Rees et al.[1988]. We speculate that the discrepancy between the Rees model and our result is due to the influence

of the 130.4-nm emissions of atomic oxygen.

3. There is a clear difference in the relationship between the results on the morning side and those on the evening side. In the equatorward part of the auroral oval on the evening side, the results are similar to those of Robinson et al.[1989]. In contrast, for the equatorward part of the auroral oval on the morning side, the correlation between the auroral luminosity and conductivity is rather poor. It is speculated that the reason for the poor I_{1231}-Σ_P correlation is that the precipitating electrons on the morning side have wider variations in energy than on the evening side.

4. The correlation between the magnetic and electric fields becomes poor in strong auroral luminosity regions.

Acknowledgments. We wish to thank N.C.Maynard for permitting us to use his electric field data in this paper.

We would like to thank Rae Dvorsky and Richard Dyson of the University of Iowa for compiling the auroral imaging data used for this study.

We gratefully acknowledge helpful discussions with T.Araki, B.-H. Ahn, R.Fujii, T. Kamei, E.Kaneda, S.Machida, T.Ono, D.R.K.Rao and M.Takeda.

This study has been supported in part by grant 60420013 under the Monbusho Scientific Research Program and by grant 63044070 and 03044128 under the Monbusho International Scientific Research Program, the Ministry of Education, Japan. The work of M. Ishii is supported by the fellowships of the Japan Society for the Promotion of Science for Japanese Junior Scientists. The work at Southwest Research Institute was supported by NASA Contract NAS5-33031.

REFERENCES

Akasofu, S.-I., Auroral arcs and auroral potential structure, in *Physics of Auroral Arc Formation, Geophys. Monogr. Ser.*, vol. 25, edited by S. -I. Akasofu and R. Kan, 1, AGU, Washington D.C., 1981.

Anderson, B.J., R.E.Erlandsom and L.J.Zanetti, A statistical study of Pc 1-2 magnetic pulsations in the equatorial magnetosphere 1. Equatorial occurrence distributions, *J. Geophys. Res.*, *97*, 3075,1992.

de la Beaujardiere, O., M.J.Baron, V.B.Wickwar, C.Senior, and J.V.Evans, MITHRAS: A program of simultaneous radar observations of the high-latitude auroral zone, report, contract F49620-81-C-042, SRI International, Menlo Park, Calif., 1982.

Bertherier,A., J.-C.Cerisier, J.-J. Bertherier, J.-M. Bosqued, and R.A.Kovrazkhin, The electrodynamic signature of short scale field aligned currents, and associated turbulence in the cusp and dayside auroral zone, Electromagnetic Coupling in the Polar Clefts and Caps, ed. by P.E.Sandholt and A.Egeland, Dordrecht, Kluwer Academic Publishers, 299,1989.

Bilitza, D., International reference ionosphere: Recent developments, *Radio Sci.*, *21*, 343, 1986.

Block,L.P., C.-G.Falthammar, P.-A.Lindqvist, G.Marklund, F.S.Mozer, A.Pedersen, T.A.Potemra and L.J.Zanetti, Electric field measurements on VIKING: first results, *Geophys. Res. Lett.*, *14*, 435, 1987.

Brekke, A. and C.Hall, Auroral ionospheric quiet summer time conductances, *Ann. Geophys.*, *6*, 361, 1988.

Burke, W. J., D. A. Hardy, F. J. Rich, M. C. Kelley, M. Smiddy, B. Schuman, R. C. Sagalyn, R. P. Vancour, P. J. L. Widman, and S. T. Lai, Electrodynamic structure of the late evening sector of the auroral zone, *J. Geophys. Res.*, *85*, 1179, 1980.

Craven, J.D., Y.Kamide, L.A.Frank, S.-I.Akasofu, and M.Sugiura, Distribution of aurora and ionospheric currents observed simultaneously on a global scale, in *Magnetospheric Currents, Geophys. Monogr. Ser.* , vol.28, edited by T.A.Potemra, 137, AGU, Washington, D.C., 1983.

Dubinin, E. M., P. L. Israelevich, and N. S. Nikolaeva, Auroral electromagnetic disturbances at an altitude of 900 km: The relationship between the electric and magnetic field variations, *Planet. Space Sci.*, *38*, 97, 1990.

Eather, R.H., and S.B.Mende, Airborne observations of auroral precipitation patterns, *J. Geophys. Res.*, *76*, 1746, 1971.

Farthing, W.H., M. Sugiura, B.G. Ledley, and L.J. Cahill, Jr., Magnetic field observations on DE-A and -B, *Space Sci. Instrum. 5*, 551, 1981.

Forget, B., J.-C. Cerisier, A. Berthelier, and J.-J. Berthelier, Ionospheric closure of small-scale Birkeland currents, *J. Geophys. Res.*, *96*, 1843, 1991.

Frank, L.A., J.D. Craven, K.L. Ackerson, M.R. English, R.H. Eather, and R.L. Carovillano, Global auroral imaging instrumentation for the dynamics explorer mission, *Space Sci. Instrum. 5*, 369, 1981.

Fuller-Rowell, T.J., and D.S.Evans, Height-integrated Pedersen and Hall conductivity patterns inferred from the TIROS-NOAA satellite data, *J. Geophys. Res.*, *92*, 7606, 1987.

Fung, S.A., and R.A. Hoffman, Finite geometry effects of field-aligned currents, *J. Geophys.*

Res., 97, 8569, 1992.

Gurnett, D. A., R. L. Huff, J. D. Menietti, J. L. Burch, J. D. Winningham, and S. D. Shawhan, Correlated low-frequency electric and magnetic noise along the auroral field lines, *J. Geophys. Res., 89*, 8971, 1984.

Iijima,T., and T.A.Potemra, Field-aligned currents in the dayside cusp observed by Triad, *J. Geophys. Res., 81*, 5971, 1976.

Ishii,M., M.Sugiura, T.Iyemori, and J.A.Slavin, Correlation between magnetic and electric fields in the field-aligned current regions deduced from DE-2 observations, *J. Geophys. Res., 97*, 13877, 1992.

Israelevich,P.L., I.M.Podgorny, A.K.kuzmin, N.S.Nikolaeva, and E.M.Dubinin, Convection and field-aligned currents, related to polar cap arcs, during strongly Northward IMF (11 January 1983), *Planet. Space Sci., 36*, 1317, 1988.

Iyemori, T., A statistical study of ULF waves observed by Magsat at ionospheric altitude, *Proc. NIPR Symp. Upper Atmos. Phys., 1*, 146, 1988.

Jones, R.A. and M.H. Rees, Time dependent studies of the aurora– I. Ion density and composition, *Planet. Space Sci., 21*, 537,1973.

Kamide, Y., A.D. Richmond, and S. Matsushita, Estimation of ionospheric electric fields, ionospheric currents, and field-aligned currents from ground magnetic records, *J. Geophys. Res., 86*, 801, 1981.

Kamide, Y., J.D. Craven, L.A. Frank, B.-H. Ahn, and S.-I.Akasofu. Modeling substorm current systems using conductivity distributions inferred from DE auroral images, *J. Geophys. Res., 91*, 11235, 1986.

Kamide, Y., Y. Ishihara, T.L.Killeen, J.D. Craven, L.A. Frank, and R.A. Heelis, Combining electric field and aurora observations from DE 1 and 2 with ground magnetometer records

to estimate ionospheric electromagnetic quantities, *J. Geophys. Res., 94*, 6723, 1989.

Knudsen, D.J., M.C.Kelley, G.D. Earle, J.F. Vickrey, and M. Boehm, Distinguishing Alfvén waves from quasi-static field structures associated with the discrete aurora: sounding rocket and HILAT satellite measurements, *Geophys. Res. Lett., 17*, 921, 1990.

Knudsen, D.J., M.C.Kelley, and J.F.Vickrey, Alfvén waves in the auroral ionosphere: A numerical model compared with measurement, *J. Geophys. Res., 97*, 77, 1992.

Langel, R. A., R. H. Estes, G. D. Mead, E. B. Fabiano, and E.R. Lancaster, Initial geomagnetic field model from MAGSAT vector data, *Geophys. Res. Lett., 7*, 793, 1980.

Lummerzheim, D., M.H. Rees, J.D.Craven, and L.A.Frank, Ionospheric conductances derived form DE-1 auroral images, *J. Atmos. Terr. Phys., 53*, 281, 1991.

Lysak, R.L., Feedback instability of the ionospheric resonant cavity, *J. Geophys. Res., 96*, 1553, 1991.

McDiarmid, I.B., J.R. Burrows, and E.E. Budzinski, Average charecteristics of magnetospheric electrons (150 eV to 200 keV) at 1400 km, *J. Geophys. Res., 80*, 73, 1975.

Matsuoka, A., T. Mukai, H. Hayakawa, Y.-I. Kohno, K. Tsuruda, A. Nishida, T. Okada, N. Kaya, and H. Fukunishi, EXOS-D observations of electric field fluctuations and charged particle precipitation in the polar cusp, *Geophys. Res. Lett., 18*, 305, 1991.

Maynard, N.C., E.A.Bielecki, and H.F. Burdick, Instrumentation for vector electric field measurements from DE-B, *Space Sci. Instrum. 5*, 523, 1981.

McEwen, D.J., and D.A.Bryant, Optical-particle characteristics of pulsating aurora, *J. Atmos. Terr. Phys., 40*, 871, 1978.

Mehta, N. C., Ionospheric electrodynamics and its coupling to the magnetosphere, Ph.D. thesis, Univ. of Calif., San Diego, 1979.

Mende, S.B., R.H.Eather, M.H.Rees, R.R.Vondrak, and R.M.Robinson, Optical mapping of

ionospheric conductance, *J. Geophys. Res., 89*, 1755, 1984.

Rasmussen, C. E., R. W. Schunk, and V. B. Wickwar, A photochemical equilibrium model of ionospheric conductivity, *J. Geophys. Res., 93*, 9831, 1988.

Rees, M.H., Auroral ionization and excitation by incident energetic electrons, *Planet. Space Sci., 11*, 1209, 1963.

Rees, M.H., and D.Lucky, Auroral electron energy derived from ratio of spectroscopic emissions, 1. model computations, *J. Geophys. Res., 79*, 5181, 1974.

Rees, M.H., D.Lummerzheim, R.G.Roble, J.D.Winningham, J.D.Craven, and L.A.Frank, Auroral energy deposition rate, characteristic electron energy, and ionospheric parameters derived from Dynamics Explorer 1 images, *J. Geophys. Res., 93*, 12841, 1988.

Rees, M.H., Auroral energy deposition rate, *Planet. Space Sci., 40*, 299, 1992.

Reid, G. C., Ionospheric effects of electrostatic fields generated in the outer magnetosphere, *J. Res. Natl. Bur. Stand., Sect.D, 69, 6*, 827, 1965.

Rich, F. J., C. A. Cattell, M. C. Kelley, and W. J. Burke, Simultaneous observations of auroral zone electrodynamics by two satellites: Evidence for height variations in the topside ionosphere, *J. Geophys. Res., 86*, 8929, 1981.

Robinson, R. M., and R. R. Vondrak, Electrodynamic properties of the evening sector ionosphere within the region 2 field-aligned current sheet, *J. Geophys. Res., 87*, 731, 1982.

Robinson, R. M., and R. R. Vondrak, Measurements of E region ionization and conductivity produced by solar illumination at high latitudes, *J. Geophys. Res., 89*, 3951, 1984.

Robinson, R.M., R.R.Vondrak, J.D.Craven, L.A.Frank, and K.Miller, A comparison of ionospheric conductances and auroral luminosities observed simultaneously with the Chatanika radar and the DE 1 auroral imagers, *J. Geophys. Res., 94*, 5382, 1989.

Schlegel, K., Auroral zone E-region conductivities during solar minimum derived from EISCAT

data, *Ann. Geophys., 6,* 129, 1988.

Senior, C., Les conductivité ionosphèriques et leur rôle dans la convection magnétosphèrique, Une étude expérimentale et théorique, Diplôme de docteur de 3^e cycle, Univ. Pierre et Marie Curie, Paris, 1980.

Senior, C., Solar and particle contributions to auroral height-integrated conductivities from EISCAT data: A statistical study, *Ann. Geophys., 9,* 449, 1991.

Smiddy, M., W. J. Burke, M. C. Kelley, N. A. Saflekos, M. S. Gussenhoven, D. A. Hardy, and F. J. Rich, Effects of high-latitude conductivity on observed convection electric fields and Birkeland currents, *J. Geophys. Res., 85,* 6811, 1980.

Spiro, R.W., P.H.Reiff, and L.J.Maher,Jr., Precipitating electron energy flux and auroral zone conductances – an empirical model, *J. Geophys. Res., 87,* 8215, 1982.

Sugiura, M., A fundamental magnetosphere-ionosphere coupling mode involving field-aligned currents as deduced from DE-2 observations, *Geophys. Res. Lett., 11,* 877, 1984.

Sugiura, M., N. C. Maynard, W. H. Farthing, J. P. Heppner, B. G. Ledley, and L. J. Cahill, Jr., Initial results on the correlation between the magnetic and electric fields observed from the DE-2 satellite in the field-aligned current regions, *Geophys. Res. Lett., 9,* 985, 1982.

Sugiura, M., T. Iyemori, R. A. Hoffman, and N. C. Maynard, Relationships between field-aligned currents, electric fields, and particle precipitation as observed by Dynamics Explorer-2, in *Magnetospheric Currents, Geophys. Monogr. Ser.,* vol. 28, edited by T. A. Potemra, 96, AGU, Washington, D.C.,1983.

Vickrey, J. F., R. R. Vondrak, and S. J. Mathews, The diurnal and latitudinal variation of auroral zone ionospheric conductivities, *J. Geophys. Res., 86,* 65, 1981.

Vickrey, J. F., R. C. Livingston, N. B. Walker, T. A. Potemra, R. A. Heelis, M. C. Kelley, and F. J. Rich, On the current-voltage relationship of the magnetospheric generator at

intermediate spatial scales, *Geophys. Res. Lett., 13,* 495, 1986.

Wallis, D.D., and E.E.Budzinski, Empirical models of height integrated conductivities, *J. Geophys. Res., 86,* 125, 1981.

Weimer, D. R., C. K. Goertz, D. A. Gurnett, N. C. Maynard, and J. L. Burch, Auroral zone electric fields from DE 1 and 2 at magnetic conjunctions, *J. Geophys. Res., 90,* 7479, 1985.

Weimer, D. R., D. A. Gurnett, C. K. Goertz, J. D. Menietti, J. L. Burch, and M. Sugiura, The current-voltage relationship in auroral current sheets, *J. Geophys. Res., 92,* 187, 1987.

Winningham, J.D., J.L.Burch, N.Eaker, and V.A.Blevins, The low altitude plasma instrument (LAPI), *Space Sci. Instrum. 5,* 465, 1981.

Woolf, H. M., On the computation of solar elevation angles and the determination of sunrise and sunset times, *Rep. 1968-13 X-1646,* NASA Langley Res. Cent., Hampton, Va., 1968.

Figure Captions

Plate 1 Image data obtained by DE 1 satellite with 123W filter at 03:37 UT, November 25, 1981. The scale in plot and number beside it are the trajectory of DE 2 satellite and the universal time of DE 2 passage. The characters "M" and "N" are the magnetic and geographic north pole.

Plate 2 Image data obtained DE 1 satellite with 123W filter at 12:30 UT, November 21, 1981. The format is the same as Plate 1

Plate 3 Image data obtained DE 1 satellite with 123W filter at 19:14 UT, October 20, 1981. The format is the same as Plate 1

Plate 4 The result of particle energy observed simultaneously with the first example.(*i.e.*, Plate 1) Upper panel shows variations of number flux of high energy particle ($E > 35KeV$)

whose pitch angle is over (blue line) and less(yellow line) than 90°. Middle and lower panel show energy flux of ion and electron, respectively.

Plate 5 The result of particle energy observed simultaneously with first example.(*i.e.*, Plate 2) Format is the same as Plate 4.

Plate 6 The result of particle energy observed simultaneously with first example.(*i.e.*, Plate 3) Format is the same as Plate 4.

Figure 1 A summary of the distribution and flow directions of large-scale field-aligned currents determined from data obtained on 493 passes of Triad during weakly disturbed conditions($| AE | < 100$ nT) (from Iijima and Potemra, 1976)

Figure 2 Column emission rate ratios as functions of characteristic electron energy. (from McEwen and Bryant, 1978)

Figure 3 Example of magnetic and electric field perturbations, showing a good correlation between the north-south component of the electric field E_x and the east-west component of the magnetic field ΔB_z. ILAT is invariant latitude, MLAT and MLON are Magnetic latitude and longitude, and GLAT and GLON are geographic latitude and longitude.

Figure 4 Correlation between ΔB_z and E_x values plotted in Figure 3. The correlation coefficient is 0.96.

Figure 5 The relation between the ratio $\Delta B_z/\mu_0 E_x$ and the filter cutoff period. The ratio decreases with decreasing cutoff period.

Figure 6 Twenty examples observed on the dayside, showing a scale length dependence of the ratio $\Delta B_z/\mu_0 E_x$. The data points for which the correlation coefficient between the

magnetic and electric field perturbations is under 0.5 are not connected. The dotted lines on the right and left sides show comparisons of the ratio with the Σ_P deduced from the IRI-86 model (average values in these orbits) and with the Alfvén wave velocity calculated from the observed plasma density and total magnetic force data (assumed O^+ ion dominant), respectively. A case labeled (a) is observed near the terminator.

Figure 7 Twenty examples observed on the nightside. The format is the same as in Figure 4. The case labeled (b) was observed during a magnetically disturbed period (AE=918 nT).

Figure 8 (a and b) Comparison between the calculated Pedersen conductivity from the IRI-86 model and the observed ratio $\Delta B_z/\mu_0 E_x$. (c) Comparison between the calculated Alfvén wave and the ratio $E_x/\Delta B_z$ In Figures 8a and 8b the vertical axis represents the ratio of the observed ΔB_z to E_x, and the abscissa represents the value based on the model. The horizontal bars for the IRI-86 model values show the range of Σ_P along the orbit during the observing period. In Figure 6c the vertical axis represents the ratio E_x to ΔB_z, and the abscissa represents the value calculated from the observed particle density and the magnetic field magnitude. The asterisk represents the values for large scales, and the caret represents values for small scales (see the text).

Figure 9 An example of the "dynamic" correlation. The upper panel shows that the ratio, $\Delta B_z/\mu_0 E_x$ and the lower panel shows the coefficient of correlation between the magnetic and electric fields. The ratio increases along the orbit from the nightside to the dayside.

Figure 10 Comparison between the ratio $\Delta B_z/\mu_0 E_x$ in 20 examples and the Pedersen conductivity based on published models. The ratios for which the correlation coefficient is over 0.75 are averaged with in intervals of 0.5° in zenith angle (irregular curve), and these average ratios are plotted with dots in this figure. The model presented by de la Beaujardier

et al. (Model 4) agrees well with the lower envelope of our results.

Figure 11 Hodograph of the X and Y components of magnetic perturbation on a small scale. The vector rotates four times in the anticlockwise direction.

Figure 12 An example of conductivity profile based on the IRI-86 model and the effective height-integrated Pedersen conductivity $\Sigma_{P,eff}$ calculated from the IRI-86 model. The parameters for the IRI-86 model (season, time, location, and solar activity) are those at the time and location at which the magnetic and electric fields were observed.

a) Conductivity profile of the IRI-86 model. The bold, thin, and dotted lines represent parallel, Pedersen and Hall conductivities.

b) The ionospheric potential profile for each spatial scale-length. It is assumed that $\Phi_k = 1$ at 1000 km and $\Phi_k = 0$ at 0 km altitude.

c) The scale-length dependence of the effective height-integrated Pedersen conductivity $\Sigma_{P,eff}$ calculated from the potential profile in (b).

Figure 13 The plots of 20 satellite passes use. Coordinates are invariant latitude and invariant MLT. Pass 19 is in darkness period, and pass 12 crosses the terminator. Other passes are sunlit passes.

Figure 14 The scale-length dependence of the ratio $\Delta B_z/\mu_0 E_x$, Alfvén velocity, and Pedersen conductivity for the 20 cases. (a) was observed near the terminator (pass 12). (b) was observed in darkness (pass 19). The abscissa represents cut-off periods of high-pass/band-pass filters. The number on each curve corresponds to that in Figure 13.

Figure 15 The scale-length dependence of the difference between the ratio $\Delta B_z/\mu_0 E_x$ and the effective Pedersen conductivity $\Sigma_{P,eff}$.

Figure 16 The scale-length dependence of the normalized difference between the ratio $\Delta B_z / \mu_0 E_x$ and the effective Pedersen conductivity $\Sigma_{P,eff}$.

Figure 17 A schematic figure of the analysis. DE 2 (low altitude satellite) observed the magnetic and electric field data along the orbit indicated "center". Simultaneously, DE 1 (high altitude satellite) obtained the auroral image data, including "left","center",and "right".

Figure 18 The results of comparison between the ratio, $\Delta B_z/\mu_0 E_x$, and the height-integrated Pedersen conductivity, Σ_P, on the morning side case of Plate 1. (a) the magnetic and electric field perturbations obtained by DE 2 observation, variations of correlations between ΔB_z and E_x , and variations of the ratio, $\Delta B_z/\mu_0 E_x$. Horizontal axis of these plots present universal time of DE 2 passage. x and z components represent the North-South and East-West components, respectively. (b) auroral luminosities near the orbit of DE 2, and the ratio, $\Delta B_z/\mu_0 E_x$, in the same invariant latitude. Values of $\Delta B_z/\mu_0 E_x$ is presented by circles and is averaged in the same bin of "average" luminosity (bar chart in the fourth panel). The vertical broken line represents the boundary between regions 1 and 2. (c) scatter plot of the relationship between auroral luminosity and the ratio, $\Delta B_z/\mu_0 E_x$. The dotted line represents the model of Robinson et al.[1989]. The thin and thick lines are the regression lines of data obtained in regions 1 and 2, respectively.

Figure 19 The results of comparison between the ratio, $\Delta B_z/\mu_0 E_x$, and the height-integrated Pedersen conductivity, Σ_P, on the evening side case of Plate 1. Format is same as Fig. 18.

Figure 20 The results of comparison between the ratio, $\Delta B_z/\mu_0 E_x$, and the height-integrated Pedersen conductivity, Σ_P, on the case of Plate 2. Format is the same as in Fig. 18.

Figure 21 The results of comparison between the ratio, $\Delta B_z/\mu_0 E_x$, and the height-integrated Pedersen conductivity, Σ_P, on the case of Plate 3. Format is the same as in Fig. 18.

Figure 22 The total plot of 32 case (a) and their classification by time difference between DE 1 and 2.((b) and (c)) Format is the same as in Fig. 18(c), except for error bars which are removed for clarity. The regression lines are plotted for total data.

Figure 23 The statistical result of the relationship between the auroral luminosity and the ratio, $\Delta B_z/\mu_0 E_x$, arranged as per the local time and relative locations of auroras. (a)Morning side of region 2, (b)Morning side of region 1, (c)Evening side of region 2, and (d)Evening side of region 1. Format is the same as in Fig. 22. The boundaries of invariant latitude between poleward and equatorward are determined from profile of magnetic field perturbations.

Figure 24 The statistical result of the relationship between the auroral luminosity and the ratio, $\Delta B_z/\mu_0 E_x$, classified by the characteristic energy of precipitating particles. The characteristic energies are (a)less than 100 eV,(b)100-500 eV, (c)500 eV-1 keV, and (d)greater than 1keV, respectively. The broken lines in panel (b)(c) and (d) are the model values calculated from Rees et al.[1988], and the dotted line in each panel represents the same by Robinson et al.[1989].

TABLE 1. Filter Cutoff/Passband Periods

High Resolution Data		0.5-s Average	
Cutoff/Passband Period,s	Filter	Passband Period,s	Filter
- 0.25	high pass	1.0 - 2.0	band pass
0.25 - 0.5	band pass	2.0 - 4.0	band pass
0.5 - 1.0	band pass	4.0 - 8.0	band pass
1.0 - 2.0	band pass	8.0 - 16.0	band pass
2.0 - 4.0	band pass	16.0 - 32.0	band pass

Table 2. Investigations on the ratio of the magnetic to electric field perturbation in the high-latitude field-aligned current regions

Table 2

Spacecraft	Authors	
ICB-1300	Israelevich et al.	[1988]
	Dubinin et al.	[1990]
HILAT and rocket	Knudsen et al.	[1990]
EXOS-D	Matsuoka et al.	[1991]
AUREOL-3	Berthelier et al.	[1989]
	Forget et al.	[1991]
Dynamics Explorer 1 / 2	Sugiura	[1984]
	Sugiura et al.	[1982,1983]
	Gurnett et al.	[1984]
	Weimer et al.	[1985,1987]
	Ishii et al.	[1992]

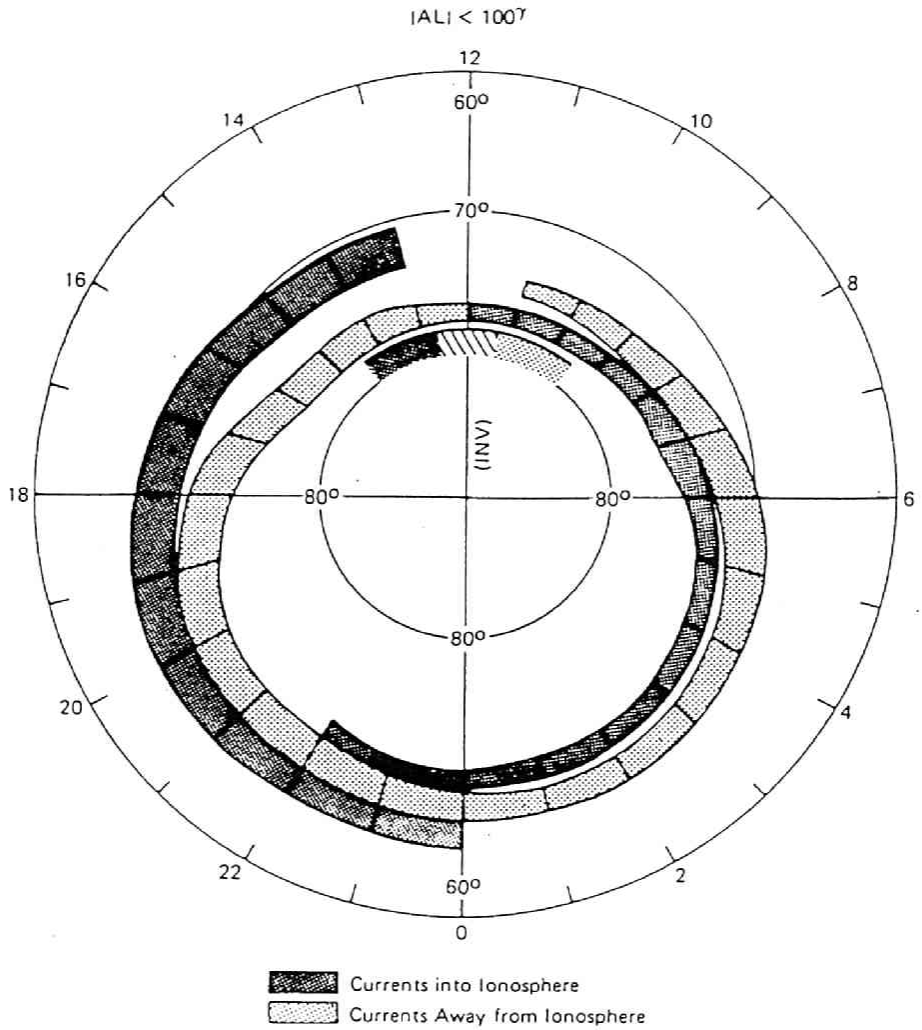
|AL| < 100γ
12
60°
14
10
70°
16
8
(ANI)
18
80°
80°
6
80°
20
4
22
60°
2
0
Currents into Ionosphere
Currents Away from Ionosphere

Figure 1

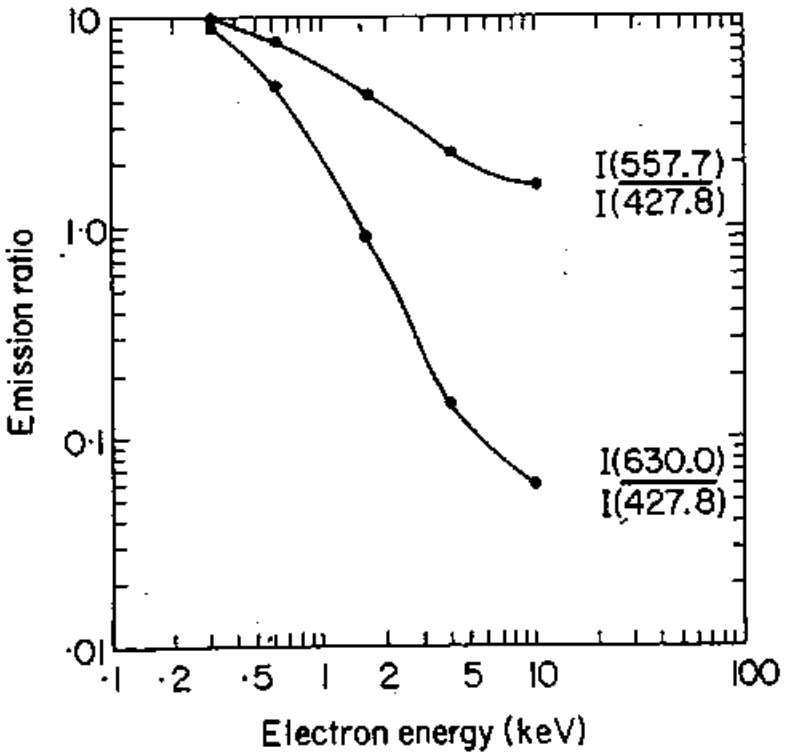
10
1·0
0·1
·01
Emission ratio
I(557.7)
I(427.8)
I(630.0)
I(427.8)
·1
·2
·5
1
2
5
10
100
Electron energy (keV)

Figure 2

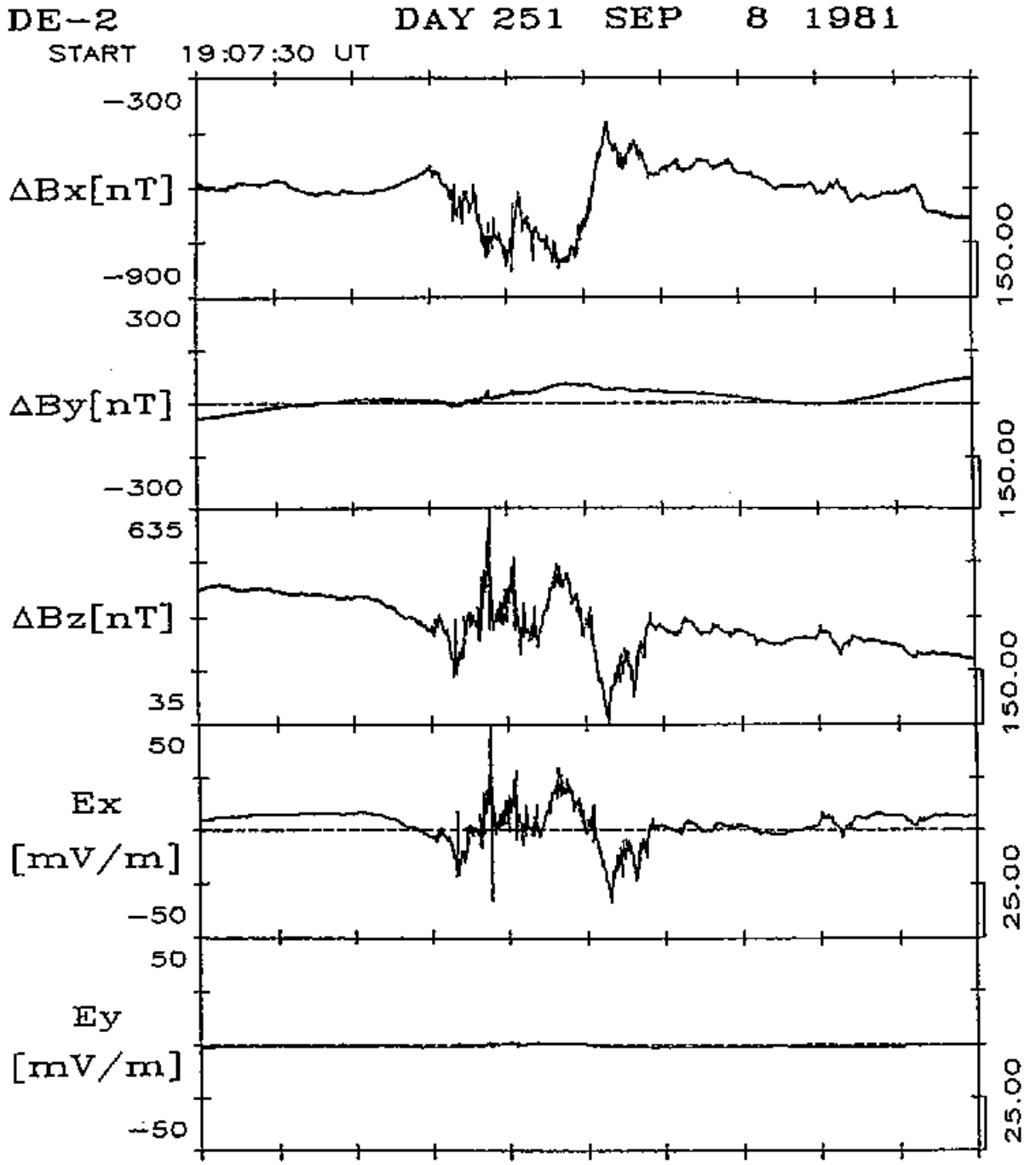

UT	[M:S]	07:30	09:00	10:30	12:00	13:30	15:00
ALT	[KM]	322	315	312	312	314	321
MLT	[DEG]	10.4	9.9	8.9	7.1	4.4	2.6
ILAT	[DEG]	68.5	74.0	79.2	83.4	---	81.5
MLAT	[DEG]	67.5	73.0	78.0	81.6	81.6	78.1
MLON	[DEG]	-61.5	-69.2	-83.3	-111.9	-154.6	176.7
GLAT	[DEG]	60.6	66.6	72.7	78.8	84.9	89.0
GLON	[DEG]	-113.9	-114.2	-114.6	-114.9	-115.2	63.5
LT	[HR]	11.6	11.6	11.6	11.6	11.6	23.5

Figure 3

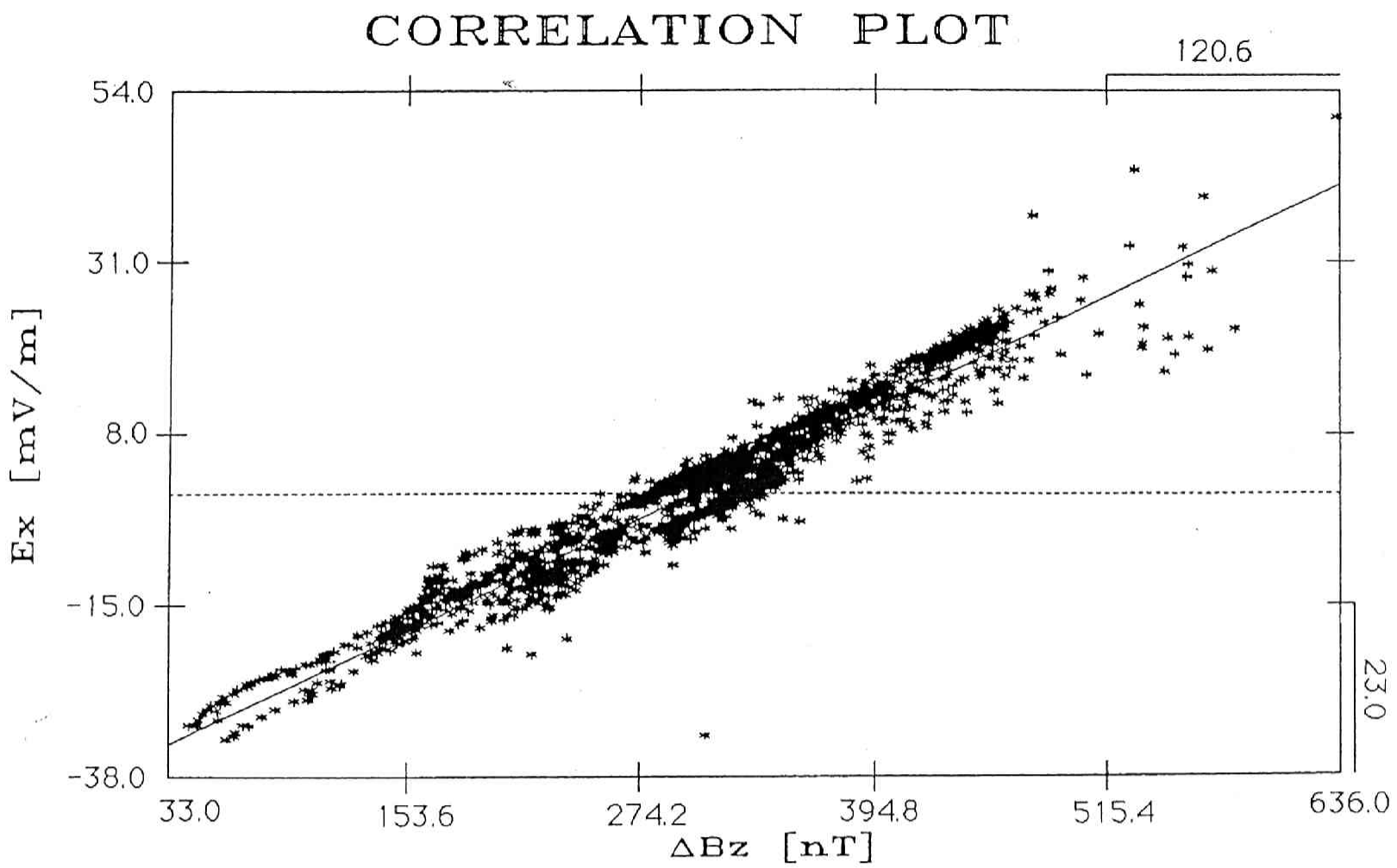
CORRELATION PLOT
120.6
54.0
31.0
8.0
-15.0
-38.0
Ex [mV/m]
23.0
33.0
153.6
274.2
394.8
515.4
636.0
ΔBz [nT]

Figure 4

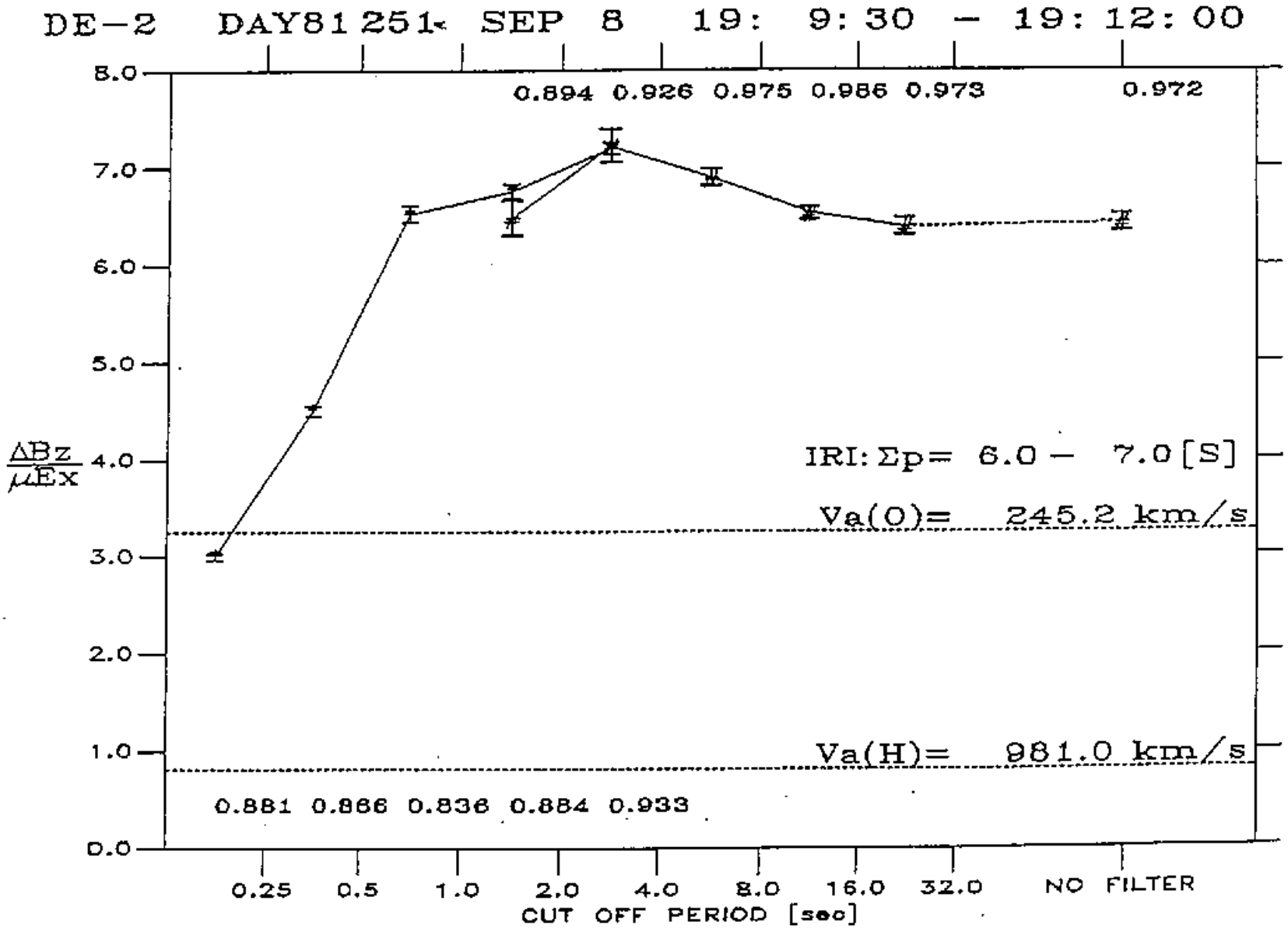
DE-2 DAY81 251 SEP 8 19: 9:30 - 19: 12: 00
0.894 0.926 0.975 0.986 0.973 0.972
8.0
7.0
6.0
5.0
4.0
3.0
2.0
1.0
0.0
ΔBz / μEx
IRI: Σp= 6.0 - 7.0 [S]
Va(O)= 245.2 km/s
Va(H)= 981.0 km/s
0.881 0.866 0.836 0.884 0.933
0.25 0.5 1.0 2.0 4.0 8.0 16.0 32.0 NO FILTER
CUT OFF PERIOD [sec]

Figure 5

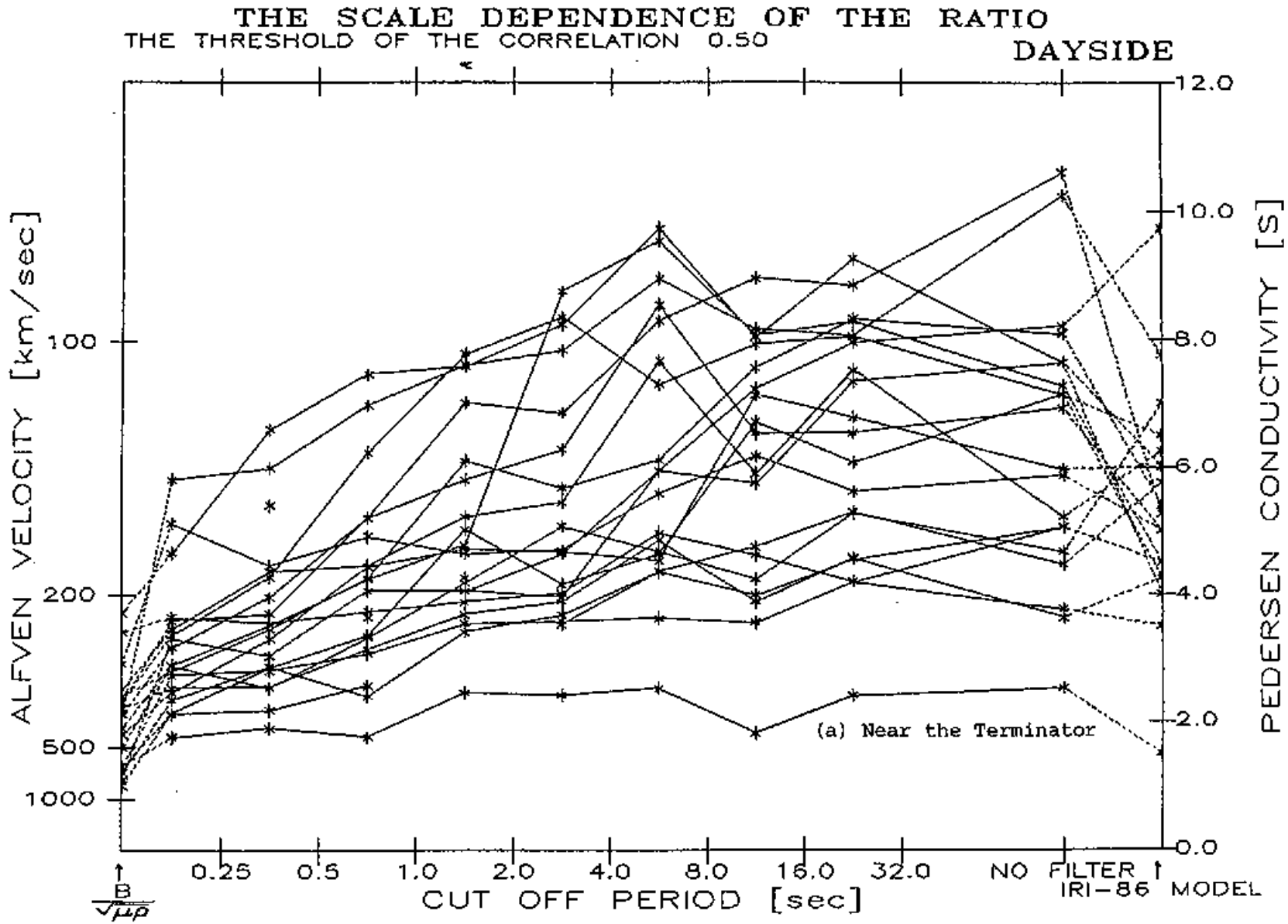
THE SCALE DEPENDENCE OF THE RATIO
THE THRESHOLD OF THE CORRELATION 0.50
DAYSIDE
ALFVEN VELOCITY [km/sec]
100
200
500
1000
12.0
10.0
8.0
6.0
4.0
2.0
0.0
PEDERSEN CONDUCTIVITY [S]
(a) Near the Terminator
0.25
0.5
1.0
2.0
4.0
8.0
16.0
32.0
NO FILTER
B / √μρ
CUT OFF PERIOD [sec]
IRI-86 MODEL

Figure 6

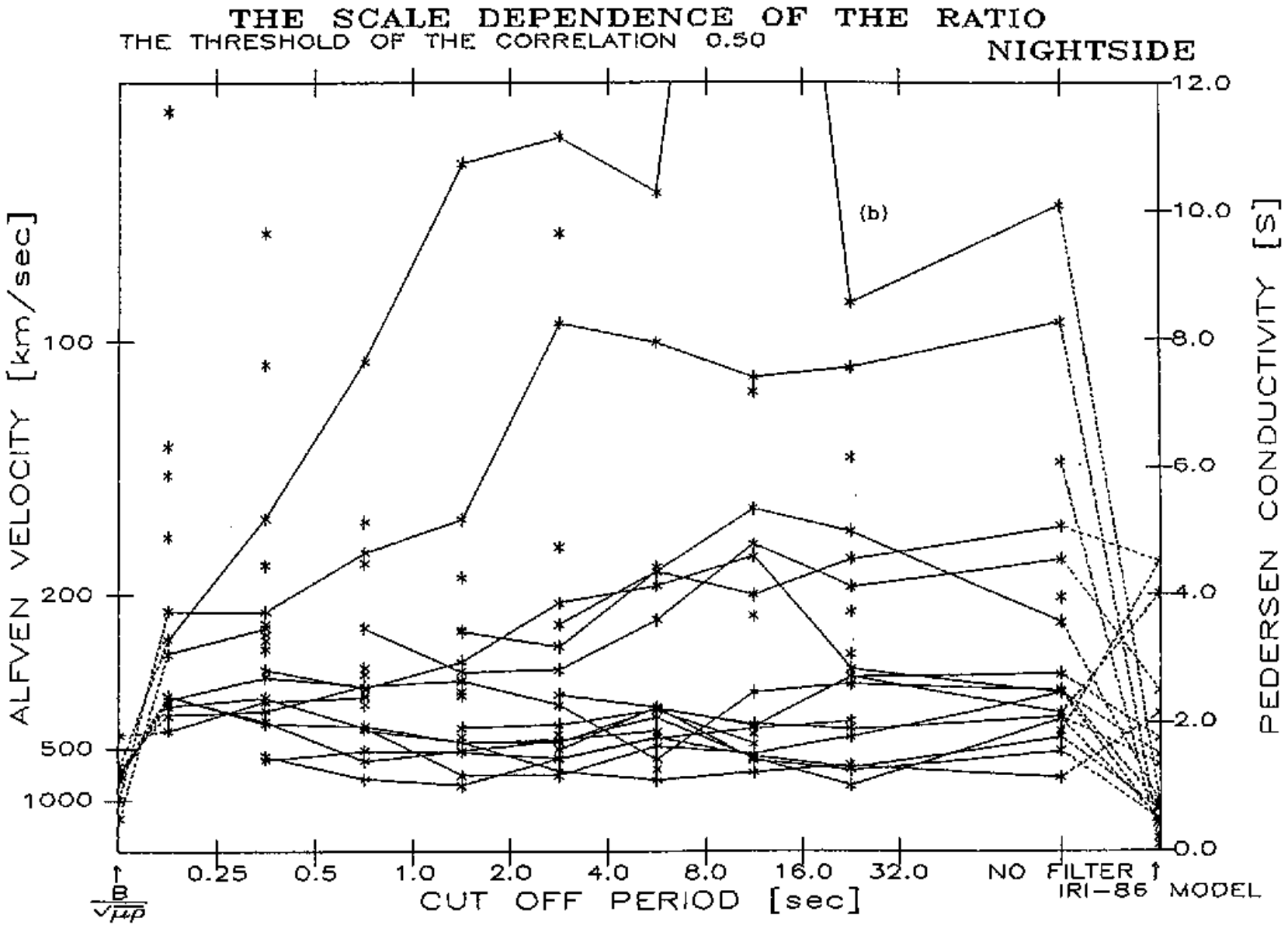
THE SCALE DEPENDENCE OF THE RATIO
THE THRESHOLD OF THE CORRELATION 0.50
NIGHTSIDE
(b)
ALFVEN VELOCITY [km/sec]
100
200
500
1000
12.0
10.0
8.0
6.0
4.0
2.0
0.0
PEDERSEN CONDUCTIVITY [S]
0.25
0.5
1.0
2.0
4.0
8.0
16.0
32.0
NO FILTER
B/√μρ
CUT OFF PERIOD [sec]
IRI-86 MODEL

Figure 7

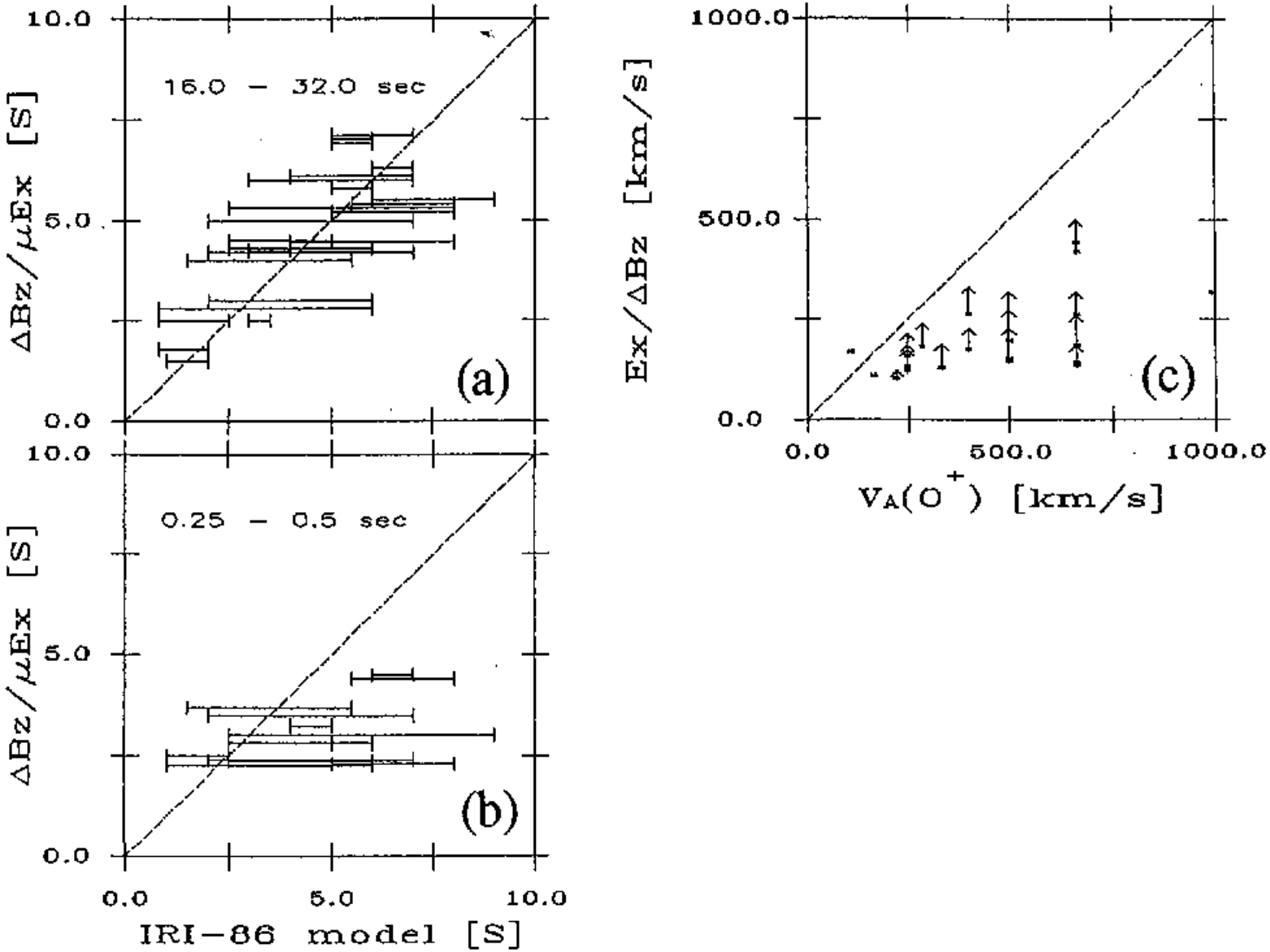
10.0
16.0 – 32.0 sec
ΔBz/μEx [S]
5.0
0.0
(a)
10.0
0.25 – 0.5 sec
ΔBz/μEx [S]
5.0
0.0
(b)
0.0
5.0
10.0
IRI-86 model [S]
1000.0
Ex/ΔBz [km/s]
500.0
0.0
(c)
0.0
500.0
1000.0
VA(O+) [km/s]

Figure 8

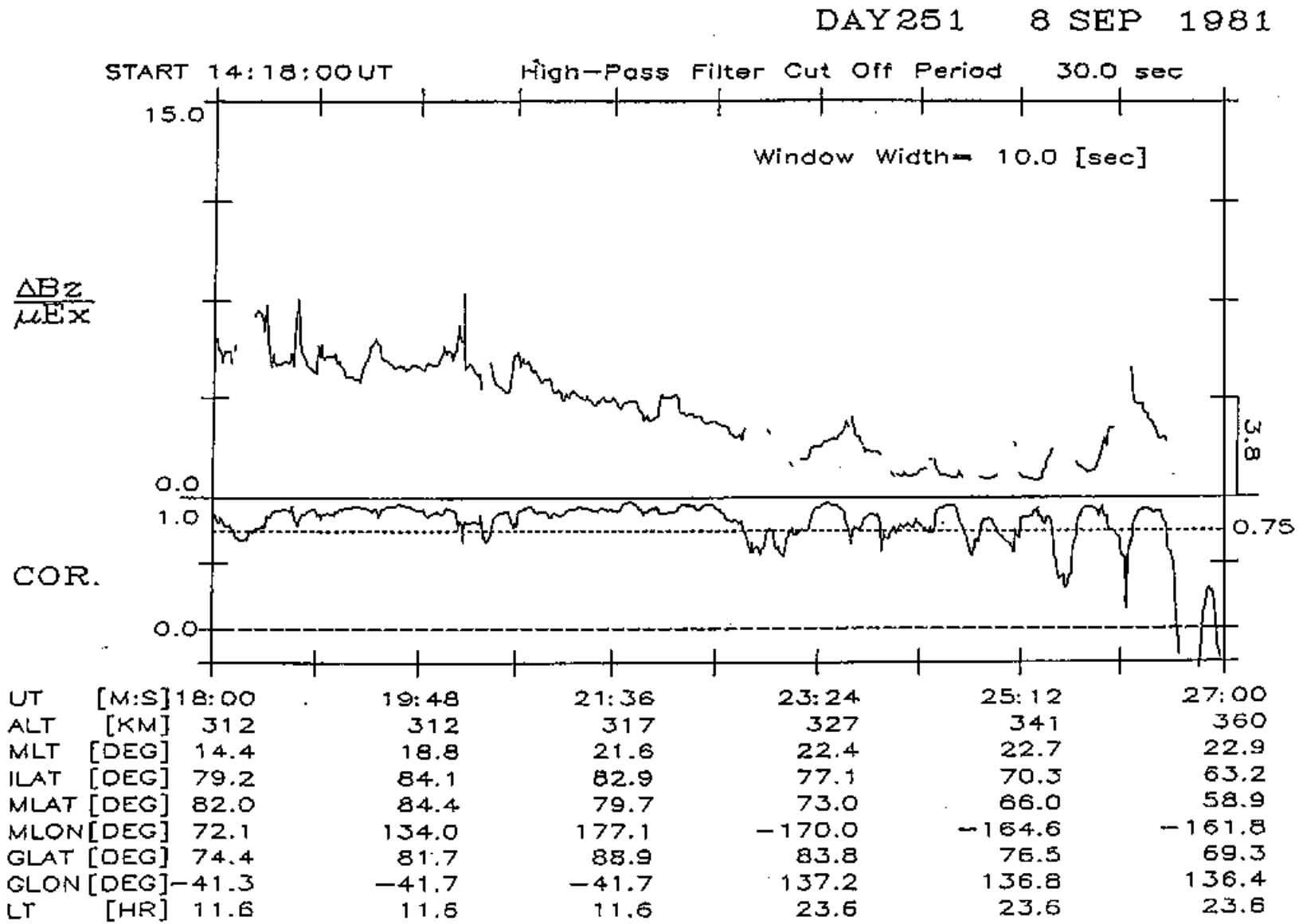
DAY251 8 SEP 1981
START 14:18:00UT
High-Pass Filter Cut Off Period 30.0 sec
Window Width= 10.0 [sec]
15.0
ΔBz/μEx
0.0
3.8
1.0
0.75
COR.
0.0
UT [M:S] 18:00 19:48 21:36 23:24 25:12 27:00
ALT [KM] 312 312 317 327 341 360
MLT [DEG] 14.4 18.8 21.6 22.4 22.7 22.9
ILAT [DEG] 79.2 84.1 82.9 77.1 70.3 63.2
MLAT [DEG] 82.0 84.4 79.7 73.0 66.0 58.9
MLON [DEG] 72.1 134.0 177.1 -170.0 -164.6 -161.8
GLAT [DEG] 74.4 81.7 88.9 83.8 76.5 69.3
GLON [DEG] -41.3 -41.7 -41.7 137.2 136.8 136.4
LT [HR] 11.6 11.6 11.6 23.6 23.6 23.6

Figure 9

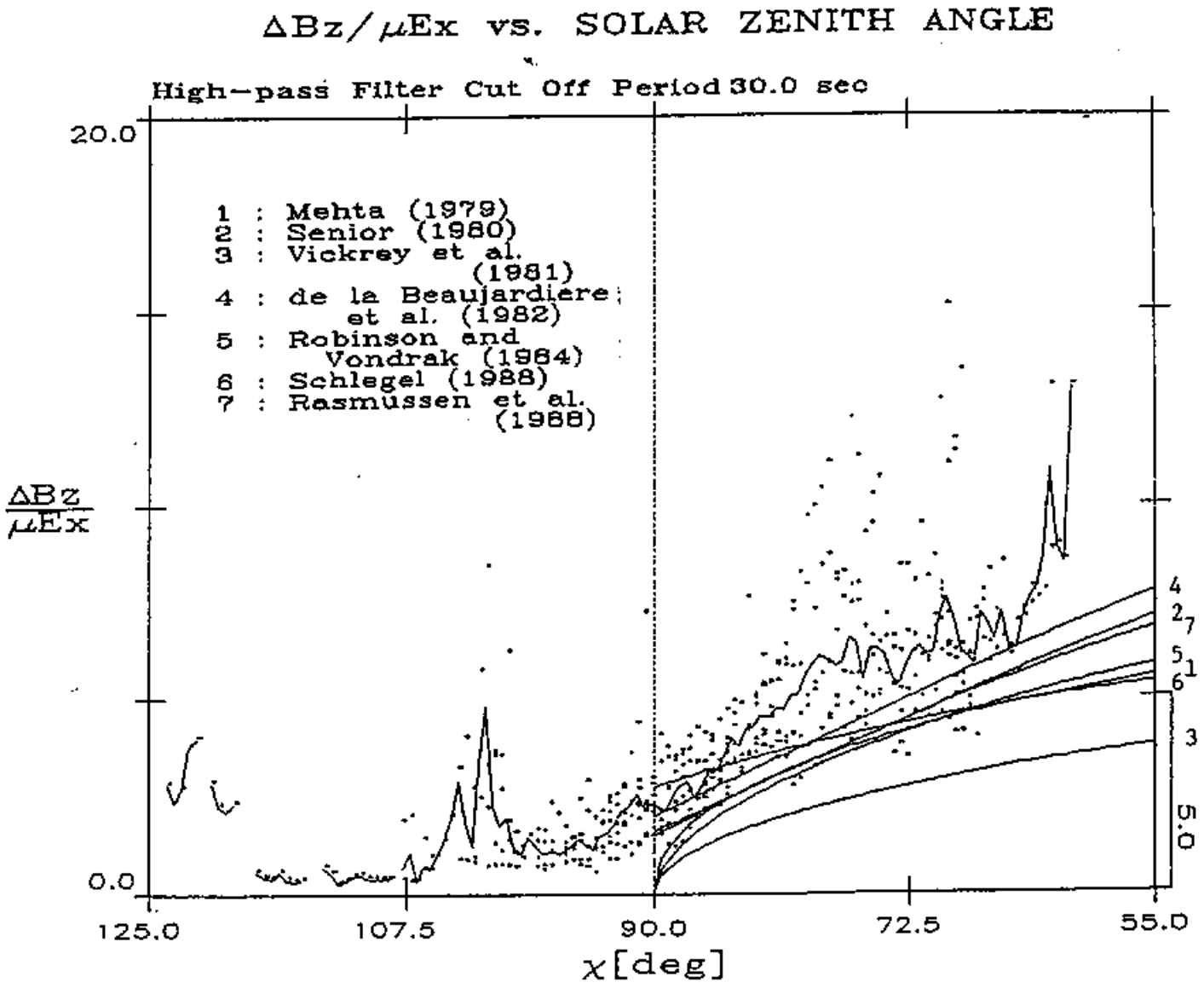
ΔBz/μEx vs. SOLAR ZENITH ANGLE
High-pass Filter Cut Off Period 30.0 sec
20.0
0.0
1 : Mehta (1979)
2 : Senior (1980)
3 : Vickrey et al. (1981)
4 : de la Beaujardiere et al. (1982)
5 : Robinson and Vondrak (1984)
6 : Schlegel (1988)
7 : Rasmussen et al. (1988)
ΔBz / μEx
4
2
7
5
1
6
3
5.0
125.0
107.5
90.0
72.5
55.0
χ[deg]

Figure 10

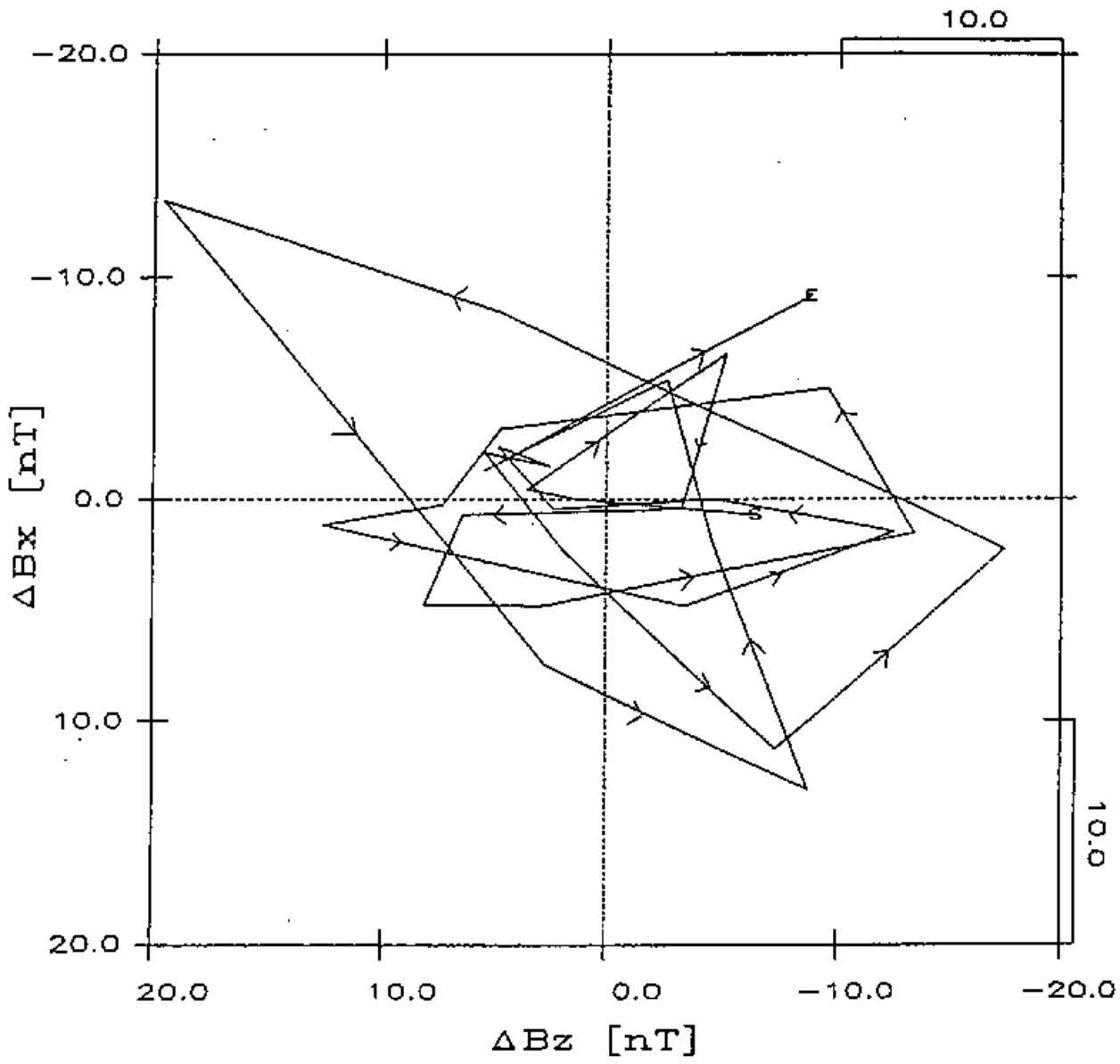

Figure 11

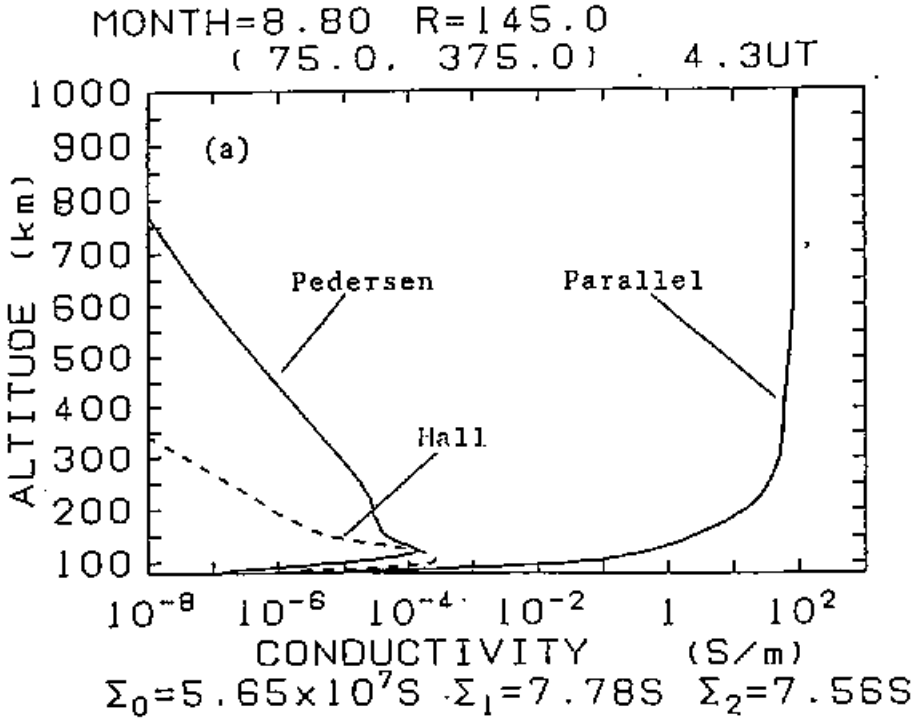
MONTH=8.80 R=145.0
(75.0, 375.0) 4.3UT
(a)
Pedersen
Parallel
Hall
ALTITUDE (km)
1000
900
800
700
600
500
400
300
200
100
10^{-8} 10^{-6} 10^{-4} 10^{-2} 1 10^{2}
CONDUCTIVITY (S/m)
Σ_0=5.65x10^7S Σ_1=7.78S Σ_2=7.56S

Figure 12

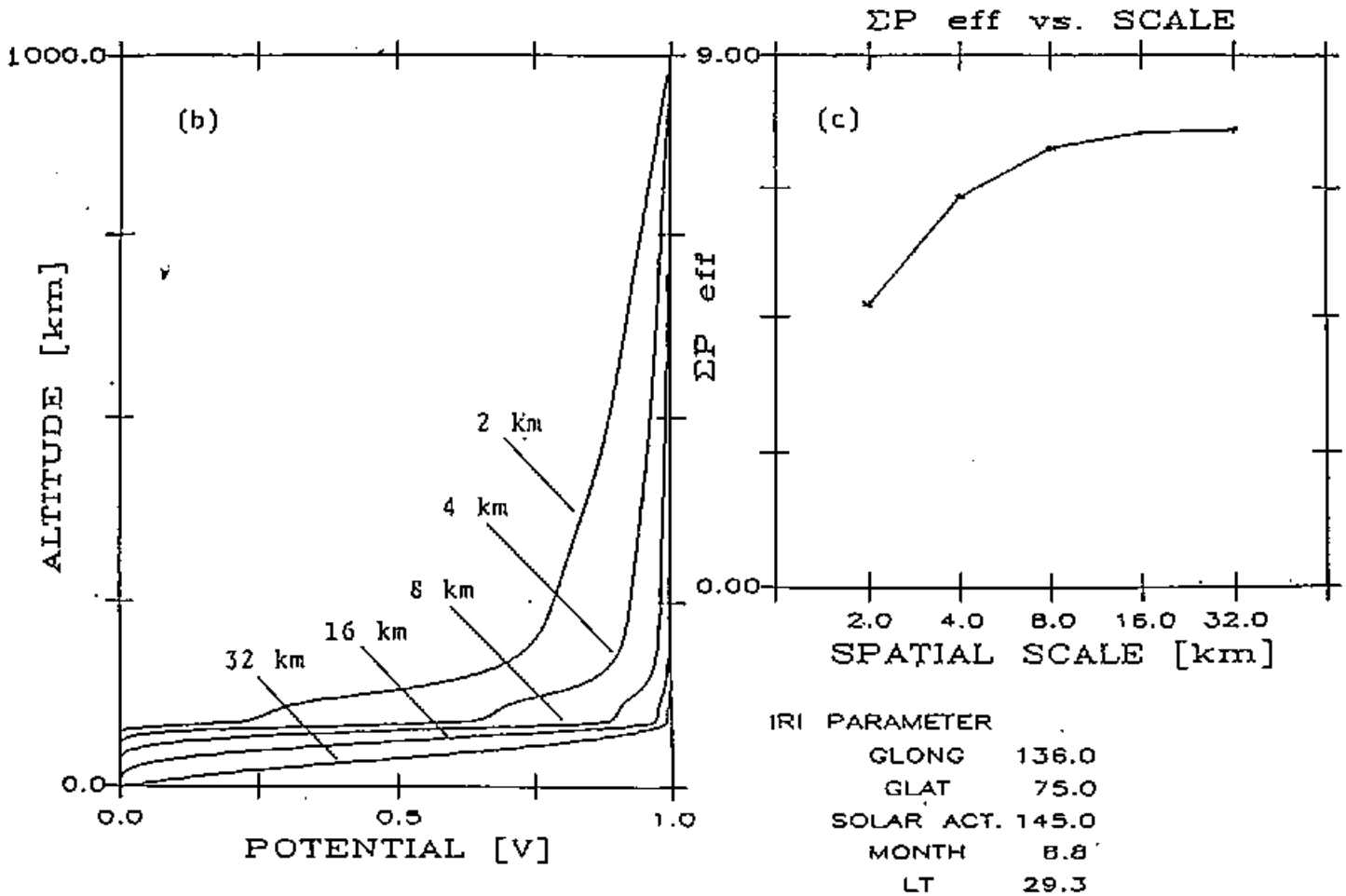
(b)
1000.0
0.0
ALTITUDE [km]
2 km
4 km
8 km
16 km
32 km
0.0
0.5
1.0
POTENTIAL [V]
ΣP eff vs. SCALE
(c)
9.00
0.00
ΣP eff
2.0 4.0 8.0 16.0 32.0
SPATIAL SCALE [km]
IRI PARAMETER
GLONG 136.0
GLAT 75.0
SOLAR ACT. 145.0
MONTH 8.8
LT 29.3

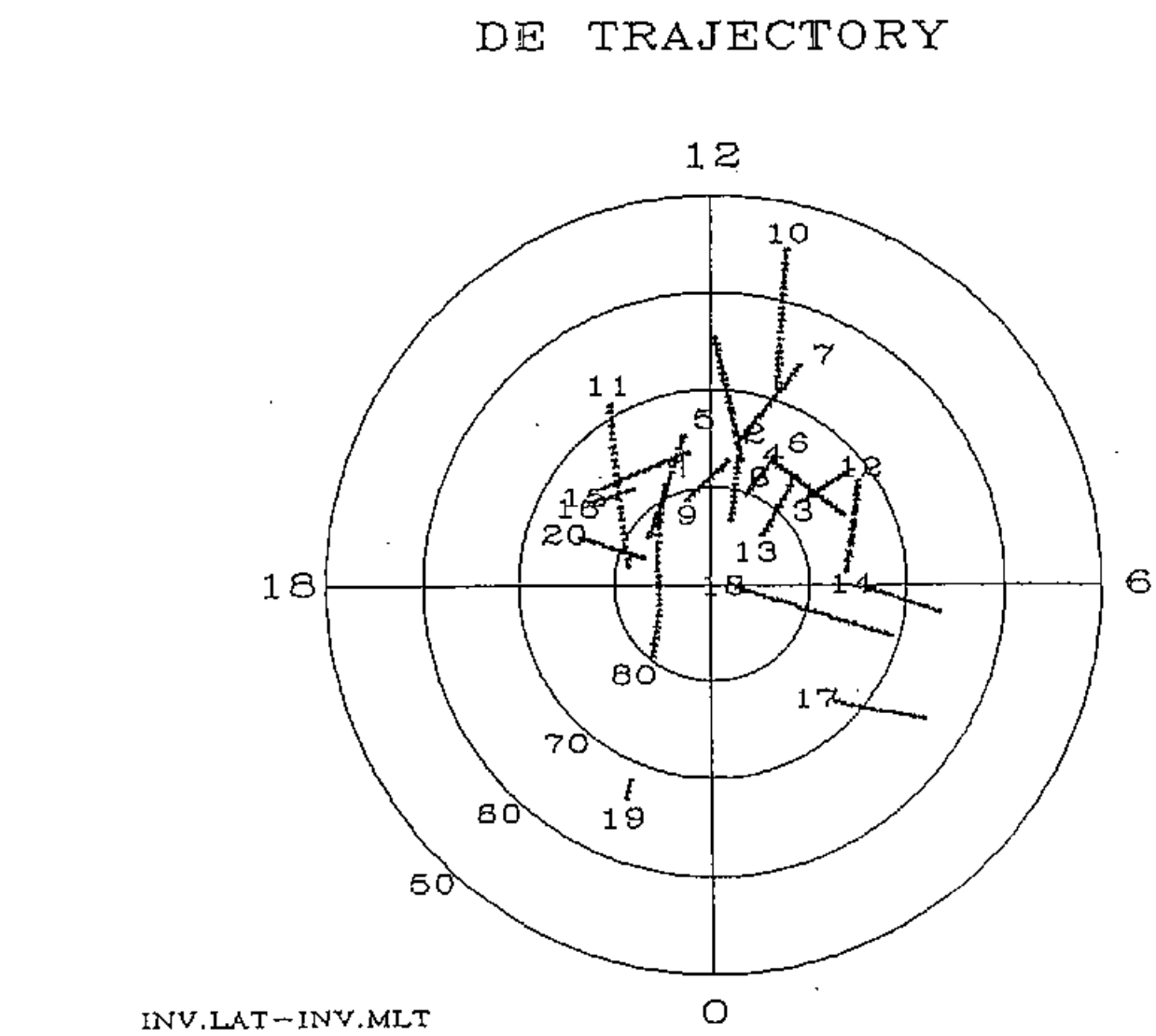
DE TRAJECTORY
12
10
7
11
5
2
6
4
8
12
15
16
9
3
20
13
18
6
14
80
17
70
19
60
50
0
INV.LAT–INV.MLT

Figure 13

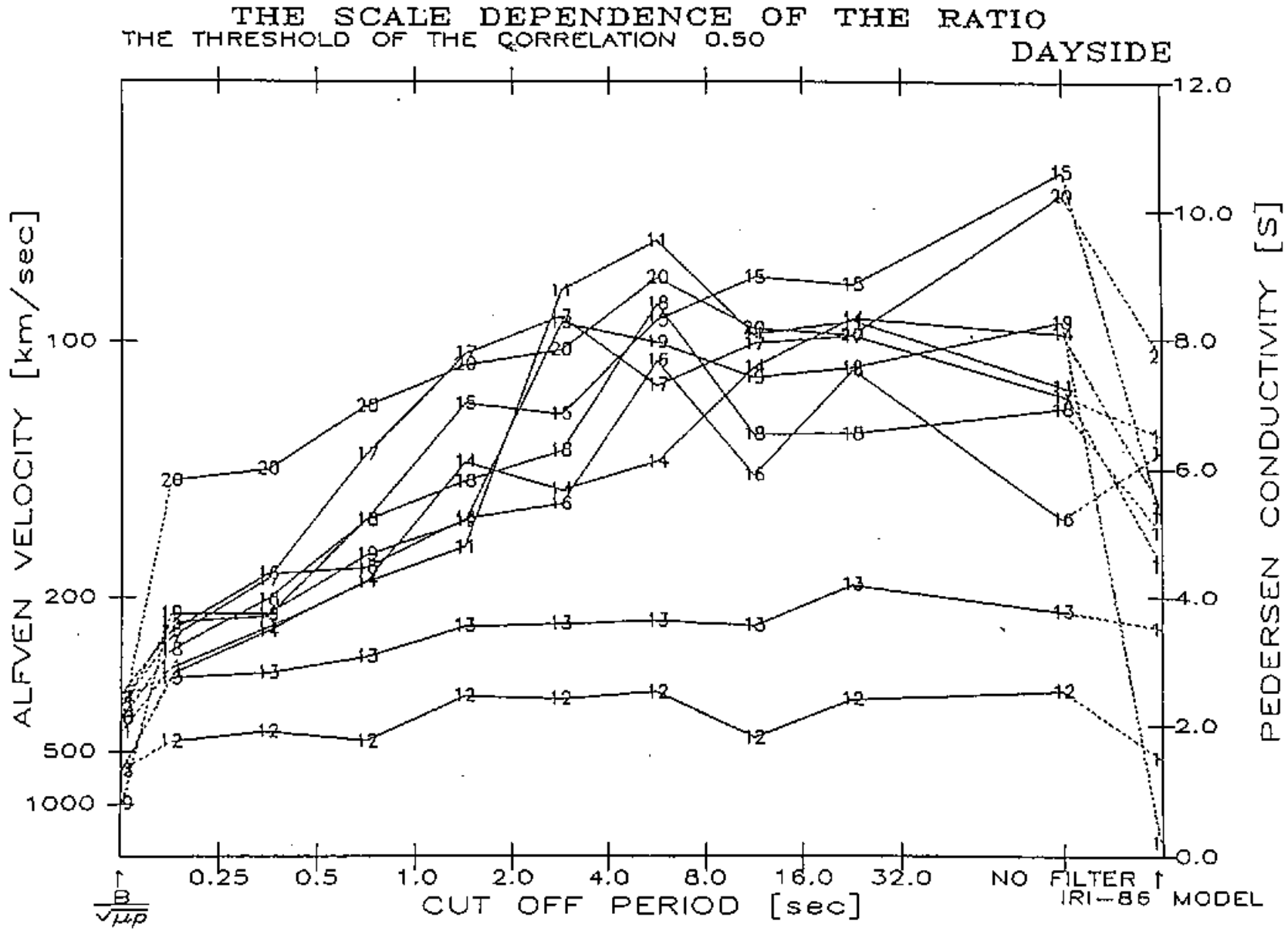
THE SCALE DEPENDENCE OF THE RATIO
THE THRESHOLD OF THE CORRELATION 0.50
DAYSIDE
ALFVEN VELOCITY [km/sec]
PEDERSEN CONDUCTIVITY [S]
100
200
500
1000
12.0
10.0
8.0
6.0
4.0
2.0
0.0
0.25
0.5
1.0
2.0
4.0
8.0
16.0
32.0
NO FILTER
CUT OFF PERIOD [sec]
B/√μρ
IRI-86 MODEL

Figure 14 (a)

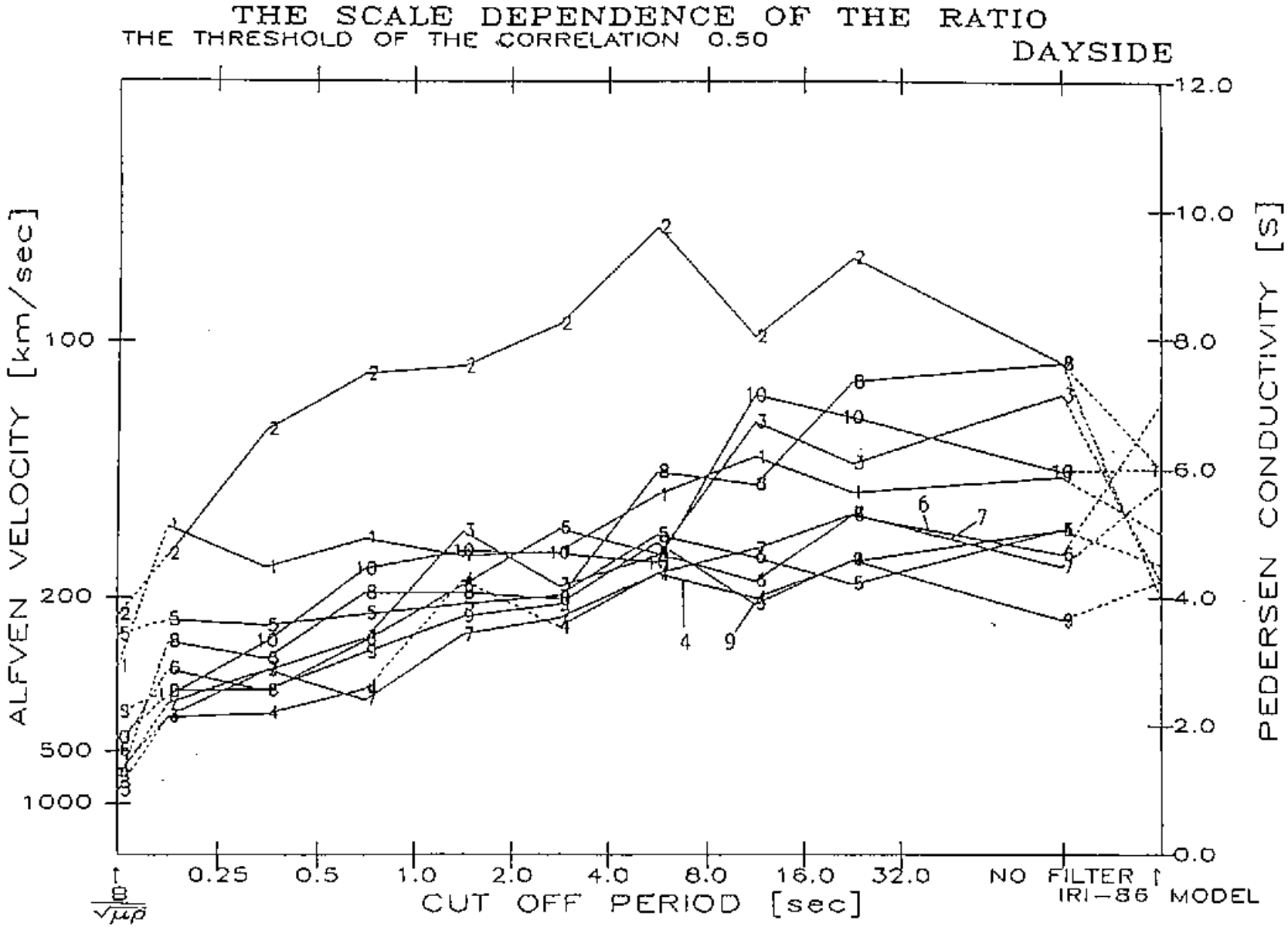
THE SCALE DEPENDENCE OF THE RATIO
THE THRESHOLD OF THE CORRELATION 0.50
DAYSIDE
ALFVEN VELOCITY [km/sec]
PEDERSEN CONDUCTIVITY [S]
100
200
500
1000
12.0
10.0
8.0
6.0
4.0
2.0
0.0
0.25
0.5
1.0
2.0
4.0
8.0
16.0
32.0
NO FILTER
IRI-86 MODEL
CUT OFF PERIOD [sec]

Figure 14 (b)

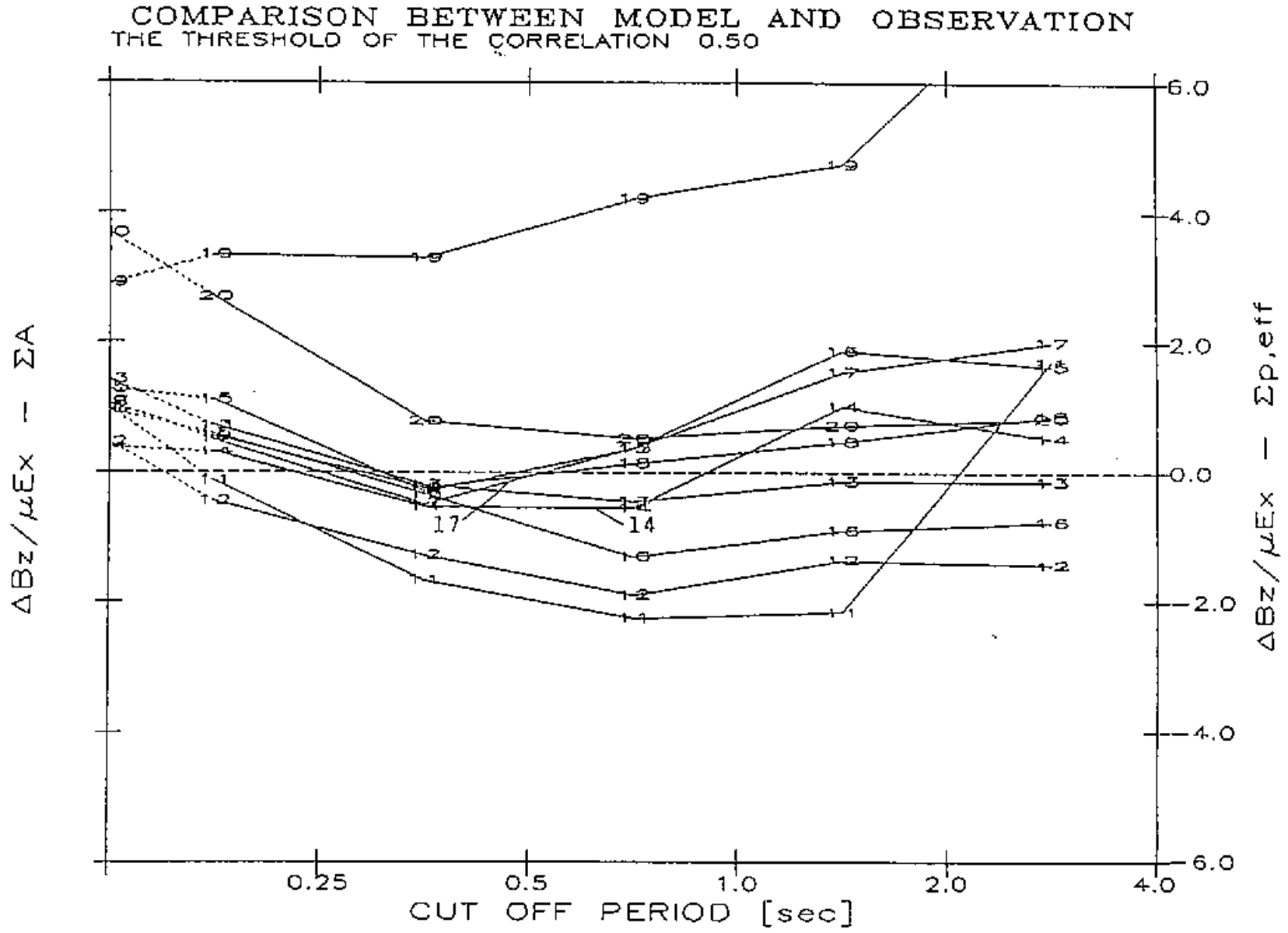
COMPARISON BETWEEN MODEL AND OBSERVATION
THE THRESHOLD OF THE CORRELATION 0.50
ΔBz/μEx − ΣA
ΔBz/μEx − Σp,eff
6.0
4.0
2.0
0.0
2.0
4.0
6.0
0.25
0.5
1.0
2.0
4.0
CUT OFF PERIOD [sec]

Figure 15 (a)

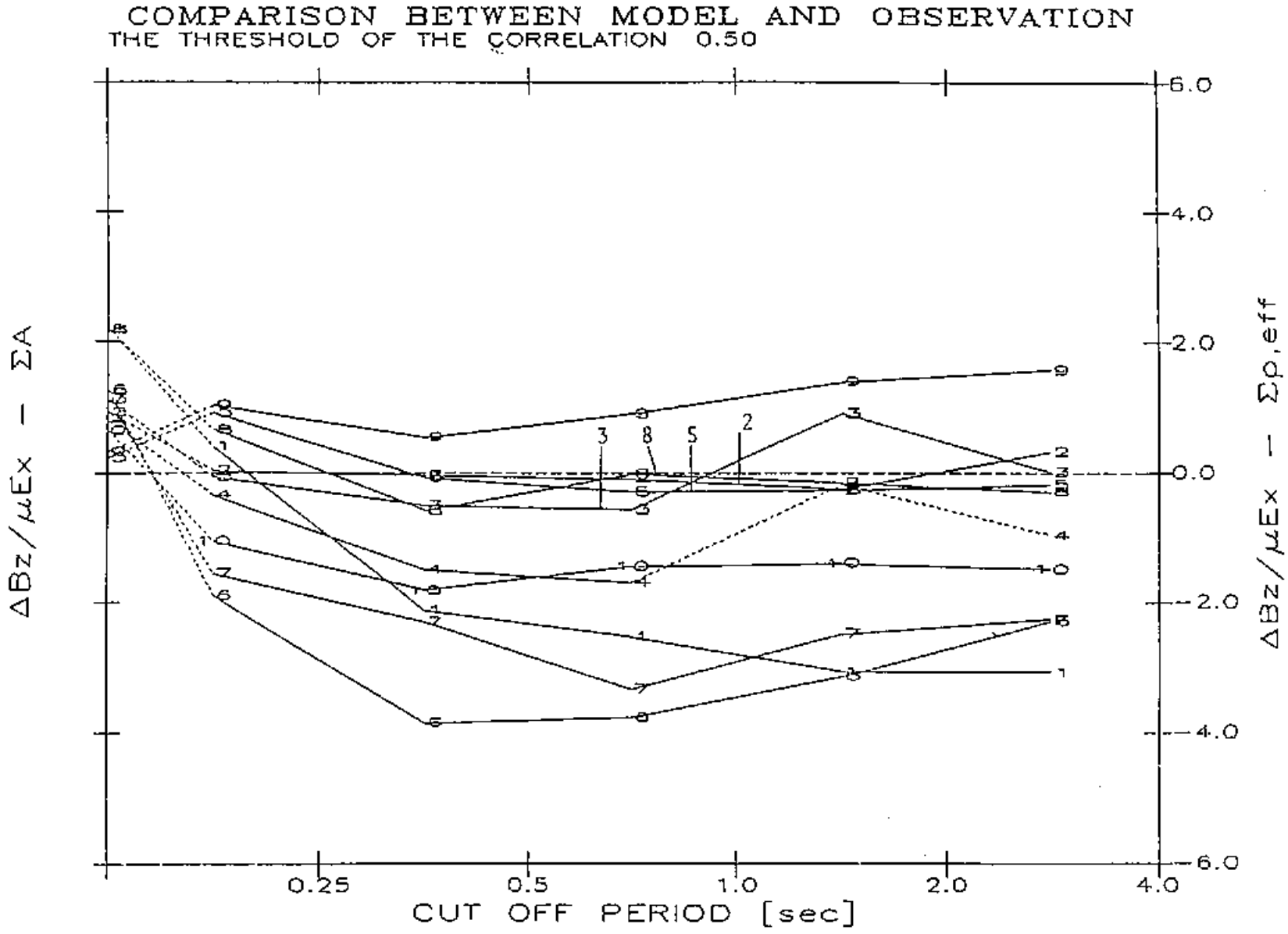
COMPARISON BETWEEN MODEL AND OBSERVATION
THE THRESHOLD OF THE CORRELATION 0.50
ΔBz/μEx − ΣA
ΔBz/μEx − Σρ,eff
6.0
4.0
2.0
0.0
2.0
4.0
6.0
0.25
0.5
1.0
2.0
4.0
CUT OFF PERIOD [sec]

Figure 15 (b)

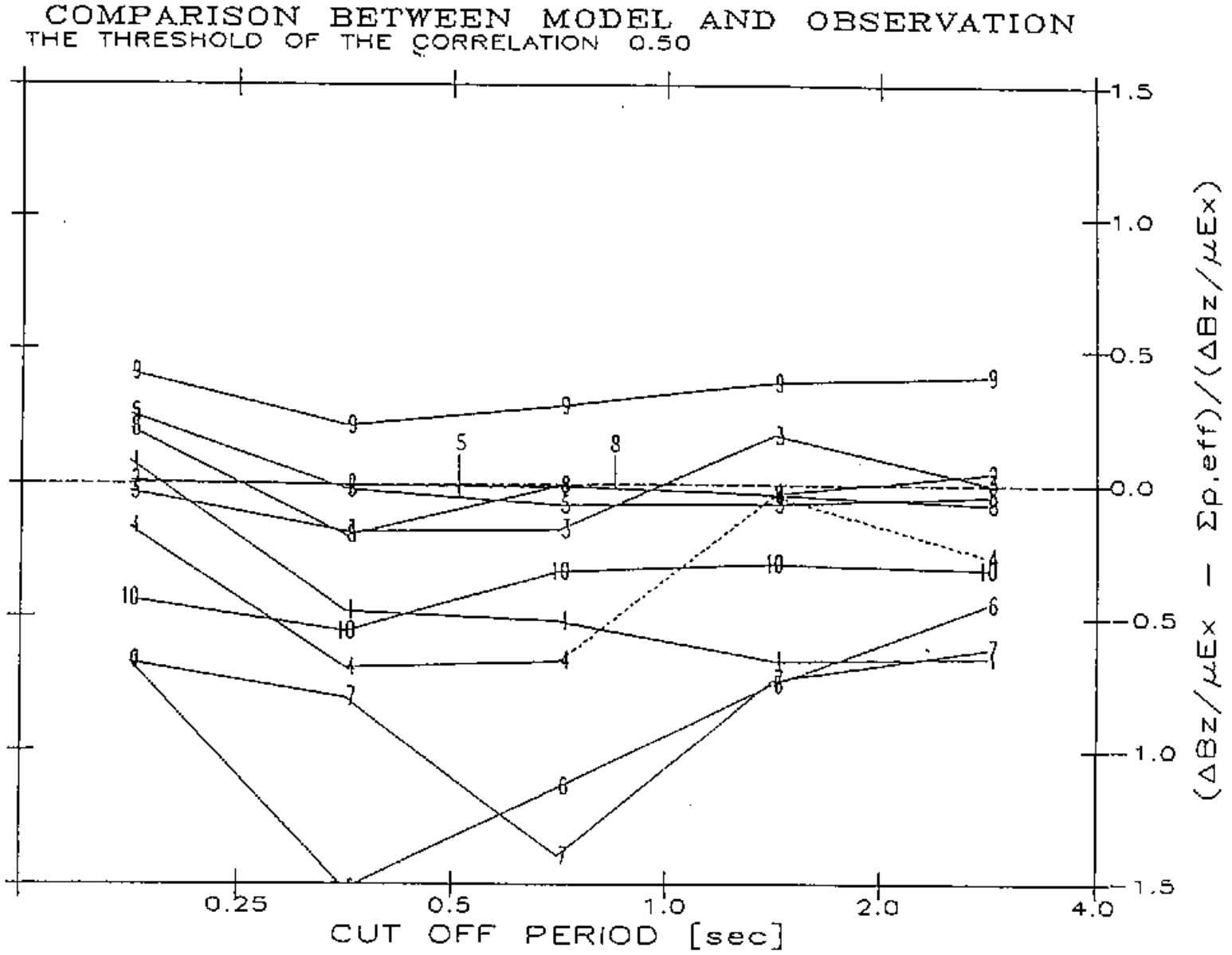
COMPARISON BETWEEN MODEL AND OBSERVATION
THE THRESHOLD OF THE CORRELATION 0.50
1.5
1.0
0.5
0.0
0.5
1.0
1.5
(ΔBz/μEx − Σp,eff)/(ΔBz/μEx)
0.25
0.5
1.0
2.0
4.0
CUT OFF PERIOD [sec]

Figure 16 (a)

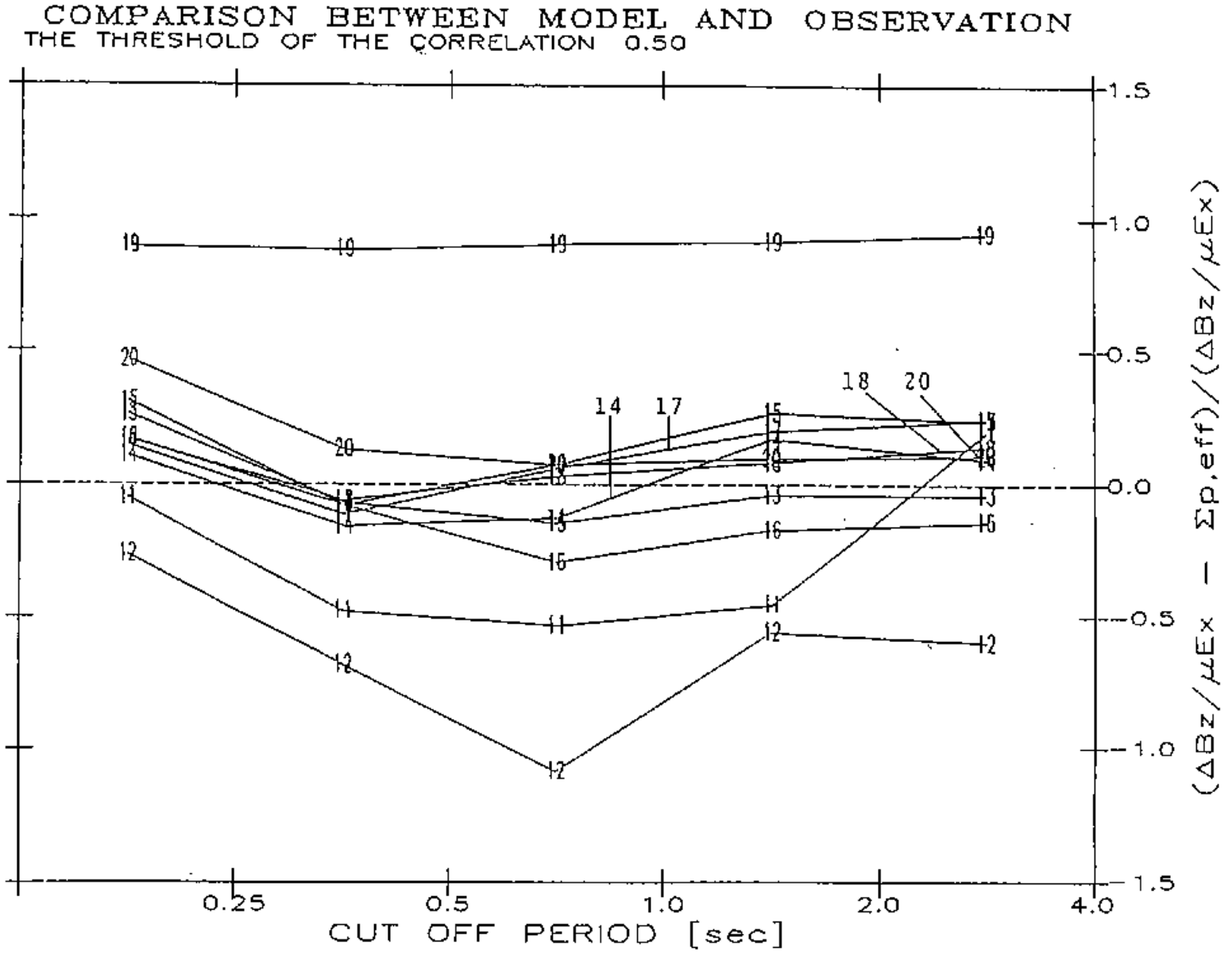
COMPARISON BETWEEN MODEL AND OBSERVATION
THE THRESHOLD OF THE CORRELATION 0.50
1.5
1.0
0.5
0.0
-0.5
-1.0
-1.5
(ΔBz/μEx − Σρ,eff)/(ΔBz/μEx)
0.25
0.5
1.0
2.0
4.0
CUT OFF PERIOD [sec]

Figure 16 (b)

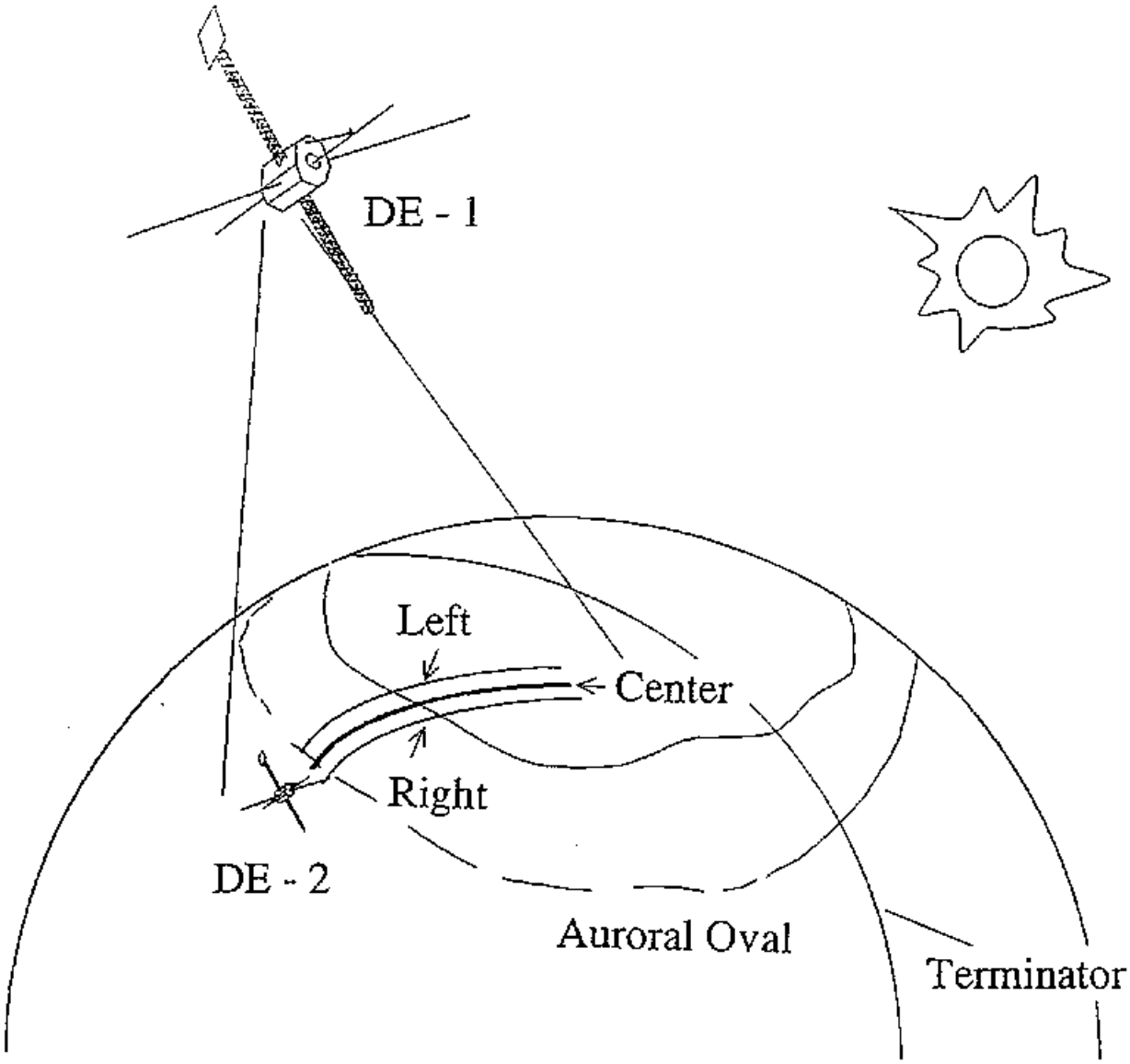

Figure 17

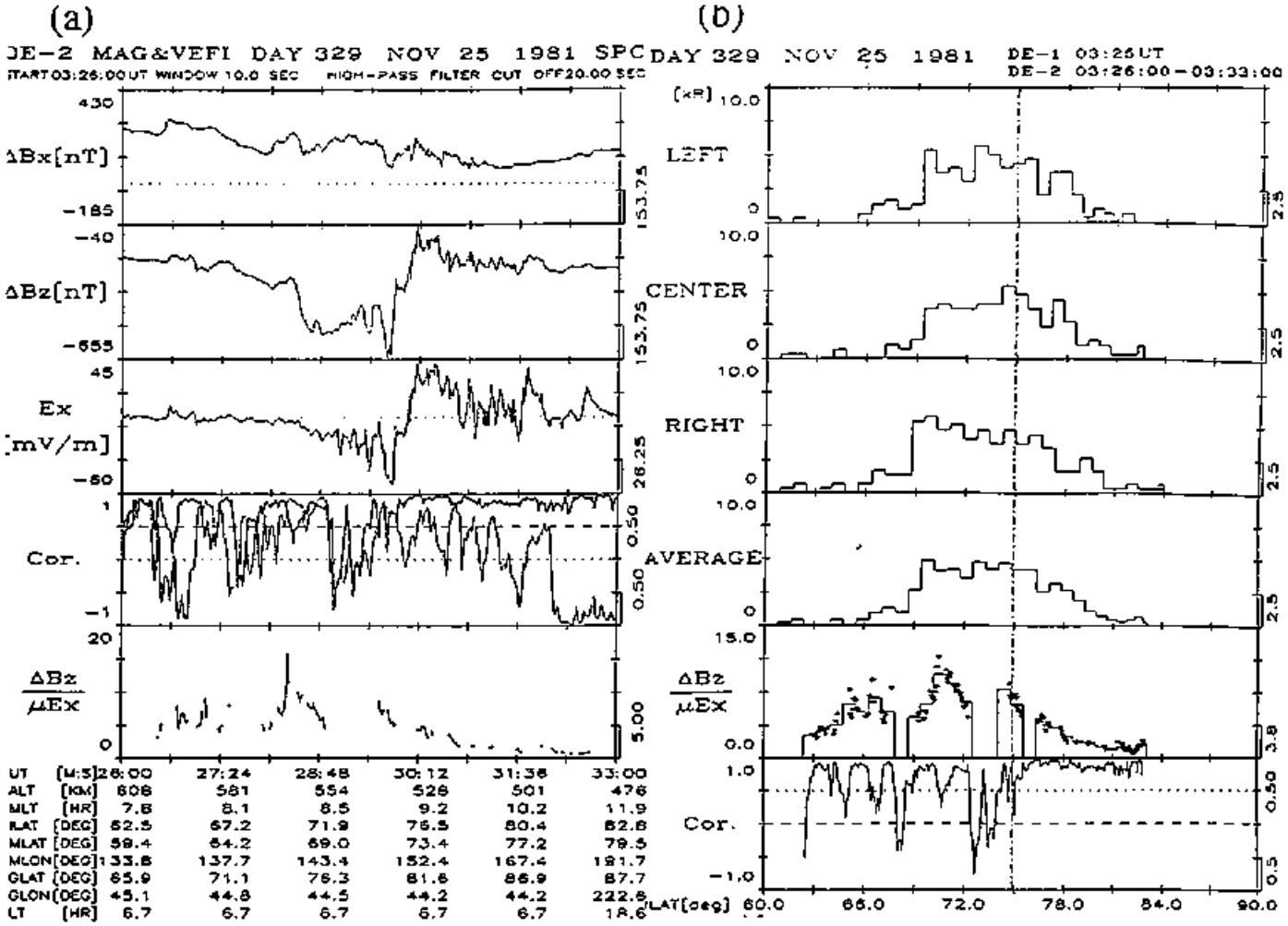
(a)
(b)
DE-2 MAG&VEFI DAY 329 NOV 25 1981 SPC
DAY 329 NOV 25 1981
DE-1 03:25UT
DE-2 03:26:00-03:33:00
ΔBx[nT]
ΔBz[nT]
Ex [mV/m]
Cor.
ΔBz/μEx
LEFT
CENTER
RIGHT
AVERAGE
UT (M:S) 26:00 27:24 28:48 30:12 31:38 33:00
ALT (KM) 608 581 554 528 501 476
MLT (HR) 7.8 8.1 8.5 9.2 10.2 11.9
MLAT (DEG) 59.4 64.2 69.0 73.4 77.2 79.5
GLAT (DEG) 65.9 71.1 76.3 81.6 86.9 87.7
GLON (DEG) 45.1 44.8 44.5 44.2 44.2 222.6
LT (HR) 6.7 6.7 6.7 6.7 6.7 18.6
MLAT (deg) 60.0 66.0 72.0 78.0 84.0 90.0

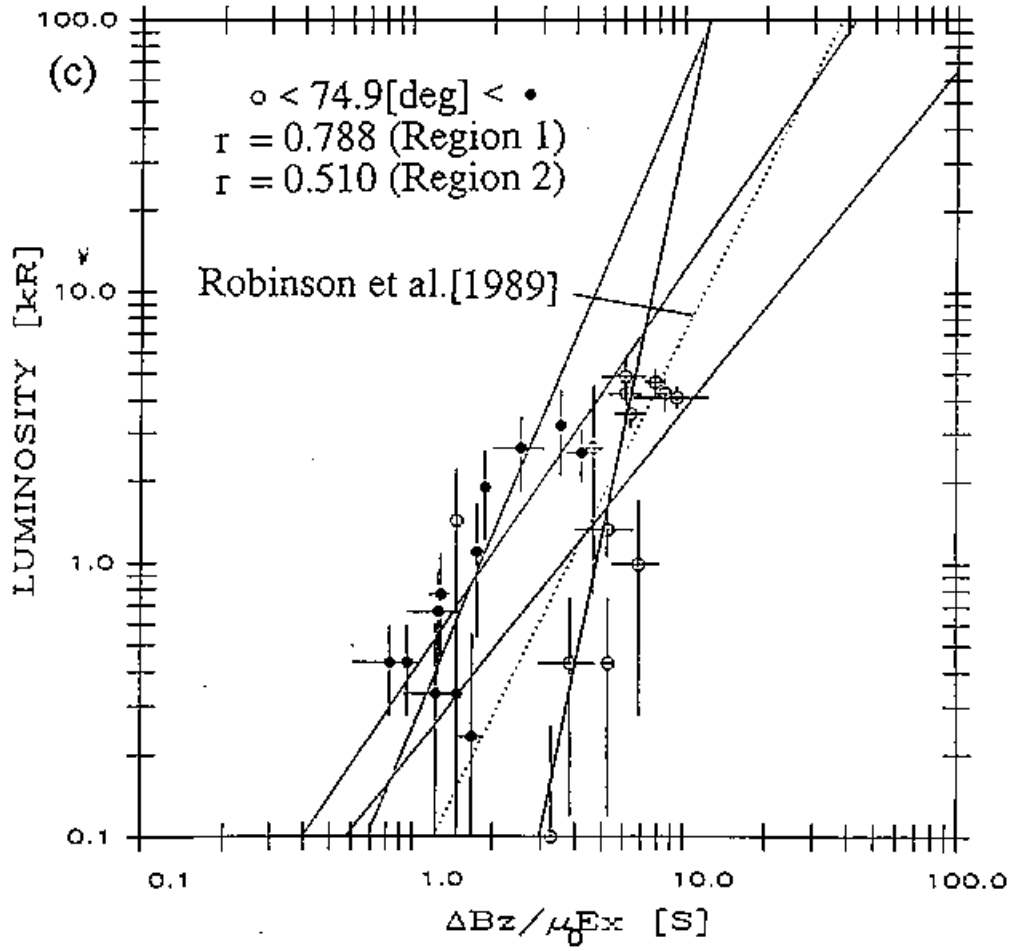
(c)
o < 74.9[deg] < •
r = 0.788 (Region 1)
r = 0.510 (Region 2)
Robinson et al.[1989]
LUMINOSITY [kR]
ΔBz/μ0Ex [S]
0.1
1.0
10.0
100.0

Figure 18

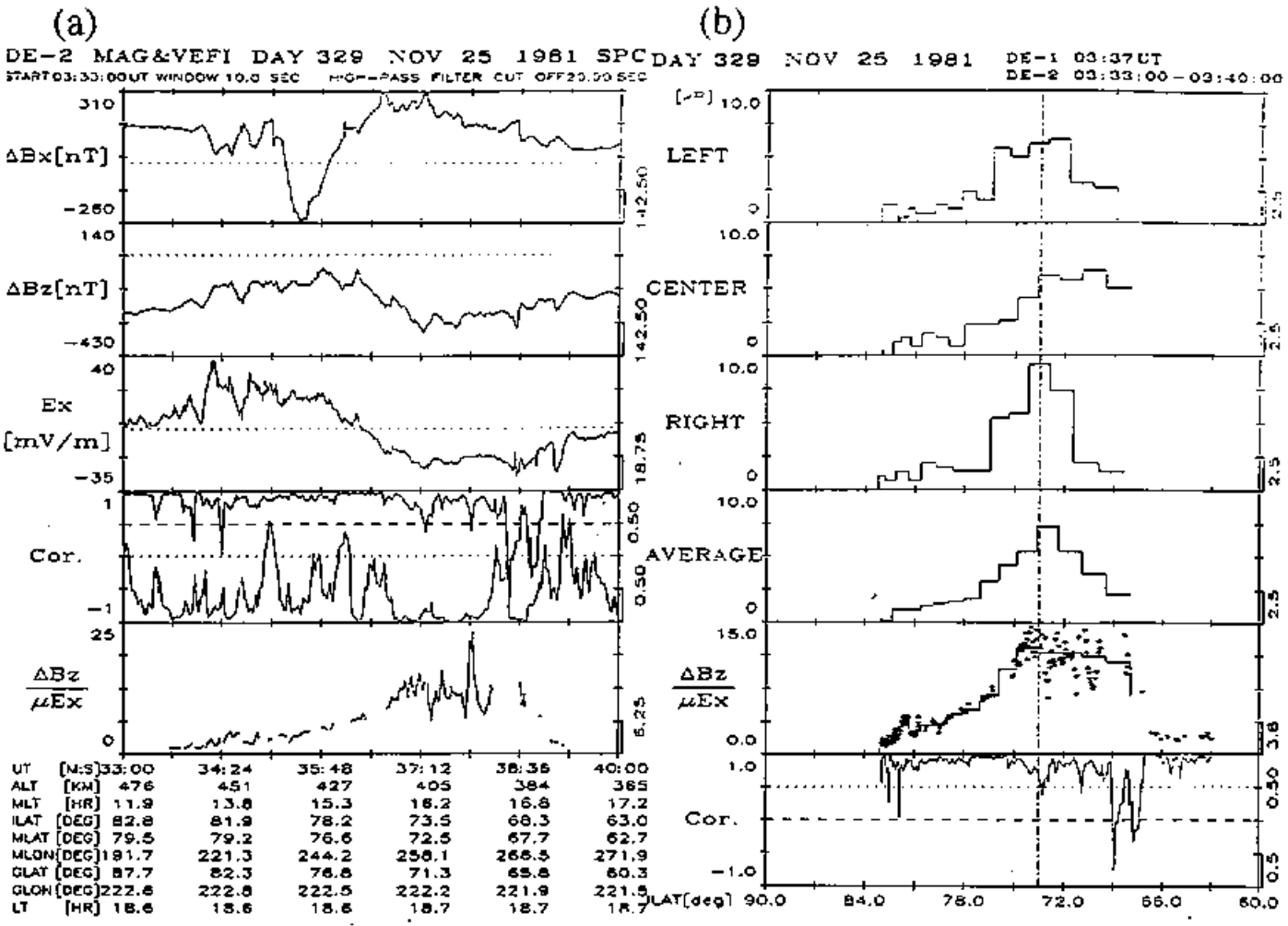
(a)
DE-2 MAG&VEFI DAY 329 NOV 25 1981 SPC
ΔBx[nT]
ΔBz[nT]
Ex [mV/m]
Cor.
ΔBz/μEx
(b)
DAY 329 NOV 25 1981
DE-1 03:37UT
DE-2 03:33:00-03:40:00
LEFT
CENTER
RIGHT
AVERAGE
ΔBz/μEx
Cor.
GLAT[deg]

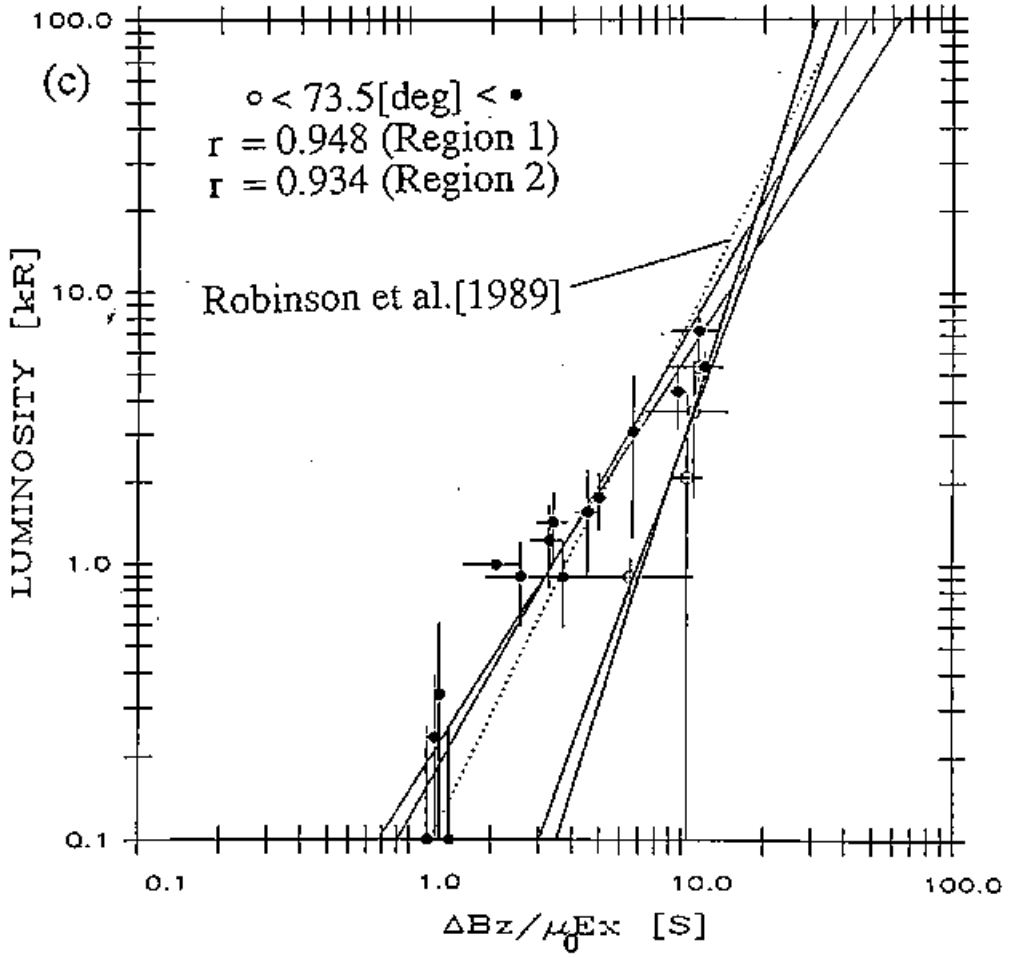
(c)
o < 73.5[deg] < •
r = 0.948 (Region 1)
r = 0.934 (Region 2)
Robinson et al.[1989]
LUMINOSITY [kR]
ΔBz/μ0Ex [S]

Figure 19

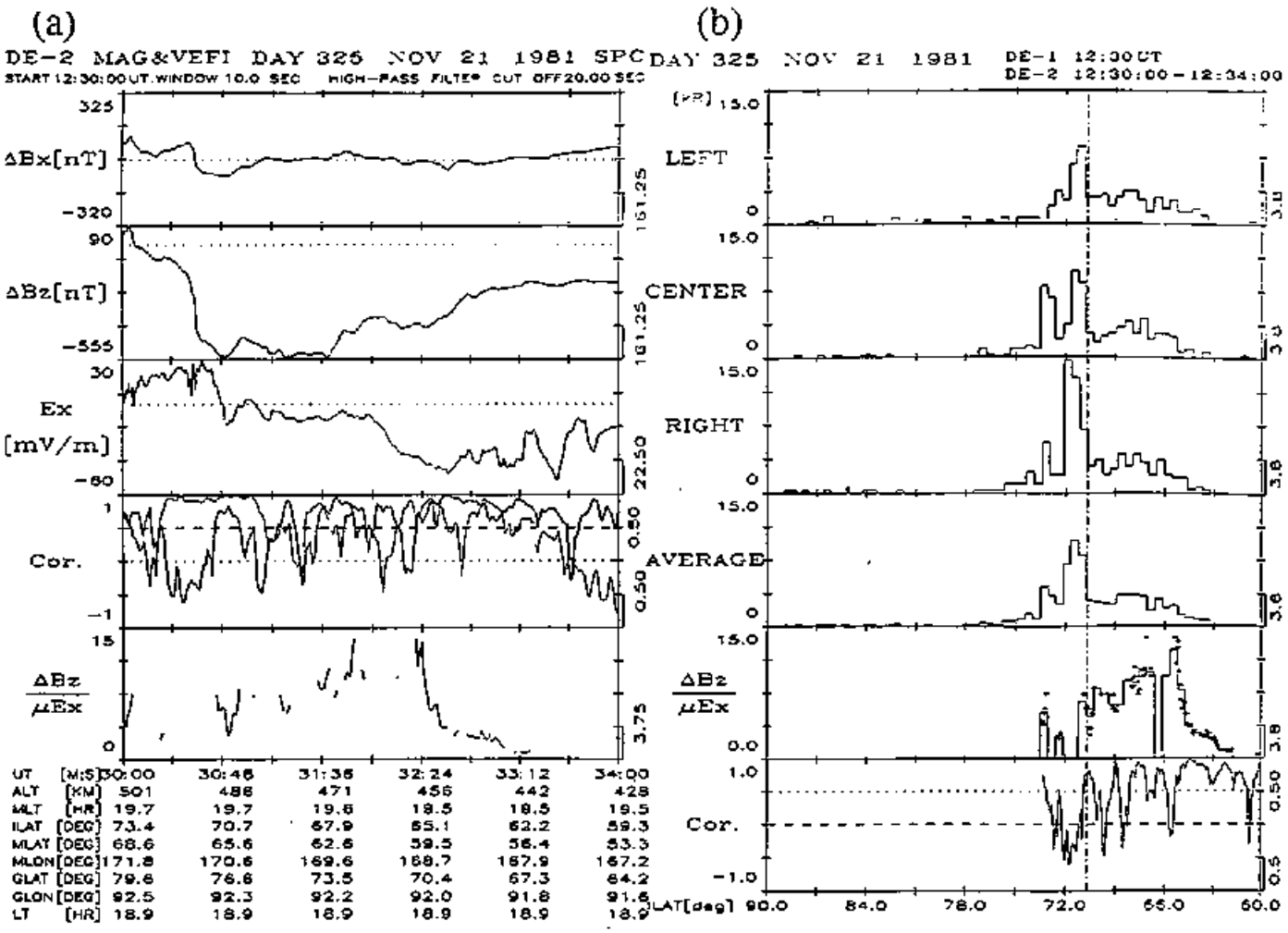
(a)
DE-2 MAG&VEFI DAY 325 NOV 21 1981 SPC
START 12:30:00 UT WINDOW 10.0 SEC HIGH-PASS FILTER CUT OFF 20.00 SEC
ΔBx[nT]
ΔBz[nT]
Ex [mV/m]
Cor.
ΔBz/μEx
UT [M:S] 30:00 30:48 31:36 32:24 33:12 34:00
ALT [KM] 501 486 471 456 442 428
MLT [HR] 19.7 19.7 19.6 19.5 19.5 19.5
ILAT [DEG] 73.4 70.7 67.9 65.1 62.2 59.3
MLAT [DEG] 68.6 65.6 62.6 59.5 56.4 53.3
MLON [DEG] 171.8 170.6 169.6 168.7 167.9 167.2
GLAT [DEG] 79.6 76.6 73.5 70.4 67.3 64.2
GLON [DEG] 92.5 92.3 92.2 92.0 91.8 91.6
LT [HR] 18.9 18.9 18.9 18.9 18.9 18.9
(b)
DAY 325 NOV 21 1981
DE-1 12:30 UT
DE-2 12:30:00 - 12:34:00
LEFT
CENTER
RIGHT
AVERAGE
ΔBz/μEx
Cor.
GLAT[deg] 90.0 84.0 78.0 72.0 66.0 60.0

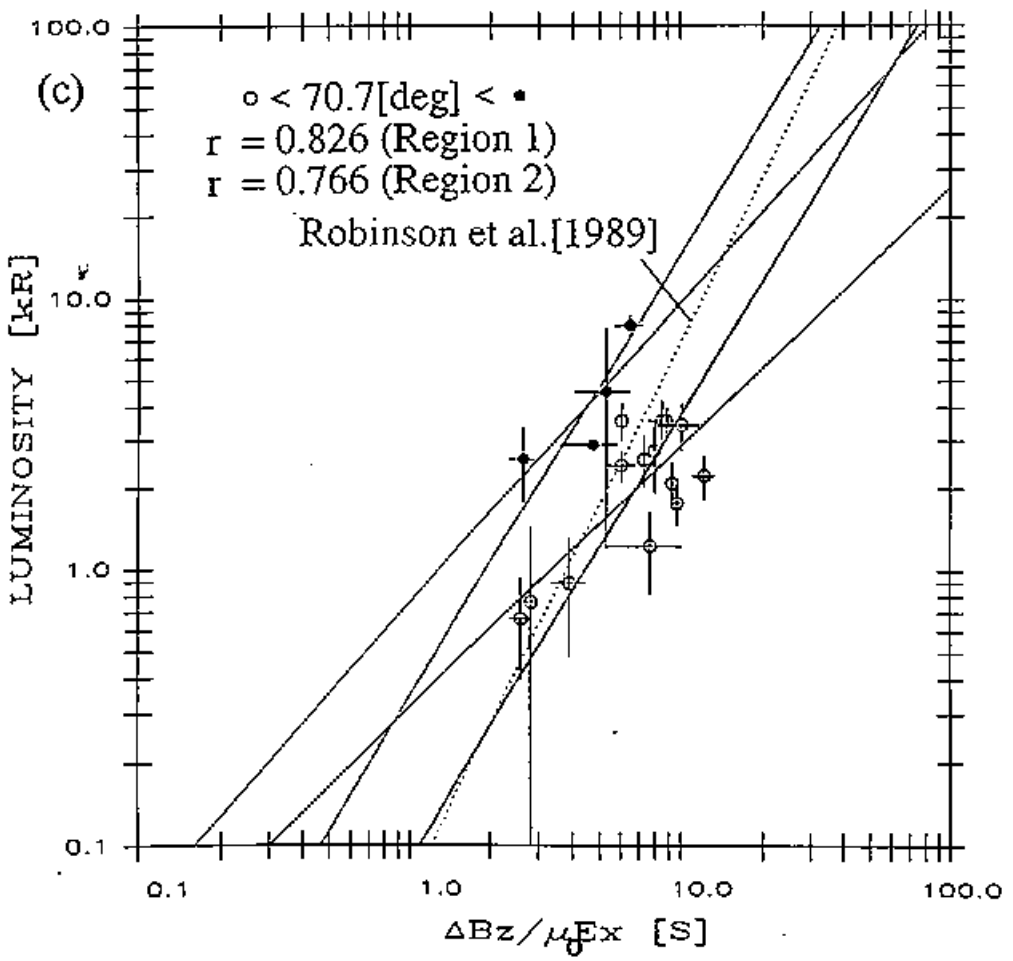
(c)
o < 70.7[deg] < •
r = 0.826 (Region 1)
r = 0.766 (Region 2)
Robinson et al.[1989]
LUMINOSITY [kR]
ΔBz/μEx [S]
0.1
1.0
10.0
100.0

Figure 20

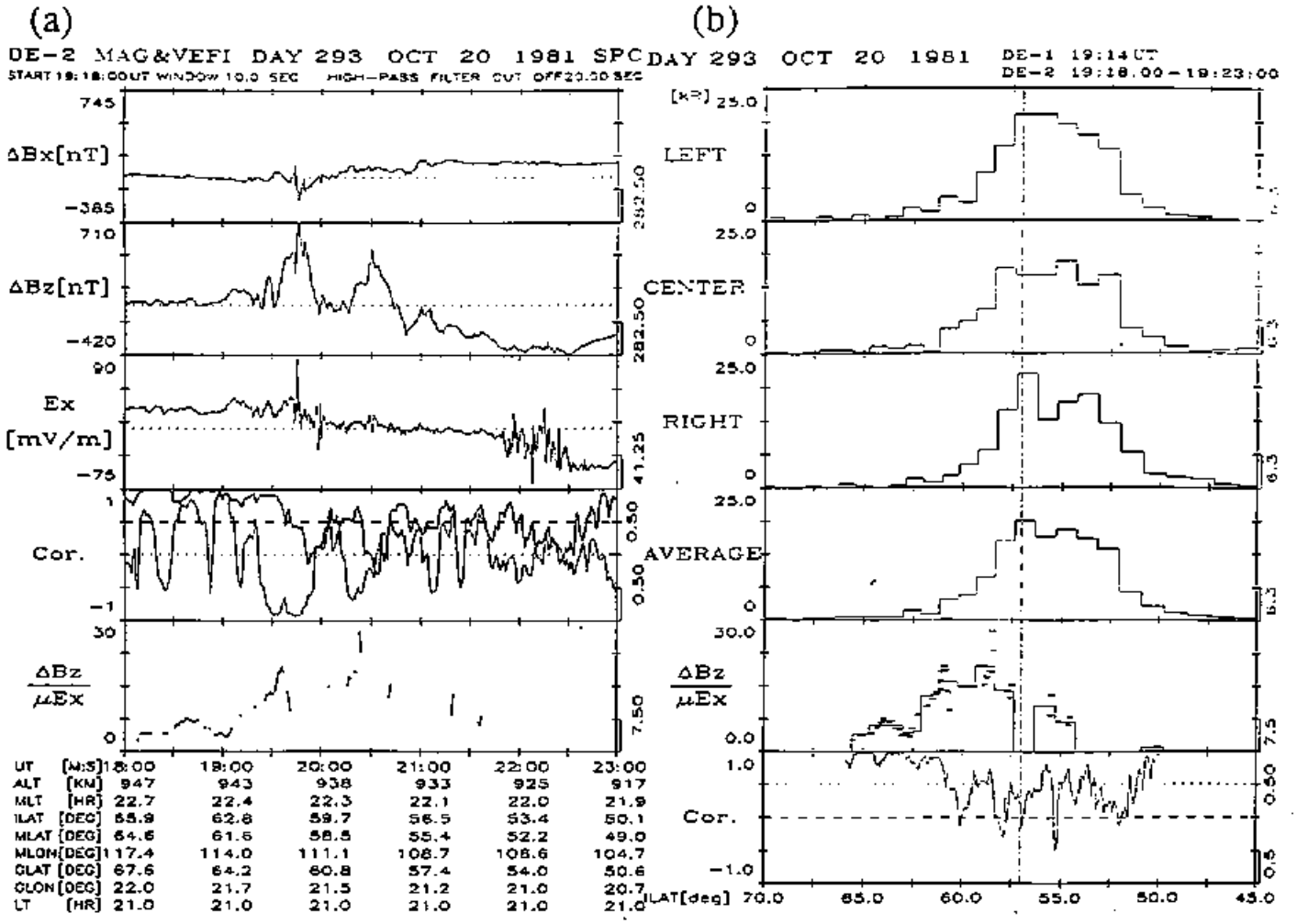
(a)
DE-2 MAG&VEFI DAY 293 OCT 20 1981 SPC
START 19:18:00UT WINDOW 10.0 SEC HIGH-PASS FILTER CUT OFF20.00 SEC
ΔBx[nT]
ΔBz[nT]
Ex [mV/m]
Cor.
ΔBz/μEx
UT (M:S) 18:00 19:00 20:00 21:00 22:00 23:00
ALT (KM) 947 943 938 933 925 917
MLT (HR) 22.7 22.4 22.3 22.1 22.0 21.9
MLAT (DEG) 64.6 61.6 58.5 55.4 52.2 49.0
MLON (DEG) 117.4 114.0 111.1 108.7 106.6 104.7
GLAT (DEG) 67.6 64.2 60.8 57.4 54.0 50.6
GLON (DEG) 22.0 21.7 21.5 21.2 21.0 20.7
LT (HR) 21.0 21.0 21.0 21.0 21.0 21.0
(b)
DAY 293 OCT 20 1981
DE-1 19:14UT
DE-2 19:18.00 - 19:23:00
LEFT
CENTER
RIGHT
AVERAGE
ΔBz/μEx
Cor.
GLAT[deg] 70.0 65.0 60.0 55.0 50.0 45.0

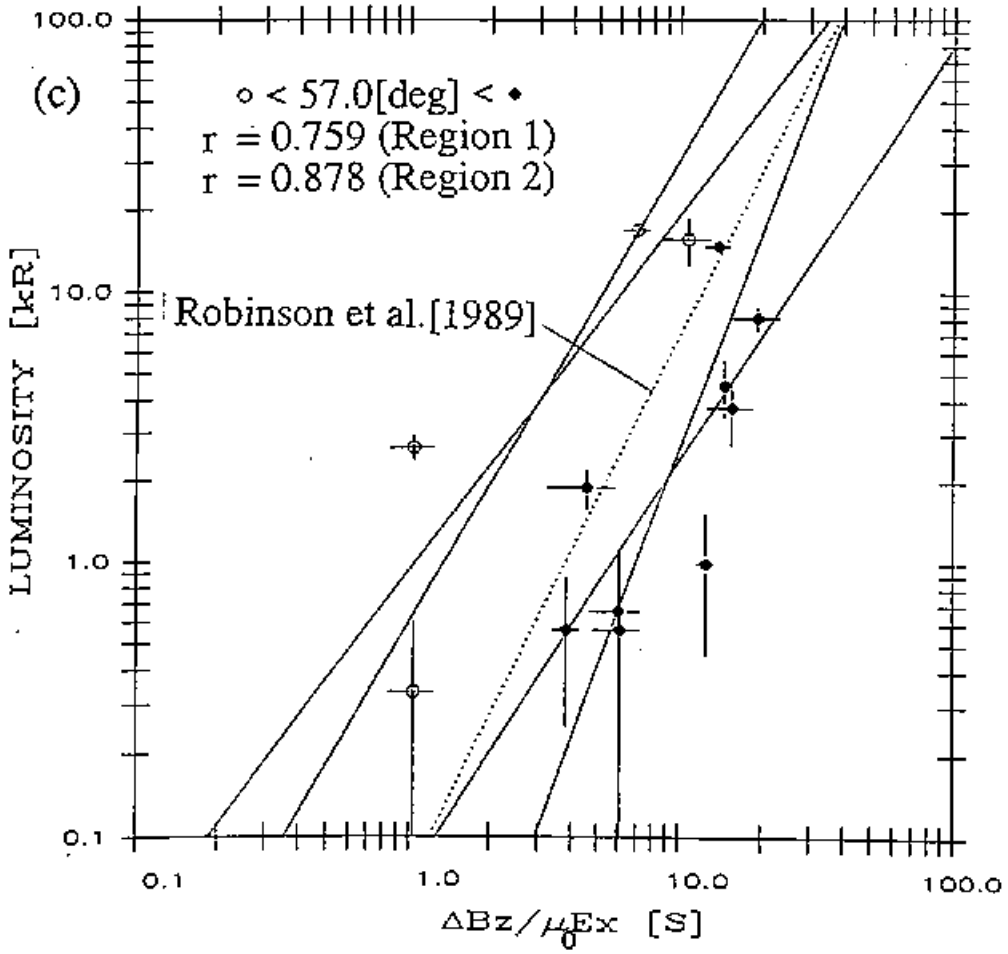
(c)
○ < 57.0[deg] < ●
r = 0.759 (Region 1)
r = 0.878 (Region 2)
Robinson et al.[1989]
LUMINOSITY [kR]
100.0
10.0
1.0
0.1
0.1
1.0
10.0
100.0
ΔBz/μ0Ex [S]

Figure 21

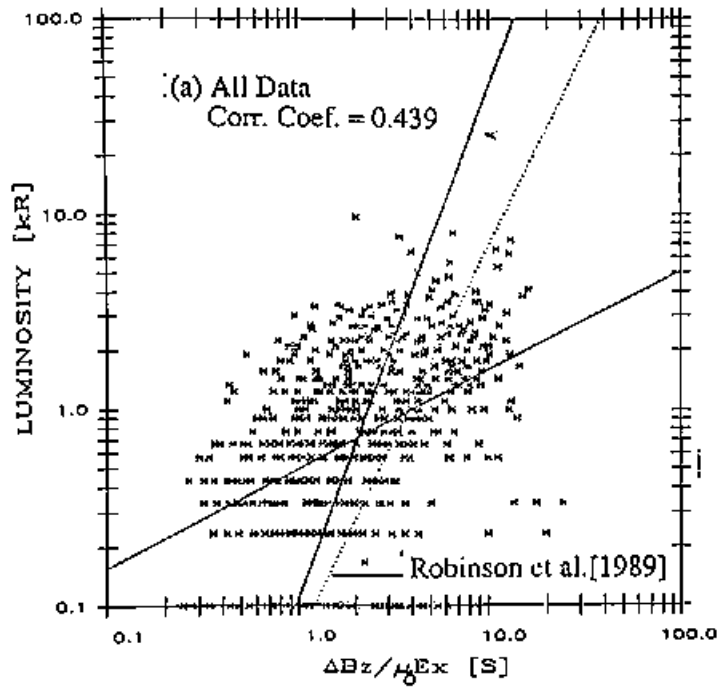
(a) All Data
Corr. Coef. = 0.439
Robinson et al.[1989]
LUMINOSITY [kR]
ΔBz/μ0Ex [S]
100.0
10.0
1.0
0.1
0.1
1.0
10.0
100.0

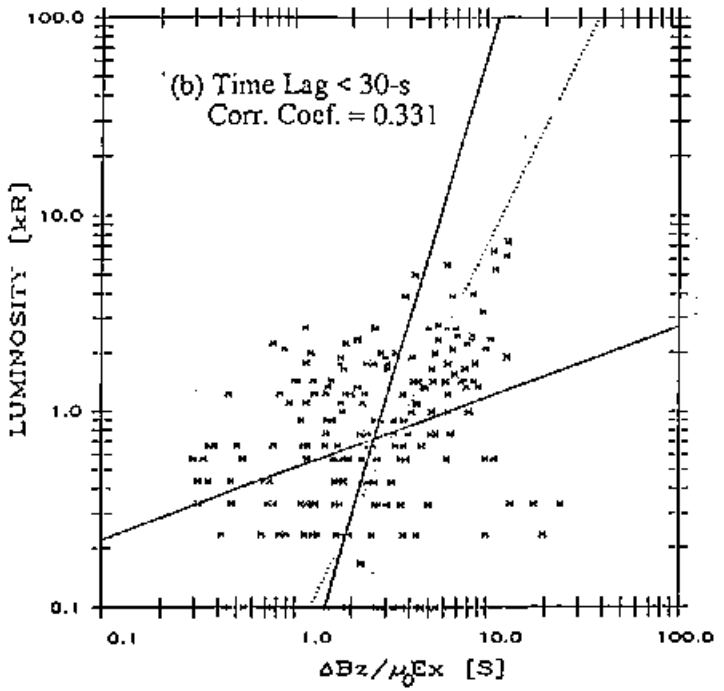
(b) Time Lag < 30-s
Corr. Coef. = 0.331
LUMINOSITY [kR]
ΔBz/μ0Ex [S]
100.0
10.0
1.0
0.1
0.1
1.0
10.0
100.0

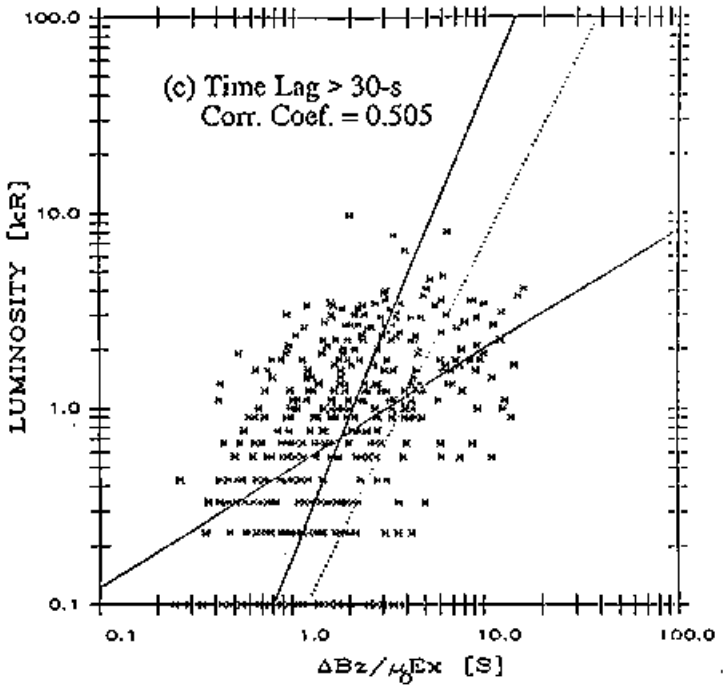
(c) Time Lag > 30-s
Corr. Coef. = 0.505
LUMINOSITY [kR]
ΔBz/μ0Ex [S]
100.0
10.0
1.0
0.1
0.1
1.0
10.0
100.0

Figure 22

Figure 23

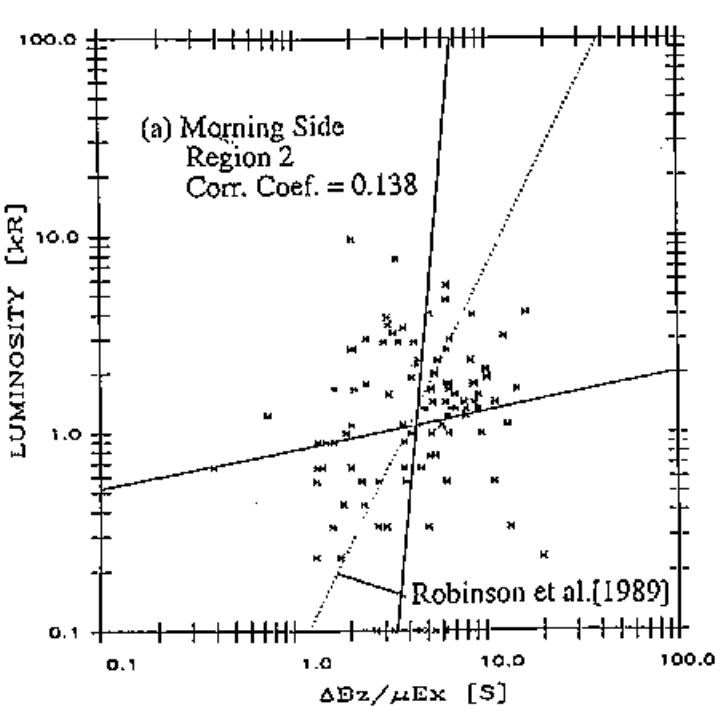
(a) Morning Side
Region 2
Corr. Coef. = 0.138
Robinson et al.[1989]
LUMINOSITY [kR]
ΔBz/μEx [S]
100.0
10.0
1.0
0.1

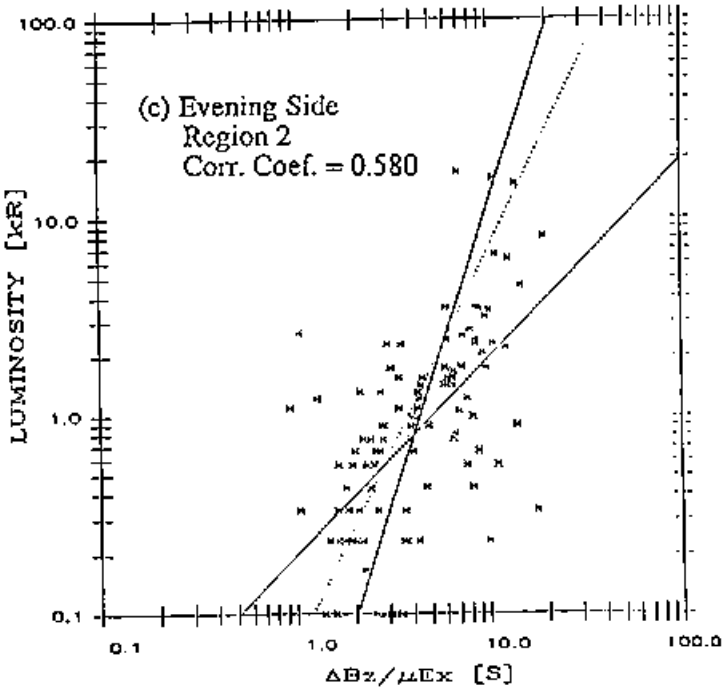
(c) Evening Side
Region 2
Corr. Coef. = 0.580
LUMINOSITY [kR]
ΔBz/μEx [S]
100.0
10.0
1.0
0.1

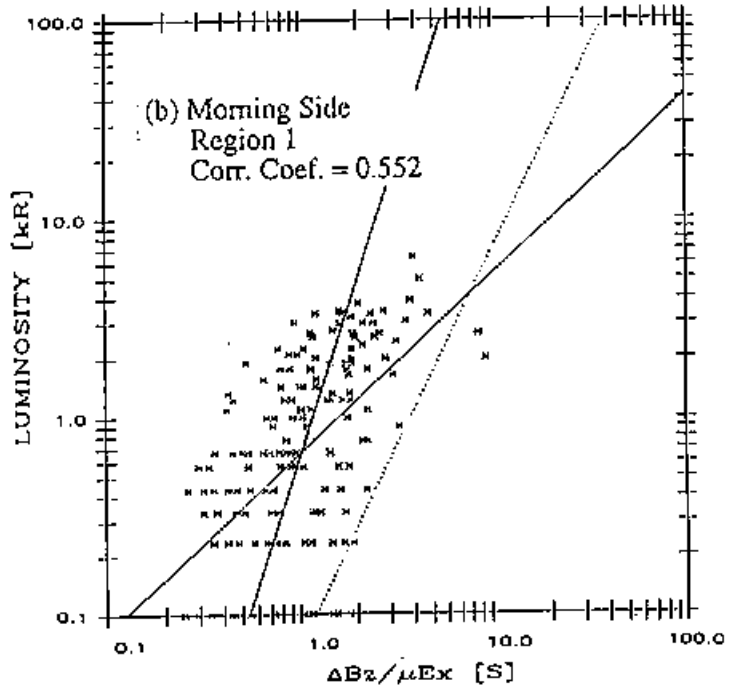
(b) Morning Side
Region 1
Corr. Coef. = 0.552
LUMINOSITY [kR]
ΔBz/μEx [S]
100.0
10.0
1.0
0.1

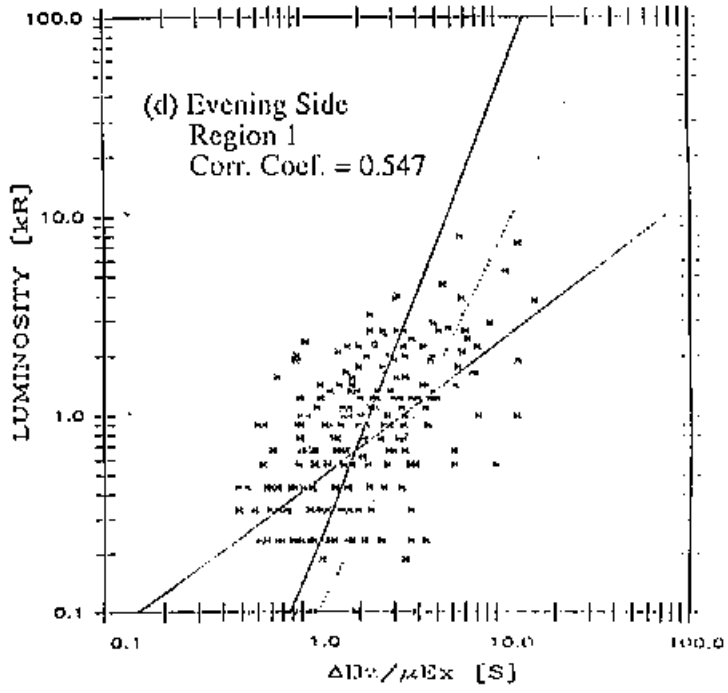
(d) Evening Side
Region 1
Corr. Coef. = 0.547
LUMINOSITY [kR]
ΔBz/μEx [S]
100.0
10.0
1.0
0.1

Figure 24

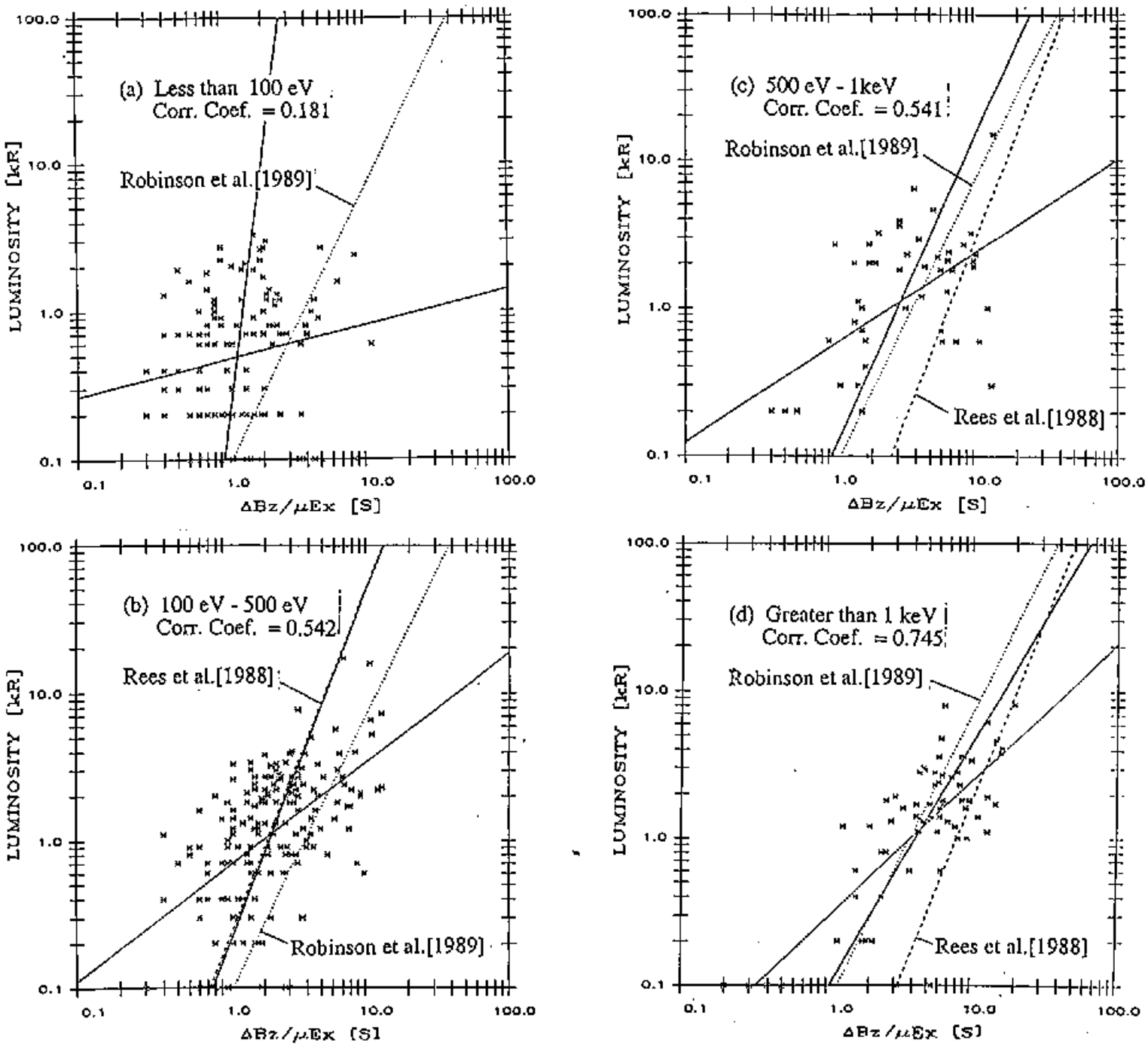
(a) Less than 100 eV
Corr. Coef. = 0.181
Robinson et al.[1989]
(b) 100 eV - 500 eV
Corr. Coef. = 0.542
Rees et al.[1988]
Robinson et al.[1989]
(c) 500 eV - 1keV
Corr. Coef. = 0.541
Robinson et al.[1989]
Rees et al.[1988]
(d) Greater than 1 keV
Corr. Coef. = 0.745
Robinson et al.[1989]
Rees et al.[1988]
LUMINOSITY [kR]
ΔBz/μEx [S]
100.0
10.0
1.0
0.1

Plate 1

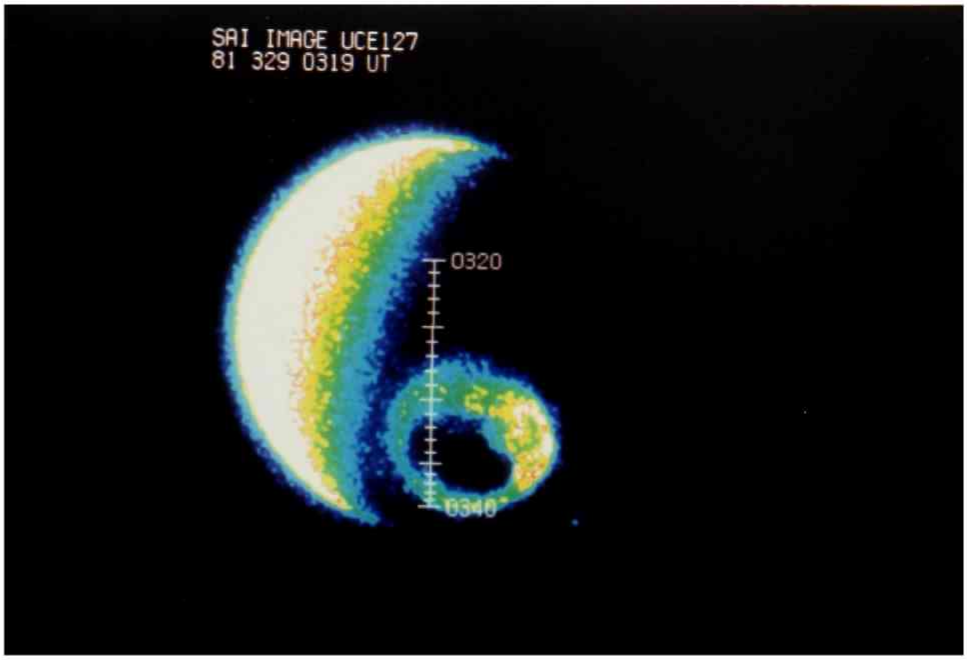

Plate 2

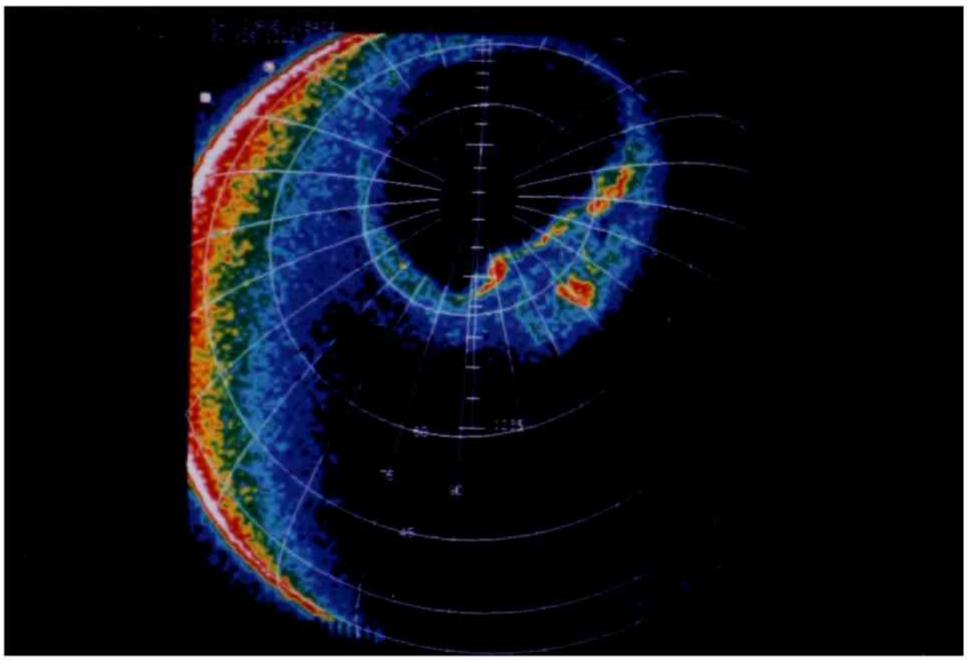

Plate 3

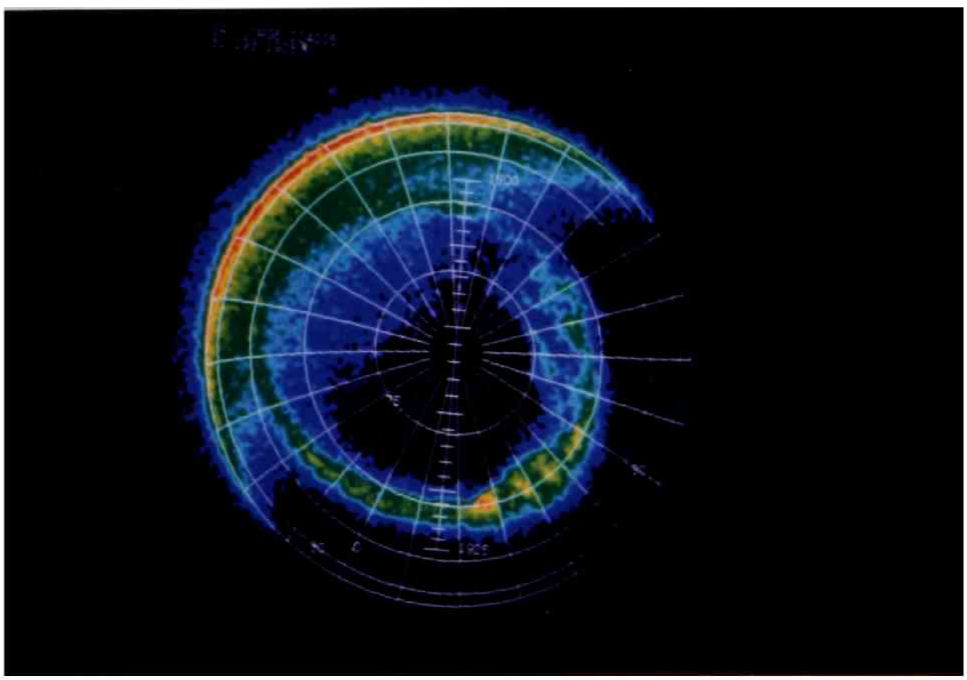

DYNAMICS EXPLORER
JOINT DATA PRESENTATION

Plate 4

YR/DAY: 81/329

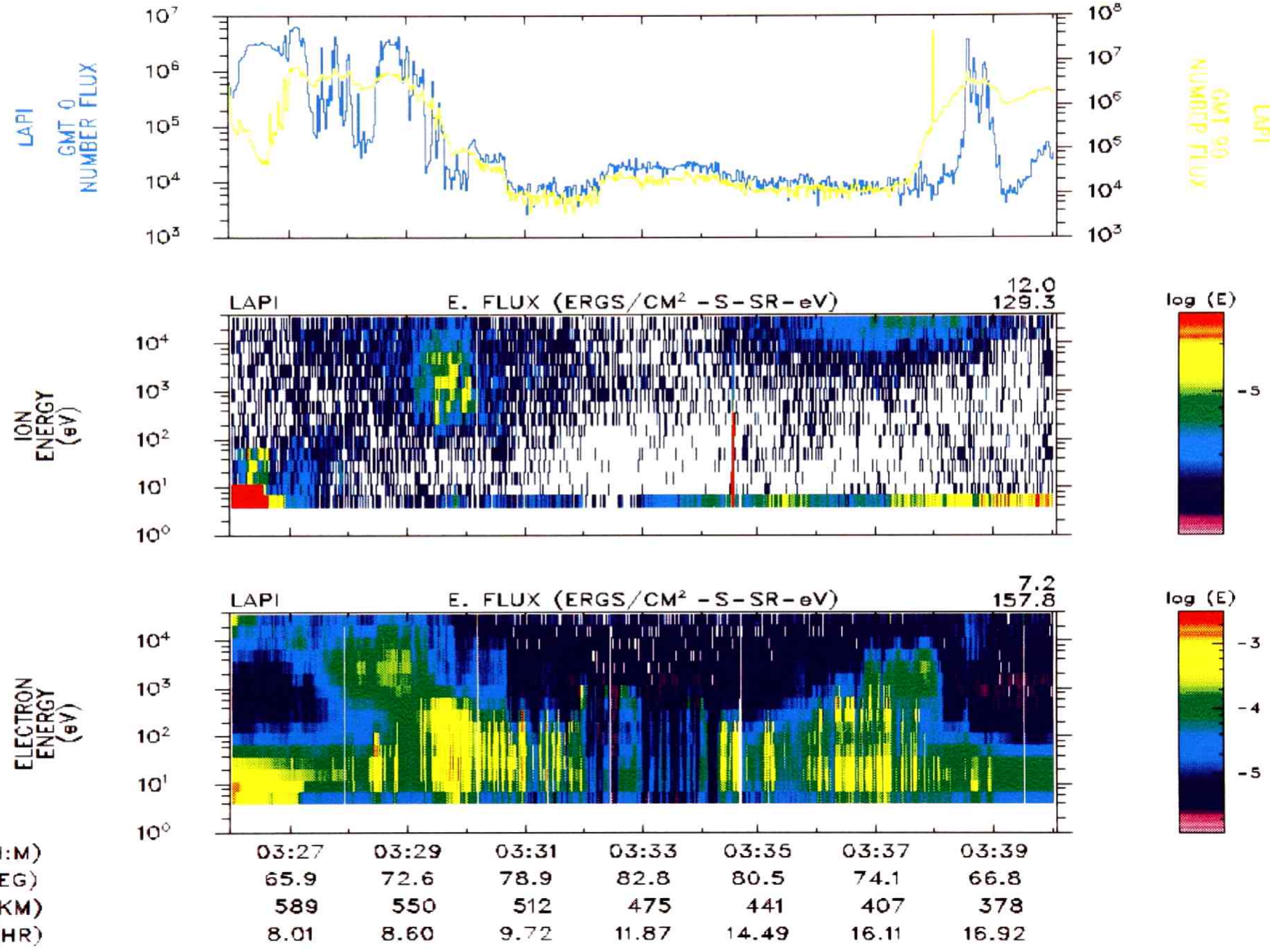

UT(H:M)	03:27	03:29	03:31	03:33	03:35	03:37	03:39
IL(DEG)	65.9	72.6	78.9	82.8	80.5	74.1	66.8
ALT(KM)	589	550	512	475	441	407	378
MLT(HR)	8.01	8.60	9.72	11.87	14.49	16.11	16.92

DYNAMICS EXPLORER
JOINT DATA PRESENTATION

Plate 5

YR/DAY: 81/325

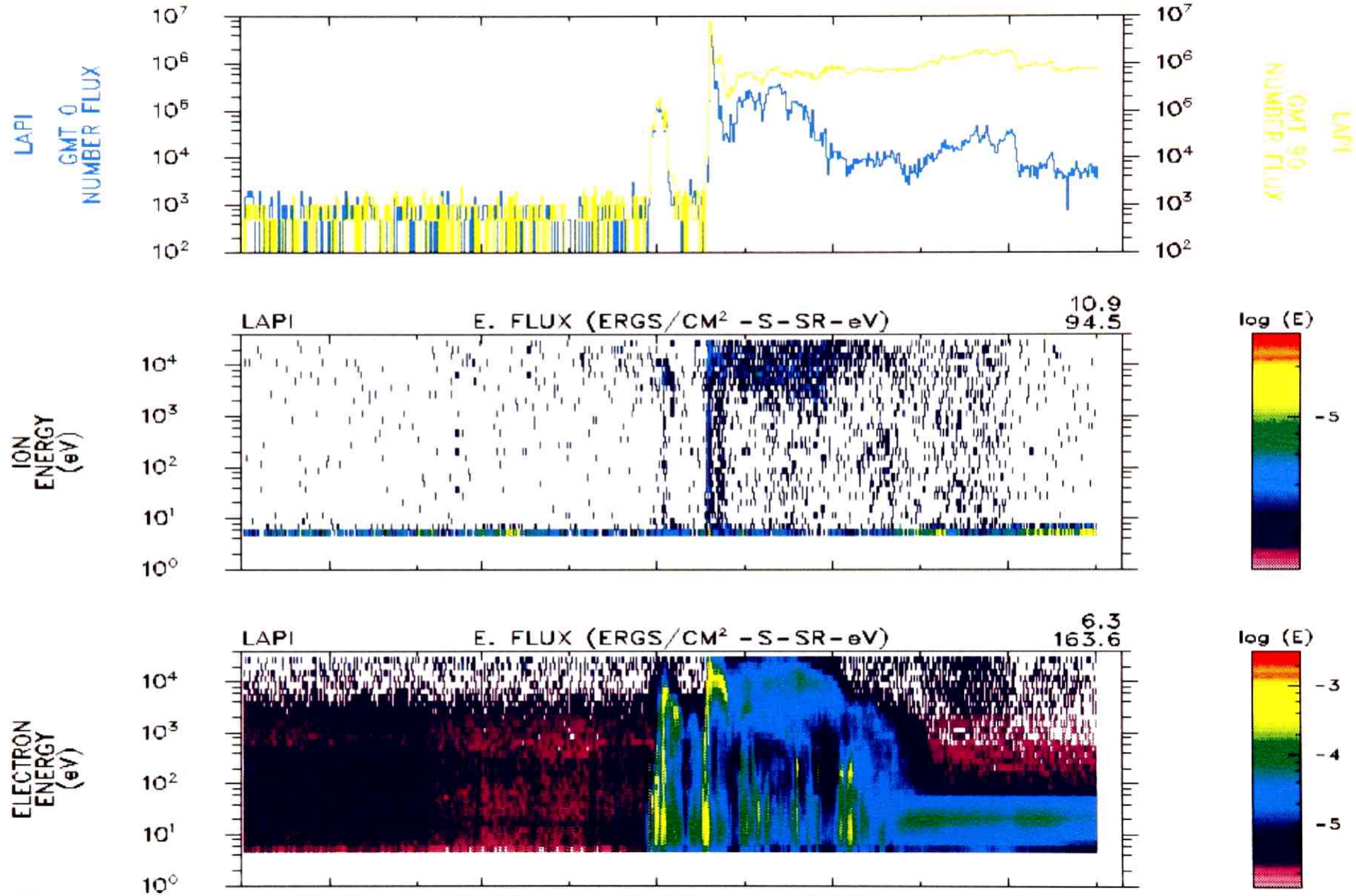

DYNAMICS EXPLORER
JOINT DATA PRESENTATION

Plate 6

YR/DAY: 81/293

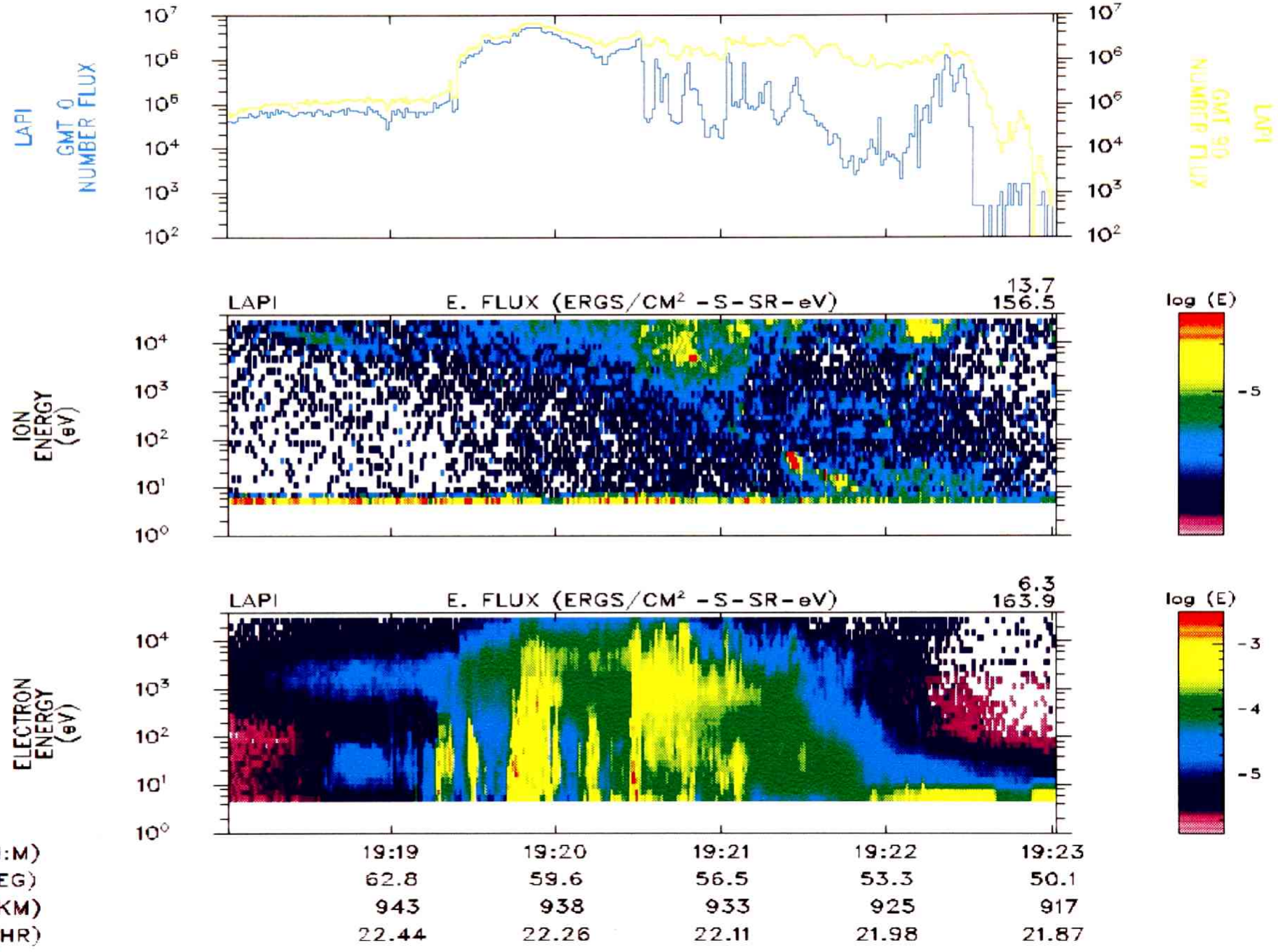

UT(H:M)	19:19	19:20	19:21	19:22	19:23
IL(DEG)	62.8	59.6	56.5	53.3	50.1
ALT(KM)	943	938	933	925	917
MLT(HR)	22.44	22.26	22.11	21.98	21.87